DEVELOP NEW NMR-BASED METHODS FOR CHARACTERIZATION OF PORE STRUCTURE AND QUANTIFICATION OF CATION EXCHANGE CAPACITY OF COMPLEX FORMATIONS

A Dissertation

by

KAI CHENG

Submitted to the Office of Graduate and Professional Studies of
Texas A&M University
in partial fulfillment of the requirements for the degree of

DOCTOR OF PHILOSOPHY

Chair of Committee,	Zoya Heidari
Co-Chair of Committee,	John Killough
Committee Members,	Walter B. Ayers
	Steven M. Wright
Head of Department,	Jeff Spath

May 2019

Major Subject: Petroleum Engineering

ABSTRACT

Nuclear magnetic resonance (NMR) measurements have been applied successfully for characterizing porosity, pore-size distribution, and permeability of conventional formations. Interpreting NMR measurements in reservoirs with complex pore geometry can, however, be challenging. I introduced contrast agents for improved NMR measurements to enable the characterization of interconnected/isolated pores and reliable assessment of permeability in formations with complex pore structures. Moreover, the reliability of laboratory NMR measurements in clay-rich formations is influenced significantly by environmental effects such as relative humidity. I systematically investigated the mechanisms of clay hydration at different relative humidity levels and quantified the impacts of relative humidity on NMR-based core analysis, and I investigated the mechanisms of clay hydration at different humidity levels. Furthermore, assessment of cation exchange capacity (CEC) is important for interpreting electrical resistivity logs, but reliable quantification of CEC is usually challenging. I established an analytical correlation between CEC and volume of hydration water, which was quantified by NMR measurements, and I developed a new NMR-based method to quantify the CEC of pure clay minerals and rocks.

In this dissertation, I prepared superparamagnetic Fe_3O_4 nanoparticles and Mn^{2+} solution as contrast agents and injected them into different formation types to characterize the isolated pores and interconnected pores using NMR measurements. Then, I eliminated the influence of isolated porosity and improved the assessment of

permeability for complex carbonate formations. The relative errors of permeability (compared to directly-measured CEC) decreased from more than 80% to less than 10%. In addition, I combined NMR and thermogravimetric analysis (TGA) measurements to quantify the impact of relative humidity on core measurements. The variation in relative humidity caused more than 250% uncertainty in porosity assessment. The volume of hydration water was quantified at different relative humidity levels using NMR measurements. Based on the energy balance between electric potential energy and chemical potential energy, I established an analytical correlation between the volume of hydration water and the CEC of clay minerals and developed a new method for quantifying CEC. Then, I successfully quantified the CEC of four types of pure clay minerals with less than 7 meq/100 g error. Finally, I extended the new method for CEC quantification to rocks with multiple types of clay minerals. The relative error of CEC estimates (compared to the CEC from the wet chemistry method) for shaly sand formations was less than 4 meq/100 g. CEC estimates for organic-rich mudrock formations agreed with CEC estimates from the membrane potential method.

The contributions of this dissertation include (a) introducing contrast agents for improved NMR-based assessment of interconnected and isolated pores/fractures in complex formations, (b) improving NMR-based permeability assessment, (c) quantifying the impact of relative humidity on the reliability of NMR-based core measurements, and (d) establishing a new method for CEC assessment in pure clay minerals and in rocks with complex mineralogy by integrating NMR, X-ray diffraction (XRD), pyrolysis, and nitrogen adsorption-desorption measurements.

DEDICATION

To my beloved parents, Feicun and Lingyu, for their constant love and care.

To my lovely and supportive wife, Huafang, who always encourages and motivates me.

To my little son, Jasper, who brings me joy and makes me more fulfilled than I could have ever imagined.

ACKNOWLEDGEMENTS

I would like to express my deepest gratitude to my advisor, Dr. Zoya Heidari, for her support during my Ph.D program. None of these achievements would have been possible without her guidance. Her profound knowledge, insightful advice, and enthusiasm for science guided and motivated me through these years. I would like to express my gratitude to my co-chair, Dr. John Killough, for his assistance and guidance during my Ph.D study. Also, I would like to extend my appreciation to Dr. Walter Ayers and Dr. Steven Wright for serving as my committee members and for their useful and insightful technical comments.

I would thank my teammate Aderonke Aderibigbe for her help and collaboration during the first year of my Ph.D. study. I would thank my teammate Lu Chi for collaborating on one of my papers. I would like to thank all my friends at Texas A&M University and my teammates in the Multi-Scale Formation Evaluation research group for their continuous support and encouragement. Special thanks go to Huangye Chen, Angie Yang, Gama Firdaus, and Artur Posenato Garcia. I would also like to thank my teammates at the University of Texas Austin, Artur Posenato Garcia, Archana Jagadisan, Andres Gonzalez, and Saurabh Tandon, for their help during my study there.

My Co-op at Halliburton was a valuable educational experience that helped enhance my knowledge and research in NMR techniques. I am very grateful to my mentor, Dr. Gabriela Leu, and to my supervisor, Dr. Songhua Chen, for giving me the

opportunity to learn and work with them—and of course my Ph.D advisor, Dr. Zoya Heidari, for recommending and approving me to go to the Co-op.

I would like to express my gratitude to the financial sponsors of the research conducted in this dissertation. The work was funded by the Texas A&M University Joint Industry Research Program on Multi-Scale Formation Evaluation and was sponsored jointly by Aramco Services Company, BHP Billiton, BP, Chevron, ConocoPhillips, and Devon Energy, as well as the Crisman Institute for Petroleum Research at the Harold Vance Department of Petroleum Engineering.

CONTRIBUTORS AND FUNDING SOURCES

Contributors

This work was supported by a dissertation committee consisting of Professor Dr. Zoya Heidari [advisor], Dr. John Killough [co-advisor], and Dr. Walter B. Ayers of the Department of Petroleum Engineering, and Dr. Steven M. Wright of the Department of Electrical and Computer Engineering.

All work conducted for the dissertation was completed by the student independently.

Funding Sources

Graduate study was supported by the Texas A&M University Joint Industry Research Program on Multi-Scale Formation Evaluation and was sponsored jointly by Aramco Services Company, BHP Billiton, BP, Chevron, ConocoPhillips, and Devon Energy, as well as the Crisman Institute for Petroleum Research at the Harold Vance Department of Petroleum Engineering.

NOMENCLATURE

a	Constant coefficient in the SDR model
B_e	Equivalent conductance of clay cation
BVI	Bound fluid volume
C	Empirical constant in the Coates model
CEC	Cation exchange capacity (meq/100g)
CEC_{apparent}	The sum of CEC for exchangeable cations from ICP-MS measurements
$CEC_{\text{corrected}}$	CEC corrected for the influence of salt precipitants
CEC_{Ca2+}	CEC of Ca^{2+} in clay minerals (meq/100g)
CEC_{Ca2+}	CEC of Ca^{2+} in clay minerals (meq/100g)
CEC_{Ca2+}	CEC of Ca^{2+} (meq/100g)
CEC_i	CEC of each mineral i
CEC_i	CEC of pure clay mineral i (meq/100g)
CEC_{K+}	CEC of K^+ (meq/100g)
CEC_{Mg2+}	CEC of Mg^{2+} (meq/100g)
CEC_{Na+}	CEC of Na^+ (meq/100g)
Con	Concentration of paramagnetic component (ppm)
$Corr$	The correction factor for influence of salt precipitant (meq/100g)
d	Basal spacing before swelling (Å)
d'	Distance between two successive layers before swelling

$d_{1/2}$	Distance from cations to the surface of clay minerals before hydration (Å)
D	Basal spacing after swelling (Å)
D'	Distance between two successive layers after swelling
$D_{1/2}$	Distance from cations to the surface of clay minerals after hydration (Å)
$Diff$	Diffusion coefficient (m^2/sec), in chapter II
D_S	Thickness of hydration water on the surface of clay minerals (Å)
e	Elementary charge (1.6022×10^{-19} C)
E	Electric field strength ($V \cdot m^{-1}$)
emf	The liquid-liquid junction potential (mV)
FFI	Free fluid volume, fraction
G	Spatial gradient of internal magnetic field (Hz/mm)
ΔG	Gibbs free energy change of the hydration reaction ($J \cdot mol^{-1}$)
ΔG^0	Standard-state Gibbs free energy of the hydration reaction ($J \cdot mol^{-1}$)
i	Type of cation (i.e., Na^+, Mg^{2+}, K^+, or Ca^{2+})
j	Different type of mineral in rock sample
k	Number of rock samples with different mineral composition
k_{coates}	Permeability estimated using the Coates model
k_{SDR}	Permeability estimated using the SDR model
$k_{SDR,Chang}$	Permeability estimated using the SDR model modified by Chang
K	Dimensionless shape factor
K_p	Equilibrium constant of hydration reaction

m_1 *and* m_2	Molar concentration of brine at two side of membrane (mol)
m_{Ca2+}	Atomic mass of Ca^{2+}(40.1 g·mol^{-1})
m_{K+}	Atomic mass of K^+ (39.1 g·mol^{-1})
m_{Mg2+}	Atomic mass of Mg^{2+} (24.3 g·mol^{-1})
m_{Na+}	Atomic mass of Na^+ (23.0 g·mol^{-1})
m_{NaCl}	Molecular mass of NaCl (58.4 g·mol-1)
m_w	Water molar mass (18.0 g·mol^{-1})
M	Total number of minerals in rock samples
M_j	Mass concentration of mineral *j*
M_{km}	Mass concentration of mineral *m* in rock sample *k*
M_{kn}	Mass concentration of clay mineral *n* in rock sample *k*
M_{rock}	Mass of rock sample (g)
$Mass_{clay}$	Total mass of clay minerals (g)
n	Total number of minerals in the samples
N	Average number of interlayers
N_A	Avogadro constant (6.0221 × 10^{23} mol^{-1})
$N_{c,i}$	Quantity of cation *i*
p	Pore connectivity coefficient
$P_{clay(s)}$	Partial pressure of dry clay minerals (atm, 1.01×10^5 Pa)
$P_{H2O(g)}$	Partial pressure of water vapor (atm)
$P^*_{H2O(g)}$	Equilibrium vapor pressure of water at a given temperature (atm)

$P_{\text{clay·H2O(s)}}$	Partial pressure of hydrated clay minerals (atm)
Q_v	The CEC per unit pore volume of the rock (meq/cc)
r	Relaxivity constant ($ppm^{-1}\cdot sec^{-1}$)
R	Gas constant ($8.3145\ J\cdot K^{-1}\cdot mol^{-1}$)
$Rate$	Relaxation rate of fluid with paramagnetic component (sec^{-1})
$Rate^0$	Relaxation rate without contrast agent (sec^{-1})
RH	Relative humidity
RT/F	Thermodynamic constants (equal to 25.69 mV at 25 ˚C)
S	Effective surface area of clay minerals ($m^2\cdot g^{-1}$)
S_{BET}	Brunauer–Emmett–Teller (BET) surface area ($m^2\cdot g^{-1}$)
S_j	Surface area of mineral j
S_n	Surface area of mineral n
S_{total}	Surface area of rock sample
$S_{total,\,k}$	Surface area of rock sample k
S_w	Water Saturation
t_{Na}^{hf}	Hittorf transport number of the sodium ion
T	Absolute temperature (K)
T_2	NMR spin-spin relaxation time (msec)
T_{2B}	Bulk relaxation time (msec)
$T_{2cutoff}$	T_2 that divides the T_2 distribution into free fluid and bound fluid (msec)
T_{2gm}	Geometric mean of T_2 distribution (msec)

$T_{2gm,inter}$	Geometric mean of T_2 distribution of interconnected pore space (msec)
$T_{2gm,iso}$	Geometric mean of T_2 distribution of isolated pore space (msec)
$T_{2gm,total}$	Geometric mean of T_2 distribution of total pore space (msec)
$T_{2gm,<750ms}$	Geometric mean of T_2 distribution less than 750 msec (msec)
T_{2i}	T_2 relaxation time at time interval I (msec)
$T_{2i,critial}$	Critical T_2 time to distinguish isolated pores and connected pores (msec)
T_{2S}	Surface relaxation time (msec)
TE	Inter-echo spacing time (μsec)
Tp	Temperature (˚C)
Δu_i	Electric potential change of each cation ($J \cdot g^{-1}$)
ΔU	Total change in electric potential energy of cations ($J \cdot mol^{-1}$)
$\Delta U_{interlayer}$	The change in electric potential energy due to hydration at interlayer space of clay minerals ($J \cdot mol^{-1}$)
$\Delta U_{surface}$	The change in electric potential energy due to hydration on the surface of clay minerals ($J \cdot mol^{-1}$)
V	Volume of leachate (mL)
V_{HW}	Volume of total hydration water per 100g mass of dry clay minerals (mL/100g)
$V_{HW,j}$	Volume of hydration water for each mineral i (mL/100g)
$V_{HW,total,k}$	Total volume of hydration for rock sample k (mL/100g)
$V_{interlayer}$	Volume of interlayer hydration water per 100g mass of dry clay minerals (mL/100g)

z	Valence of cation
z_i	Valence of cation *i*
β	Line broadening at half the maximum intensity of reflection
γ	Gyromagnetic ratio, rad/(sec·Tesla)
$\gamma_{\pm}$	Mean ionic activity coefficient of an electrolyte
ε_0	Vacuum permittivity (8.854×10^{-12} C·V^{-1}·m^{-1})
ε_{is}	Relative permittivity of interlayer space
ε_w	Relative permittivity of water (80.4)
η	The order of reflection in Bragg's law
θ	Bragg diffraction angle
λ	Wavelength of XRD source (1.5418 Å)
$\Delta\mu$	The change in chemical potential of hydration reaction (J·mol^{-1})
ρ	Surface relaxivity (μm/sec)
ρ_{brine}	Density of each mineral *i* (mL·g-1)
ρ_{i}	Density of brine (1.1 mL·g-1)
ρ_{rock}	Density of rock (2.6 mL·g-1)
ρ_{w}	Density of water (1.0 mL·g-1)
σ	Surface charge density of clay minerals (C·m^{-2})
τ	Particle size of clay minerals in the lamellar direction (Å)
ϕ	Porosity of the rock
ϕ	Porosity of the rock

ϕ_i	Incremental porosity at each T_2 relaxation time T_{2i}
$\phi_{i,AI}$	Incremental porosity at each T_{2i} after injection
$\phi_{i,iso}$	Incremental porosity of isolated pores at each T_2 relaxation time T_{2i}
ϕ_{inter}	Interconnected porosity of rock samples
ϕ_{iso}	Isolated porosity of rock samples
ϕ_{total}	Total porosity of rock samples
$\phi_{<750ms}$	Cumulative porosity when T_2 relaxation time less than 750 msec

ACRONYMS

CPMG	Carr-Purcell-Meiboom-Gill
LIL	Log-Inject-Log
MICP	Mercury Injection Capillary Pressure
Mn^{2+}	Manganese ion
MRI	Magnetic Resonance Imaging
NMR	Nuclear Magnetic Resonance
NSA	Number of Scans
SDR	Schlumberger Doll Research
SNR	Signal-to-Noise Ratio
SPION	Superparamagnetic Iron Oxide Nanoparticles
TEM	Transmission Electron Microscope

TABLE OF CONTENTS

Page

LIST OF FIGURES

Page

LIST OF TABLES

Page

CHAPTER I

INTRODUCTION

Petrophysical interpretation of reservoirs with complex pore geometry is challenging using conventional methods for interpretation of nuclear magnetic resonance (NMR) measurements. The main challenges discussed in this dissertation include characterization of interconnected porosity and isolated porosity, pore-size distribution, and permeability. This dissertation introduces NMR contrast agents for characterizing interconnected pores and isolated pores in complex formations. The introduced technique also improves NMR-based permeability assessment for rocks with isolated pores. In addition, interpretation of laboratory NMR measurements is challenging in some clay-rich formations. The water content in clay minerals is affected significantly by the relative humidity of laboratory conditions, causing variation in fluid-bearing porosity using NMR measurements. I experimentally quantified the impact of relative humidity on hydration of clay minerals by combining NMR and thermogravimetric analysis (TGA) measurements. I also discovered a strong correlation between the NMR-based estimates of volume of hydration water and the cation exchange capacity (CEC) of clay minerals. This strong correlation implies the possibility to develop a new method for evaluating CEC using NMR measurements. Dependable quantification of CEC is important for interpreting electrical resistivity logs in clay-rich formations. However, the conventional methods for CEC quantification, such as wet chemistry, multiple salinity, and membrane potential, can each have limitations. This work developed a new method

for reliably quantifying the CEC of pure clay minerals and rocks with multiple types of clay minerals by combining interpretation of NMR, XRD, pyrolysis, and nitrogen adsorption-desorption measurements.

1.1 Background

This dissertation includes four parts of research work. The first part documents use of nanoparticles as NMR contrast agents for enhanced interpretation of pore-network connectivity in formations with complex pore geometry. The second part extends the use of contrast agents to improve evaluation of NMR-based permeability in carbonate formations with complex geometry. The third part of this dissertation focuses on investigating the impact of relative humidity on the reliability of NMR-based core analysis, which has not been studied systematically in literature. The fourth part documents development of a new method to quantify the CEC of pure clay minerals and rocks with multiple types of clay minerals. The background and literature for each part of the research are reviewed individually in the following subsections.

1.1.1 Nanoparticles as NMR Contrast Agents for Pore-Network Connectivity Assessment

The application of nanoparticles as contrast agents for reservoir characterization and advanced reservoir surveillance is of particular interest to the petroleum industry. Historic applications involve the synthesis and use of nanoparticles such as iron oxide

for detecting waterflood fronts (Al-Shehri et al., 2013). Ongoing research studies are investigating the use of nanoparticles as contrast-enhancing agents to improve conventional data acquisition methods such as NMR, controlled source electromagnetic (CSEM) surveys, and other near-wellbore measurements such as magnetic susceptibility, acoustic, and resistivity measurements (Barron et al., 2010).

Magnetic nanoparticles have been applied successfully in medicine and biomedicine disciplines for targeted drug delivery and as contrast agents in magnetic resonance imaging (MRI) (Józefczak et al., 2005; Yang et al., 2009). The contrast agents relax the proton nuclear spins extremely fast during MRI scans; thus, they appear as dark spots in MRI images and assist in diagnostic decisions. Similar to the application of magnetic nanoparticles as contrast agents in MRI, magnetic nanoparticles also can be used as contrast agents for borehole NMR measurements. NMR T_2 (spin-spin relaxation) distributions represent the pore-size distribution of the rock (Coates et al. 1999). NMR T_2 relaxation time is shifted to a short relaxation time with the presence of magnetic nanoparticles under the Carr-Purcell-Meiboom-Gill (CPMG) pulse sequence (Carr and Purcell, 1954; Meiboom and Gill, 1958). The invasion of magnetic nanoparticles helps improve pore connectivity characterization using NMR T_2 distribution. The NMR log-inject-log (LIL) method has been introduced using brine doped with paramagnetic ions (e.g., Mn^{2+}) for quantifying residual oil saturation (e.g., Neuman 1983; Horkowitz et al. 1995; Crowe et al. 1997; Funk et al. 2004; Schulz et al. 2011; Toumelin et al. 2012), but not for improving pore connectivity assessment.

1.1.2 NMR Contrast Agents for Permeability Assessment

An important application of NMR logging is real-time and in-situ permeability assessment. In conventional formations, NMR borehole measurements estimate permeability the most accurately because of the correlation between NMR T_2 distribution and pore-size distribution (Seevers, 1966; Sen et al., 1990). Conventional NMR-based permeability models include the Coates model (Coates et al. 1997) and the Schlumberger Doll Research (SDR) model (Kenyon et al. 1986). Both the Coates and SDR models have been used successfully for permeability assessment in conventional formations. However, these models are not reliable in some carbonate formations where the pore network is not well connected. For instance, some carbonate formations contain isolated pores, such as large isolated vugs and intragranular pores. These isolated pores might be misinterpreted as connected pores, causing unreliable evaluation of permeability.

To avoid the aforementioned challenge, Chang et al. (1997) modified the SDR model by introducing an empirical vugs model in which a T_2 time above 750 msec is considered to be isolated vugs and therefore not used for permeability calculation. Chen et al. (2008) introduced a pore-connectivity coefficient to eliminate the influence of vugs or intragranular porosity. However, these attempts will have challenges for application in various types of formation due to use of approximate and empirical constants.

1.1.3 Impact of Relative Humidity on the Reliability of NMR-Based Core Analysis

Core analysis is important for petrophysical evaluation of organic-rich mudrocks due to uncertainties in well-log interpretation (Shafer, 2013). However, laboratory environmental conditions such as humidity can alter the status of core samples (Unalmiser et al., 1998) and potentially cause unreliable interpretation of core measurements. Therefore, quantifying the impact of environmental effects such as humidity is a required step toward improved core analysis and reservoir characterization. Clay minerals are abundant in mudrocks and are considered highly sensitive to environmental conditions. Previous research has shown that humidity significantly affects the hydration of montmorillonite (Cases et al., 1992, 1997; Berend et al., 1995). The hydration of clay minerals has significant influence on laboratory measurements for assessment of water saturation, especially in rock samples with high concentrations of clay minerals (Bush et al., 1970; Mooney et al., 1952). NMR T_2 measurements, which are sensitive to the presence of fluids, can be used for quantifying the volume of hydration water. TGA measures the changes in material mass as a function of increasing temperature, which provides information about dehydration, desorption, and dehydroxylation (Doyle 1961; Handwerger et al., 2012). Therefore, a combination of two techniques potentially can quantify the impact of humidity on hydration of clay minerals.

1.1.4 Quantifying the CEC of Rocks

Rock-fluid interfacial electrochemical interactions determine the amount of positively charged ions per unit weight of dry rock, known as CEC (Johnson and Linke, 1978). CEC quantification is of great importance for evaluating the contribution of clay minerals and clay-bound water to the electrical conductivity of rocks, as well as for wettability characterization. Reliable assessment of CEC can, however, be challenging.

Methods such as wet chemistry (Chapman, 1965), multiple salinity (Mian and Hilchie, 1981), and membrane potential (Thomas, 1976) are the most common for quantifying CEC. However, these methods for CEC quantification are time consuming, are limited by approximations and calibration efforts, and require tedious laboratory work. Moreover, CEC reference tables (Carroll, 1969; Ellis and Singer, 2007) often have a wide range of uncertainty in CEC values. Bush and Jenkins (1977) introduced a method for CEC assessment that finds correlations between CEC and volume of hydration water. They compared CEC values from the wet chemistry method with the volume of hydration water and established an experimental correlation between them. However, this method was developed based on experimental results and empirical correlation, restricting its application in various types of formation.

1.2 Statement of Problem

NMR logging is a well-established technology for estimating porosity, pore-size distribution, and permeability in conventional reservoirs. However, the uncertainty

associated with these estimates can be significant in formations with complex pore structures, such as those with variable pore size and pore-network connectivity. In such cases, it is often impossible to evaluate pore connectivity and detect isolated pores using well-log measurements and conventional methods for interpretation of NMR measurements. I approached this challenge by introducing contrast agents to enhance the sensitivity of NMR measurements to the presence of natural fractures and isolated pores.

Superparamagnetic iron oxide nanoparticles (SPIONs) have many interesting properties, such as superparamagnetism, high field irreversibility, and high saturation field, and they have been used successfully as contrast agents in medical drug delivery and MRI. Similar to their application in medical science, magnetic nanoparticles can also be used as contrast agents to improve the interpretation of rock NMR relaxometry. The influence of contrast agents on NMR T_2 distribution is based on the same mechanism as in MRI. Because magnetic nanoparticles accelerate the relaxation of proton spins, the T_2 peaks of nanoparticle-bearing pores/fractures would significantly shift to a short relaxation time. T_2 peak shifting depends on pore connectivity and pore-size distribution. Therefore, comparing the NMR T_2 distribution before and after contrast agent invasion can help interpret the interconnectivity of the pore space and natural fractures.

Injecting magnetic nanoparticle contrast agents enables to distinguish the isolated and interconnected pores using NMR measurements. This approach, however, can be challenging for evaluating carbonate formations because of electrostatic attraction between the surface of carbonate minerals and nanoparticles, which causes aggregation

of nanoparticles on the surface of minerals. I used a manganese-bearing solution as a contrast agent and conducted NMR measurements before and after injection of the solution. This method enables quantification of the interconnected pores and isolated pores on NMR T_2 relaxation distribution. For field application, I injected the manganese-bearing solution via doping the drilling mud with manganese chloride and investigating NMR logging data obtained before and after the use of manganese-doped drilling mud. This method potentially can improve the assessment of permeability using NMR measurements.

In addition, during NMR measurements of organic-rich mudrock samples, I found the total volume of fluid in the same mudrock sample to vary significantly when the rock sample was exposed to the atmosphere. I realized that clay minerals are abundant in mudrocks and are considered highly sensitive to relative humidity. Previous research has shown that humidity significantly affects the hydration of clay minerals, especially montmorillonite (Cases et al., 1992, 1997; Berend et al., 1995). Even though the influence of humidity on the hydration of clay minerals has been discussed in previous publications, the impact of humidity on core analysis and measurements for assessment of fluid-bearing porosity in porous media has not been quantified systematically. Therefore, I quantitatively and qualitatively evaluated hydration water at different humidity levels using NMR measurements.

Moreover, humidity experiment results show that the volume of hydration water is related strongly to the CEC of clay minerals during evaluation of hydration water at different humidity levels. This strong relationship was reported by Bush and Jenkins

(1977). However, they developed an empirical correlation lacking a physical model to describe the correlation between CEC and volume of hydration water. Therefore, I analytically established a correlation between CEC and volume of hydration water and developed a new method for quantifying the CEC of clay minerals based on the volume of hydration water quantified by NMR measurements. I also applied a new workflow that incorporates the new model, an inversion algorithm, and quantitative X-ray diffraction (XRD) to evaluate CEC in shaly sand and organic-rich mudrock formations.

1.3 Research Objectives

This work focuses on improving the existing and developing new NMR techniques for enhanced of petrophysical properties such as pore-network connectivity, isolated and interconnected porosity, permeability, and CEC in formations with complex pore geometry. The detailed objectives pursued by this research are as follows:

1. Introduce SPIONs as contrast agents for NMR interpretation of pore-network connectivity:
    a. Synthesize superparamagnetic nanoparticles;
    b. Characterize the magnetic properties and NMR T_2 response of nanoparticles;
    c. Quantify the variation of NMR T_2 relaxation time after injection of nanoparticles in different types of rocks;
    d. Quantify the pore-network connectivity of the rock with the aid of nanoparticles.

2. Improve NMR-based permeability assessment using a manganese-bearing solution as an NMR contrast agent:
    a. Characterize the NMR T_2 response of the manganese-bearing solution;
    b. Quantify interconnected porosity and isolated porosity in complex carbonate formations using the proposed manganese-bearing contrast solution;
    c. Introduce a new NMR-based permeability model, and evaluate the permeability of the carbonate rock samples;
    d. Cross-validate the improved NMR-based permeability against the Klinkenberg permeability of the rock samples.
3. Investigate the impact of humidity on the core measurement and analysis in unconventional formations:
    a. Prepare different relative humidity conditions using different saturated solutions, and conduct the hydration process on pure clay minerals and organic-rich mudrocks;
    b. Develop a workflow for measuring the T_2 distribution of hydration water;
    c. Investigate the TGA results of pure clay minerals, and compare them with the volume of hydration water from NMR measurements;
    d. Quantify the impact of hydration water on the NMR-based estimates of porosity in organic-rich mudrock formations.
4. Develop a new method to estimate the CEC of pure clay minerals using NMR-based estimates of volume of hydration water:

a. Investigate and analytically quantify the correlation between CEC and volume of hydration water in pure clay minerals;
b. Establish an analytical correlation for quantifying the CEC of pure clay minerals;
c. Test the performance of the new method on pure clay minerals including montmorillonite, illite, chlorite, and kaolinite;
d. Compare the CEC estimates from the new method against directly measured CEC from the wet chemistry method to validate the reliability of the new method.

5. Extend the application of the new method for CEC quantification in rocks with complex minerology and multiple types of clay minerals:
   a. Propose an inversion algorithm to quantify volume of hydration water and surface area for each mineral in the rock;
   b. Introduce a workflow to quantify CEC of each mineral using the volume of hydration water and surface area for each mineral in the rock;
   c. Calculate the equivalent CEC of rocks based on the CEC calculated for each mineral and the weight concentrations of minerals;
   d. Compare the CEC estimates from the new method against those from the wet chemistry method, the membrane potential method and the literature-reported values to verify the reliability and feasibility of the new workflow for CEC assessment in rocks with complex mineralogy.

1.4 Outline of Dissertation

Following the introduction chapter, the dissertation includes six additional chapters. Chapter II introduces magnetic nanoparticles as contrast agents for NMR measurements to improve characterization of interconnected porosity and fractures in multiple-porosity rocks. In this chapter, I present applying the new method to sandstone and fractured organic-rich mudrock samples.

Chapter III focuses on the use of a manganese-bearing solution as an NMR contrast agent for characterizing isolated pores in complex carbonate formations. This chapter also introduces a method to calculate the geometric mean of T_2 distribution and free-fluid volume over bound-fluid volume index after correcting for the impact of isolated pores. Then, the improved NMR-based permeability model is presented for assessing permeability. The reliability of the new method is cross-validated using directly measured permeability.

Chapter IV presents the investigation and quantification of the volume of hydration water in clay minerals based on NMR and TGA measurements. The clay minerals were exposed to water vapor at different relative humidity levels. The investigation of the influence of hydration on assessment of fluid volumes in organic-rich mudrocks was conducted using NMR measurements.

Chapter V elaborates on the analytical calculation of the CEC of pure clay minerals based on the energy balance between chemical potential energy and electric potential energy. The NMR, XRD, and nitrogen adsorption-desorption isotherm

measurements were carried out to quantify different input parameters for the analytical correlation to calculate CEC values. The CEC estimates from the new method then were cross-validated against directly measured CEC from the wet chemistry method.

Chapter VI presents the development of a new workflow to extend the application of the new method (established in Chapter V) to rocks with complex minerology and multiple types of clay minerals, including shaly sand formations and organic-rich mudrock formations. The new workflow incorporates quantitative characterization of rock composition (quantitative XRD) and an inversion algorithm to quantify the CEC of each mineral in the powdered rock samples. The reliability of the introduced workflow was verified using the wet chemistry method, the membrane potential method, and the literature-reported results.

In the end, Chapter VII summarizes the concluding remarks for this dissertation and recommendations for future work.

CHAPTER II

APPLICATION OF MAGNETIC NANOPARTICLES AS CONTRAST AGENTS FOR NMR MEASUREMENTS ON ASSESSMENT OF INTERCONNECTED POROSITY IN MULTIPLE-POROSITY ROCKS*

Nuclear magnetic resonance (NMR) measurements are considered among the most reliable methods to evaluate porosity and pore-size distribution in fluid-bearing rocks. However, in reservoirs with complex pore geometry, there is still a challenge to accurately interpret NMR relaxometry data to evaluate petrophysical properties of these reservoirs such as interconnected porosity. In this chapter, I introduce the application of nanoparticle contrast agents to improve assessment of interconnected porosity using NMR measurements. The comparison of NMR relaxometry data before and after nanoparticle injection enables distinguishing connected and isolated pore volumes, which might not be possible in the absence of contrast agents. The use of these contrast agents has been demonstrated successful in the Magnetic Resonance Imaging (MRI) technique for clinical diagnosis.

I used superparamagnetic iron oxide nanoparticles (SPION) as contrast agents injected into rock samples with multiple-porosity system (including intra-/inter-granular

---

* Modified and Reprinted with the permission from "Improved assessment of interconnected porosity in multiple-porosity rocks by use of nanoparticle contrast agents and nuclear-magnetic-resonance relaxation measurements" by Lu Chi, Kai Cheng, and Zoya Heidari, 2016, *SPE Reservoir Evaluation & Engineering*, Copyright 2018 by SPE whose permission is required for further use.

pores and natural fractures) and then quantified their impact on NMR measurements using laboratory experiments and numerical simulations. I injected contrast agents in sandstone and organic-rich mudrock samples and measured NMR T_2 (spin-spin relaxation time) distributions before and after contrast agent injection.

The results show that the comparison of NMR relaxometry data before and after SPION injection improves characterization of interconnected porosity and connectivity of natural fractures in rock samples with complex pore geometry. I observed that the long-relaxation-time peaks in NMR T_2 distribution significantly shifts to short-relaxation-time after SPION injection, indicating that inter-connected large pores/fractures are most easily invaded by SPION. However, the original short-relaxation-time peaks remained at the same position with almost the same amplitude and shape, indicating that small pores are not invaded by SPION. The accumulative porosity of the rock remains almost the same before and after SPION injection, indicating that SPION invasion in the rock only results in the down-shifting of T_2 relaxation time, but does not affect the NMR estimates of total porosity. I conclude from the experimental results that inter-connected large pores/fractures, isolated large pores, and small pores can be differentiated in NMR T_2 distribution with the aid of contrast agents. The outcomes of this research are promising for the successful application of the introduced technique for pore characterization in heterogeneous multiple-porosity systems containing natural fractures.

2.1 Introduction

The developments in NMR and MRI technology significantly influences chemistry, medical science, and petroleum industry. One of the remarkable developments in medical sciences is the use of contrast agents (Weinmann et al. 1984), such as superparamagnetic iron oxide nanoparticles (SPION), to improve the contrast in MRI images. The contrast agents relax the proton spins in liquids extremely fast during MRI scans, thus they appear as dark spots in MRI images and assist diagnostic decisions. SPION have been actively investigated as MRI contrast agents for decades (Renshaw et al. 1986; Weissleder et al. 1995). Their applications such as those used for imaging bowel and liver/spleen, have been proven to be successful for a long time (Bonnemain et al. 1998; Wang et al. 2001). The successful application of these contrast particles in medical sciences is promising for possible environmental-friendly applications in the petroleum industry for better characterization of challenging formations.

In the petroleum industry, borehole NMR measurements have shown success in evaluation of porosity and pore size distribution in fluid-bearing formations. In the fast diffusion limit, the NMR spin-spin relaxation time, T_2, of proton spins in the saturating fluids of porous media, can be expressed as (Coates et al. 1999)

$$\frac{1}{T_2}=\frac{1}{T_{2B}}+\frac{1}{T_{2S}}+\frac{1}{T_{2D}}=\frac{1}{T_{2B}}+\rho_2\left(\frac{S}{V}\right)_{pore}+\frac{Diff\left(\gamma\cdot G\cdot TE\right)^2}{12}, \tag{2.1}$$

where T_{2B} is the bulk relaxation time, T_{2S} is the surface relaxation time, and T_{2D} is the diffusion-induced relaxation time, respectively. In the expressions for T_{2S} and T_{2D} on the

right-hand side, ρ_2 is the surface relaxivity of grains, *S/V* is the surface-to-volume ratio of the pore space, *Diff* is the diffusion coefficient of pore fluids, γ is the gyromagnetic ratio of proton nuclei, *G* is the internal magnetic field gradient, and *TE* is the inter-echo spacing time of Carr-Purcell-Meiboom-Gill (CPMG) pulse sequence. The CPMG pluse sequence is the type of spin echo pulse sequence consisting of a 90° radio frequency pulse followed by an echo train induced by successive 180° pulses and is useful for measuring T_2 weighted images (Abragam 1961).

It has been widely accepted that the NMR T_2 distribution represents the pore size distribution of the rock, and the area under the T_2 distribution curve is proportional to the total porosity in the rock (Coates et al. 1999). However, reliable assessment of interconnected porosity in complex formations still remains challenging. To differentiate the movable fluids from irreducible fluids, the common method is to select a cutoff T_2 value on NMR T_2 distribution. For instance, 90 msec is a commonly-used T_2 cutoff value to distinguish movable and irreducible fluids in carbonate samples in the Coates permeability model (Coates et al. 1997). However, this T_2 cutoff value requires adjustments for different rock types and has a wide range of variety, e.g. from 18.3 msec to 1072 msec (Chen et al. 2008). Therefore, a direct NMR-based evaluation of pore connectivity in any given rock type with minimal calibration effort is desired to enhance formation evaluation.

Similar to the approach of using contrast agents in medical imaging, I propose that the interpretation of rock NMR relaxometry can be improved with the aid of contrast agents. The influence of contrast agents on NMR T_2 distribution is based on the

same mechanism as in MRI, but illustrated differently. Since SPION accelerate the relaxation of proton spins, the T_2 peaks of SPION-bearing pores/fractures would significantly shift downwards. The T_2 peak shifting depends on the pore connectivity, pore size, and fluid flow path. Therefore, comparison of the NMR T_2 distribution before and after contrast agent invasion can be used to interpret the inter-connection of the pore space and natural fractures.

NMR log-inject-log (LIL) method has been previously introduced to use paramagnetic ions (e.g., Mn2+) doped brine for quantifying residual oil saturation in the petroleum industry (e.g., Neuman 1983; Horkowitz et al. 1995; Crowe et al. 1997; Funk et al. 2004; Schulz et al. 2011; Toumelin et al. 2012). LIL method has not been previously used for improving pore connectivity assessment. Furthermore, I propose the use of SPION instead of other contrast agents such as paramagnetic ions. The first reason for this choice is the size of SPION that restricts the contrast agents flow into the relatively large pores. This characteristic improves investigating fracture connectivity in tight formations, such as organic-rich mudrocks, where SPION can only flow true fractures and not the pore network. The second reason is that SPION are more environmentally friendly compared to paramagnetic ion doped brine.

Previous publications reported that the nanoparticles can transport in the near wellbore porous media (Lecoanet et al. 2004; Rodriguez et al. 2009; He et al. 2009). Yu (2012) conducted coreflood experiments to test the dispersion of nanoparticles in rock samples and quantified the mechanism of nanoparticle transport in porous media using laboratory experiments. Kanj et al. (2009) carried out nanofluid coreflood experiments in

a formation in Saudi Arabia and validated nanoparticle transport in reservoir rocks. Yu et al. (2012) studied the adsorption and transportation behavior of silica nanoparticles in different porous media. The results of the previous publications, confirming the feasibility of nanoparticle transport in the porous media, are promising for the application of SPION contrast agents in formation evaluation.

I performed NMR laboratory experiments to improve characterization of interconnected pore volume using nanoparticle contrast agents (i.e. SPION). I started with synthesizing SPION and preparing SPION solutions at different concentrations. I then saturated the samples with the SPION solution at different concentrations of nanoparticles. Then I carried out laboratory NMR measurements and compare the NMR T_2 distribution before and after SPION invasion. The upcoming sections described the methods in detail and show the NMR experimental results for actual rock samples.

2.2 Method

2.2.1 Preparation of SPION

I prepared SPION using the solvothermal chemical methods (Cheng et al. 2014; Cheng et al. 2012). These nanoparticles are negatively charged at the surface (Cheng et al. 2012), which decrease the chance of particle accumulation in the pore space. The main composition of the nanoparticles is iron oxide. The nanoparticles have a diameter between 60 and 70 nm. **Fig. 2.1** shows the Transmission Electronic Microscope (TEM) images of these particles. The nanoparticles have high saturation magnetization of

approximately 33.2 emu/g. A previous publication documented the superparamagnetic properties of these nanoparticles (Cheng et al. 2014). SPION solution are soluble in water but not in oil. When this solution is injected into the porous media, it will displace the in-situ fluids in the pore space, gets mixed with formation, and invades the connected pore network.

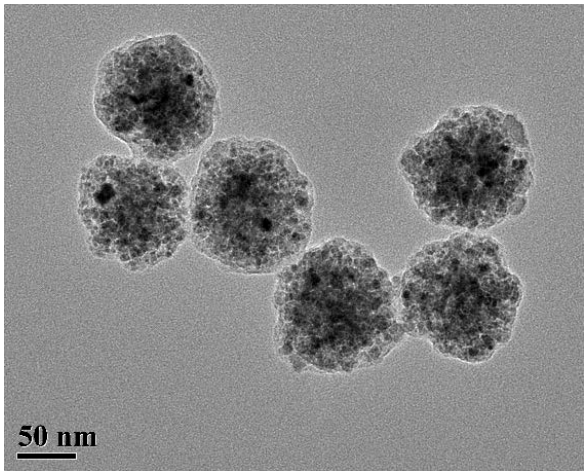

Fig. 2. 1 TEM image of the synthesized SPION.

I dispersed 0.1 gram SPION powder in 20 mL deionized water and prepared the standard SPION solution at the concentration of 5 kppm. The standard SPION solution was then diluted and solutions with different concentrations of nanoparticles (i.e., 125 ppm, 100 ppm, 50 ppm, 40 ppm, 30 ppm, 20 ppm, 10 ppm, and 5 ppm) were prepared to measure the relaxivity performance of the SPION solution. The SPION solutions at the concentrations of 20 ppm and 50 ppm were used to saturate the rock samples for coreflood experiments.

2.2.2 Preparation of Rock Samples

I used sandstone and organic-rich mudrock samples for the laboratory experiments. The three sandstone rock samples (SS1, SS2, and SS3) are from a homogeneous sandstone formation. These samples are 1 inch in diameter and 1.5 inches in length. **Fig. 2.2a** shows one of the three sandstone samples. Sandstone rock samples are dried at 90 ºC for two hours. The organic-rich mudrock sample used for laboratory experiments is 1 inch in diameter and 1.5 inches in length. I synthetically created three planar fractures in the sample along the longitudinal axis (**Fig. 2.2b**). The fractures were approximately 1 mm in thickness.

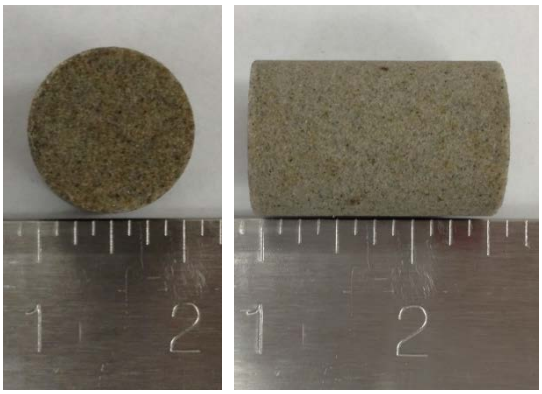

(a)

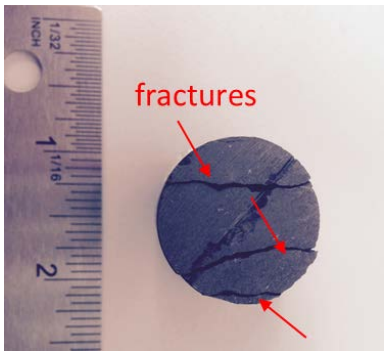

(b)

Fig. 2. 2 (a) One of the sandstone samples and (b) the organic-rich mudrock sample with planar fractures used for laboratory NMR experiments.

To fully saturate the sandstone rock samples with deionized water or SPION solutions, I carried out coreflood experiments in a triaxial core holder. I increased the volume of fluid injection until the concentration of outflowing nanoparticles stayed constant. I assumed that the sandstone samples were fully saturated with the nanoparticle solution after four pore-volumes of injection. The effluent fluid was monitored to check the moment of breakthrough, and the coreflooding process was stopped after four pore-volumes of injection.

In the case of fractured organic-rich mudrock, I only saturated the fractures of the sample by adding brine or SPION solution into the fracture space. In a previous publication, I showed that in the case of organic-rich mudrocks, SPION do not penetrate pore network of the rock and mainly saturate the fractures (Cheng et al. 2014), which can potentially enable fracture characterization. Furthermore, the diameter of SPION is between 60 and 70 nm, which is larger than the pore size (i.e., 10 to 30 nm) of the organic-rich mudrock (Al-Bazali et al. 2005). Consequently, they only transport in the fractures of the mudrock formations.

2.2.3 NMR Measurements

The NMR laboratory measurements were conducted using a 2 MHz NMR benchtop spectrometer. The T_2 relaxation measurements were carried out using a CPMG pulse sequence. For the bulk fluids, I set the inter-echo spacing time (TE) of the CPMG pulse sequence as 200 μsec. The signal-to-noise ratio (SNR) of the measurement was more than 2000 after 16 scans. In the case of sandstone rock samples, I used the same

TE of 200 μsec, which is short enough for capturing fluid signals in sandstone formations, and set target SNR and number of scans to 500 and 300, respectively, due to relatively weak signals in core samples. In the case of organic-rich mudrock sample, I set TE to 100 μsec and target SNR to 200 to be able to capture the signals from small pores. Each measurement was conducted more than three times to guarantee repeatability of the measurements.

2.3 Results

2.3.1 Bulk T_2 Relaxation Time of SPION Solution

I measured the bulk T_2 relaxation time of deionized water and SPION solutions with different concentrations of nanoparticles. The fluids were scanned in GeoSpec2 NMR spectrometer. **Fig. 2.3** shows the measured bulk T_2 relaxation rate of SPION solutions with different concentrations of nanoparticles. I observed that the bulk T_2 relaxation rate (i.e. inverse of bulk T_2 relaxation time) of SPION solution is linearly proportional to the concentration of SPION. Previous studies also reported the linear relationship between the proton relaxation rate and the concentration of paramagnetic components (Weinmann et al. 1984; Rosen et al. 1990), given by

$$Rate = \frac{1}{T_2} = Rate^0 + rCon, \tag{2.2}$$

where *Rate* is the relaxation rate of fluid with paramagnetic component, $Rate^0$ is the relaxation rate without contrast agent, *r* is relaxivity constant, and *Con* is the concentration of paramagnetic components. The relaxivity constant is determined by the

paramagnetic components and represents the performance of these components as contrast agents. The linear correlation shown in **Fig. 2.3** provides high relaxivity constant of 0.91 $ppm^{-1} \cdot sec^{-1}$ for the proposed nanoparticles, which is promising for a measurable influence of these particles on NMR measurements.

By substituting **Eq. 2.2** into **Eq. 2.1**, the T_2 relaxation time of the SPION solution in porous media can be written as

$$\frac{1}{T_2} = \left(R^0 + rC\right) + \rho_2 \left(\frac{S}{V}\right)_{pore} + \frac{D\left(\gamma \cdot G \cdot TE\right)^2}{12}, \tag{2.3}$$

where T_2 distribution is presented as a function of concentrations of SPION in the solution.

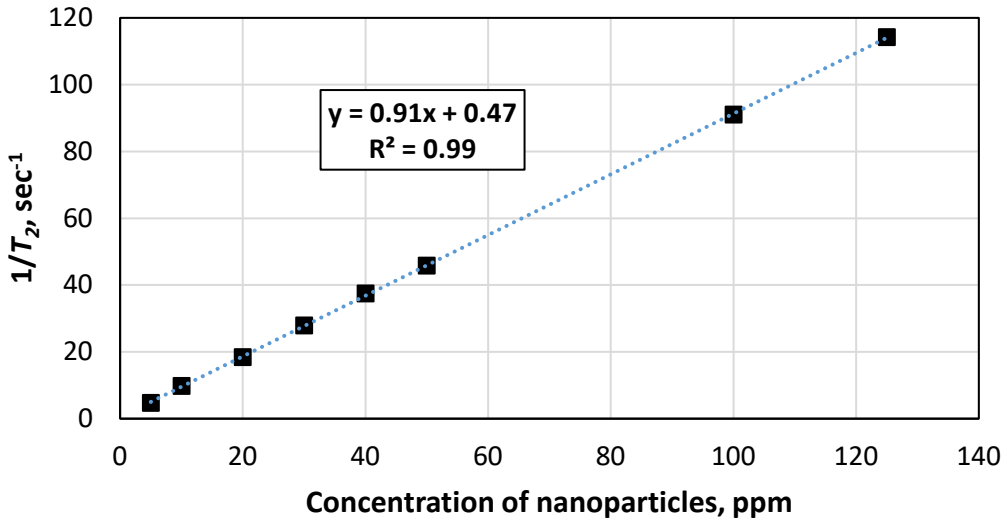

Fig. 2. 3 The experimentally measured linear relationship between NMR T_2 relaxation rate ($1/T_2$) and concentration of SPION solution.

Fig. 2.4a shows two tubes of SPION solutions and one tube of deionized water, which were used to saturate the rock samples. The concentrations of SPION in the

solutions are 20 ppm and 50 ppm, respectively. **Fig. 2.4b** shows the measured bulk T_2 relaxation times for the deionized water (blue line) and the SPION solutions (green dashed-dotted and red dashed lines for 50 ppm and 20 ppm SPION solution, respectively). The measured bulk T_2 times of 50 ppm SPION solution, 20 ppm SPION solution, and deionized water are 19.95 msec, 50.12 msec, and 2619 msec, respectively.

(a)

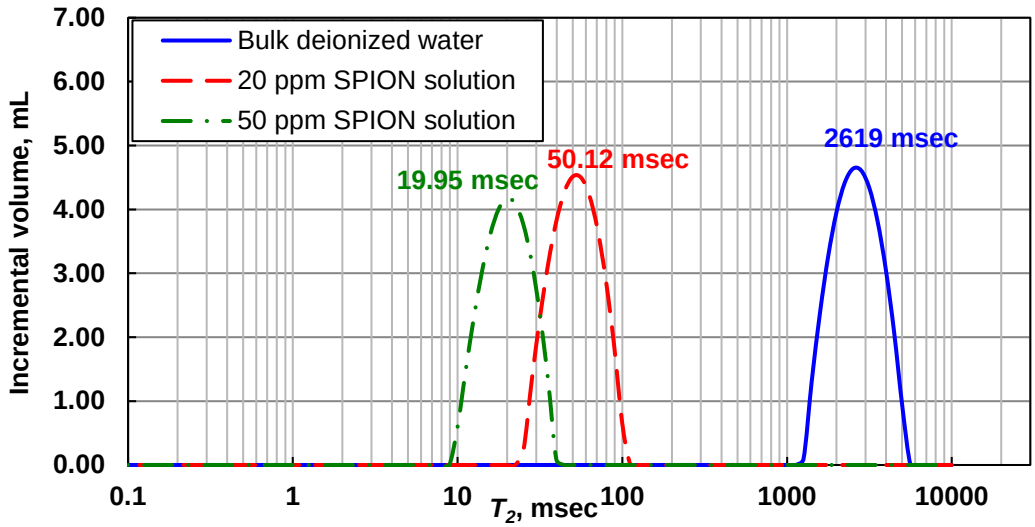

(b)

Fig. 2. 4 (a) Three containers of 50 ppm SPION solution, 20 ppm SPIO solution, and bulk deionized water and (b) measured NMR T_2 distribution for 50 ppm SPION solution (green dashed-dotted line), 20 ppm SPION solution (red dashed line), and deionized water (blue solid line).

2.3.2 Sandstone Rock Samples

The porosity of the sandstone rock samples used for laboratory experiments, SS1, SS2, and SS3 was approximately 14%. I first fully saturated all three sandstone samples by deionized water using coreflooding and measured NMR T_2 distribution for these samples. I then conducted coreflood experiments using SPION solutions and measured NMR T_2 distribution again. For SS1 and SS2 rock samples, I conducted the NMR measurements T_2 hours after coreflooding. To investigate the effect of deposition of nanoparticles on the grain surface, I extended the resting time to 36 hours in the case of SS3 rock sample.

Fig. 2.5 shows the NMR T_2 distribution of the SS1 sample saturated with water (thick blue line) and with 20 ppm SPION solution (thick red line). The T_2 peak at 354.8 msec in the blue line represents the large pores in the original sandstone rock sample. After flooding the sample with 20 ppm SPION solution, the T_2 peak shifts to 39.8 msec. Meanwhile, the T_2 peak in the short T_2 region (i.e., approximately 0.7 msec) remained at the same position with almost the same amplitude and shape. These observations indicate that highly-connected inter-granular pores in the sandstone rock sample are easily invaded by SPION, while small pores might not be influenced by SPION. I observed that the total porosity of the rock before and after flooding of SPION solution remains almost the same at 13.5% (thin blue and red lines on the right vertical axis), indicating that SPION invasion in the rock does not affect the estimates of total porosity from NMR measurements. The reason for the persistent porosity estimates is that the proton spins in water are excited at time 0 to generate the initial magnetization signal.

Although the SPION relax the proton spins in the fluids T_2 fast, they do not kill the magnetization signal at the beginning and only change the T_2 distribution. Thus, the total porosity measured by NMR remains the same, but the T_2 distribution is changed after the injection of nanoparticles.

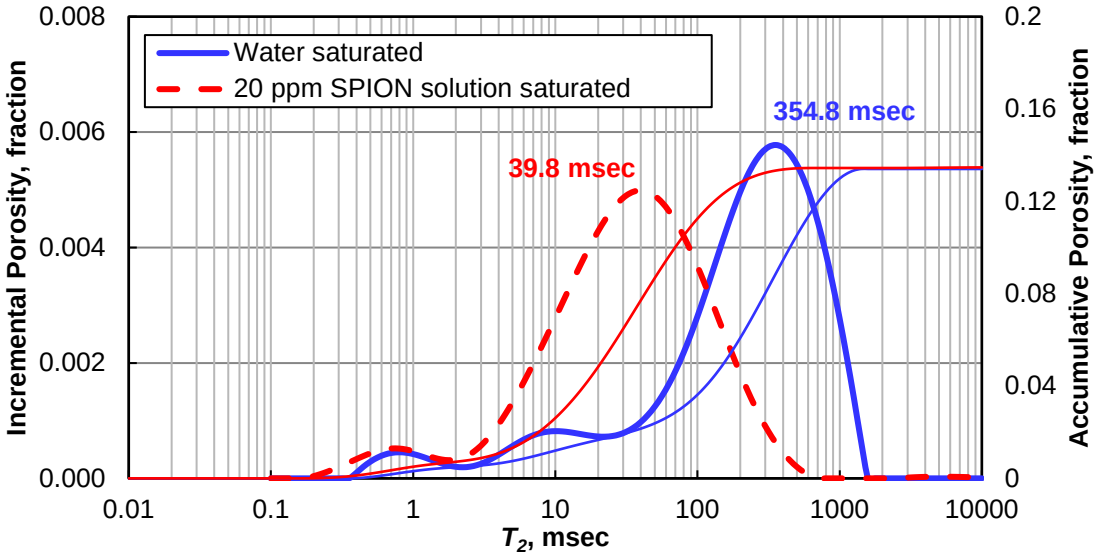

Fig. 2. 5 Sandstone rock samples: Experimental NMR T_2 distribution and accumulative porosity of SS1 after getting saturated by deionized water (blue lines), and 20 ppm SPION solution (red dashed lines).

Next, I investigated the influence of SPION concentration on T_2 distribution by using 50 ppm SPION solution in the sandstone rock sample SS2. **Fig. 2.6** shows that after saturating SS2 with 50 ppm SPION solution, the T_2 peak of SS2 further shifts downwards to 15.8 msec. Comparison of results in Figs. 2.5 and 2.6 shows that the change in concentration of SPION significantly affects the T_2 distribution.

I further investigated the influence of the deposition/separation of SPION in the rock using the sandstone rock sample SS3. I conducted the NMR measurements 36

hours later after coreflooding the rock sample using 20 ppm SPION solution. **Fig. 2.7** shows the NMR T_2 distribution of sandstone rock SS3 before (blue) and after (red line) coreflooding with the 20 ppm SPION solution. I obtained a similar NMR T_2 peak downward-shift as that shown in Fig. 2.5. However, the T_2 peak was shifted to 89.1 msec, and the curve shape was distorted. The reason can be the deposition of SPION on the grain surface after 36 hours. Since SPION are less suspended in the fluid after deposition, the bulk T_2 of SPION solution adopts a value higher than 50 msec, but still much lower than bulk T_2 of deionized water (i.e., approximately 3 sec).

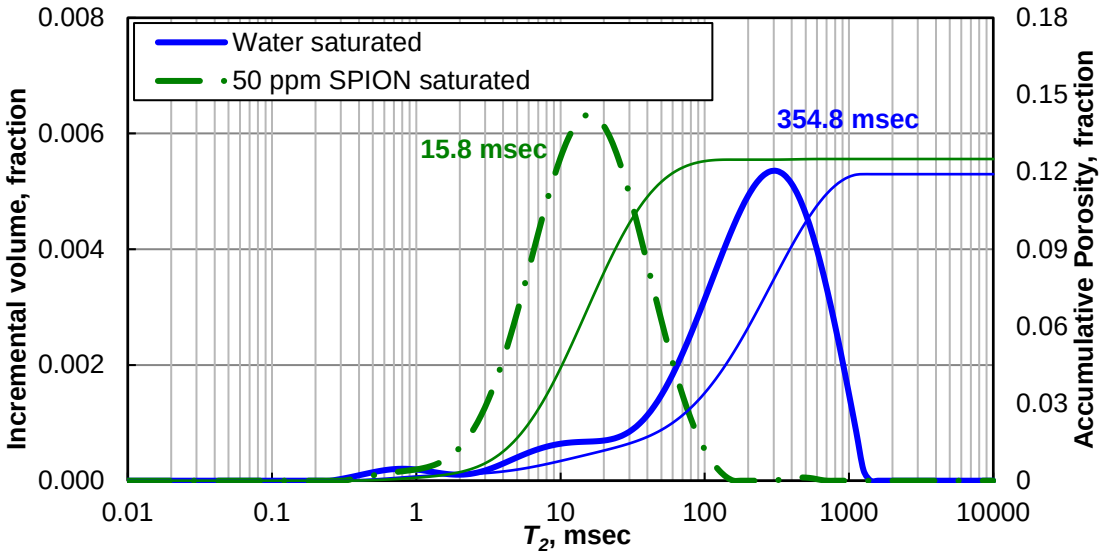

Fig. 2. 6 Sandstone rock sample: Experimental NMR T_2 distribution and accumulative porosity of SS2 after getting saturated by deionized water (blue lines), and 50 ppm SPION solution (green dashed-dotted lines).

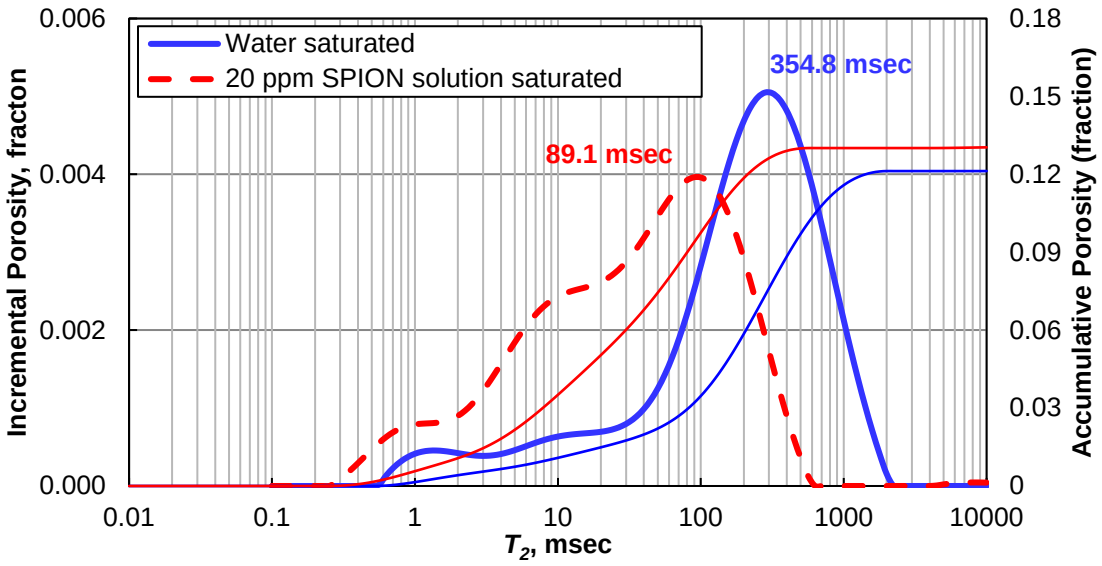

Fig. 2. 7 Sandstone rock sample: Experimental NMR T_2 distribution and accumulative porosity of SS3 after getting saturated by deionized water (blue lines), and 20 ppm SPION solution (red dashed lines). The 20 ppm SPION saturated result was obtained 36 hours after coreflooding.

2.3.3 Organic-Rich Mudrock Sample

In this case, I investigate the possibility of differentiating the connected and isolated fractures using the introduced method. I saturated the fractured mudrock samples first with brine and then with 20 ppm SPION solution.

Fig. 2.8a shows the comparison between the experimental NMR T_2 distributions of the original fractured mudrock when fractures are not saturated (black line), and after saturating fractures with brine (blue line). The original mudrock (black line) shows a T_2 peak in the short T_2 region at 0.2 msec, representing the clay-bound water and irreducible hydrocarbon in nano-scale pores, which is commonly seen in organic-rich mudrocks. The results for the brine-saturated mudrock (blue line) shows a strong T_2 peak in the long T_2 region at 1412.5 msec, in addition to the original T_2 peak at 0.2 msec,

which represents the brine-saturated fractures. However, it does not share any information about connectivity of these fractures. The black and blue dashed curves show the measured cumulative porosity for the original and brine-saturated mudrock sample, respectively. The total porosity increased from 0.017 to 0.029 after saturating the fractures with brine.

I then replaced the brine with a 20 ppm SPION solution in the fracture network, first partially-saturated two fractures, then fully-saturated all three fractures. **Fig. 2.8b** shows the comparison between the measured NMR T_2 distributions of the organic-rich mudrock sample with fractures fully-saturated with brine (blue), partially-saturated with SPION solution (red), and fully-saturated with SPION solution (green). The results from both the partially- and fully-saturated fracture network showed that the lower T_2 peak remained almost intact, indicating that the small pores in the mudrock matrix were not influenced by SPION solution. I observed a minor shift of the short T_2 peak to the left after injection of SPION solution to the rock. This minor shift can be caused by imbibition of water into the shale matrix, while nanoparticles still remain in the fractures. Meanwhile, in the case of partially-saturated result (red line), the upper T_2 peak related to the fractures shifted downwards to the range of 200 msec to 1000 msec; while in the case of fully-saturated fractures (green line), this peak shifted further to 79.4 msec. These observations can be explained by the fact that SPION invade into the interconnected fracture network and significantly alter the bulk relaxation rate and the surface relativity of the fractures. Furthermore, I obtained the same total porosity for the

three cases, demonstrating that the total porosity measurement was not influenced significantly by SPION invasion.

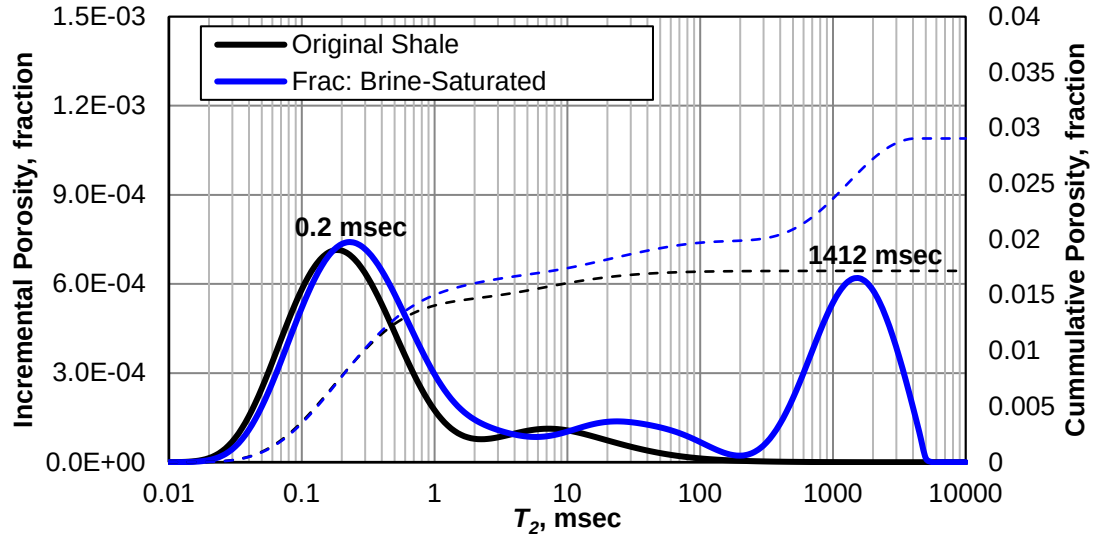

(a)

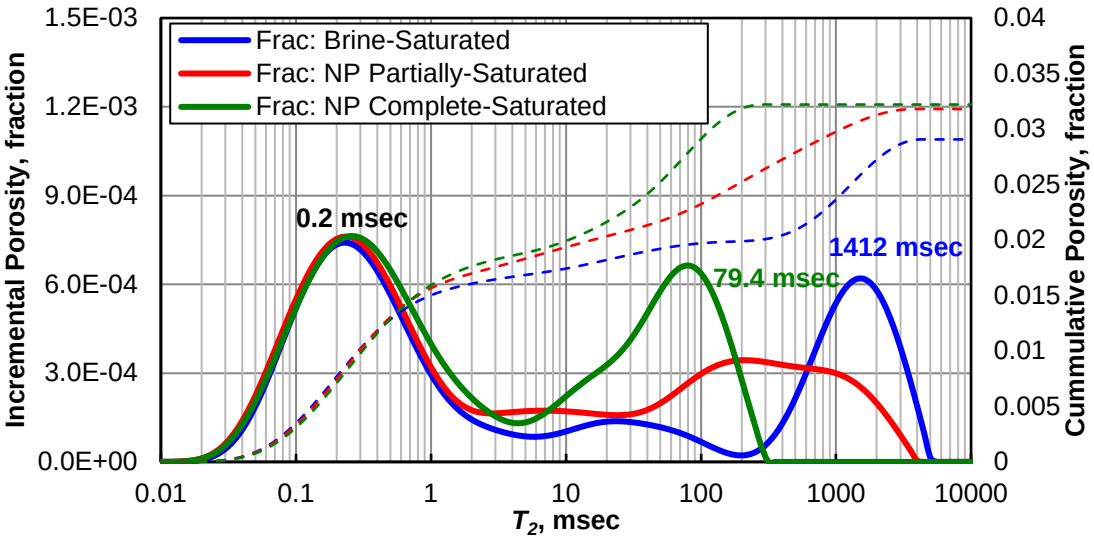

(b)

Fig. 2. 8 Organic-rich mudrock sample: Experimental NMR T_2 distribution and accumulative porosity of the organic-rich mudrock sample (a) before (black line) and after (blue line) saturating the fracture with brine water, and (b) fractures fully saturated with brine water (blue line), partially saturated with 20 ppm SPION solution (red line), and fully saturated with 20 ppm SPION solution (green line).

2.4 Conclusions

I investigated the possibility of combining contrast agents and NMR relaxometry for improved characterization of pore size distribution and interconnected porosity and fracture network in rocks. I showed the successful application of the proposed method for distinguishing isolated from connected pore/fracture network. I proposed the use of SPION as contrast agents for NMR measurements. The bulk T_2 relaxation time of the synthesized contrast agents (i.e. SPION) is influenced by the presence and concentration of SPION. The linear correlation between bulk T_2 relaxation rate and concentration of SPION was measured. The relaxivity constant of SPION is approximately 0.91 $ppm^{-1} \cdot sec^{-1}$, indicating a high relaxivity performance as contrast agents.

Experimental results of sandstone rock samples showed that long-relaxation-time peaks related to the large pores or fractures, which were easily invaded by contrast agents, shifted downwards significantly after injection of SPION solution; while the short-relaxation-time peaks related to the small pores remained almost intact after SPION injection, showing that small pores were not easily influenced by this particular contrast agent. In the case of fractured organic-rich mudrocks, the use of nanoparticles enables transport of nanoparticles only in connected natural fractures (not in the pore network) in the tight formations such as organic-rich mudrocks, which enables characterization of fracture network while keeping the signals from the pore network in the measurable range. I observed a downward shift of T_2 peaks from connected fracture after SPION injection, which demonstrated that SPION can help distinguishing

connected and isolated fracture networks in NMR measurements, and estimating the volumetric concentration (or density) of connected fractures in organic-rich mudrock formations.

The results from different rock types indicated that the use of contrast agents is promising to improve interpretation of NMR measurements to quantify interconnected porosity in formations with complex pore/fracture networks. This is the first time that magnetic nanoparticles contrast agents are utilized to improve borehole NMR measurements, including characterization of pore size distribution and pore connectivity in heterogeneous rock samples. The outcome of this research can enhance the petrophysical evaluation of heterogeneous rocks and can be later used to improve permeability assessment in complex carbonate and organic-rich mudrock formations by quantifying the connectivity of the pore and fracture network.

CHAPTER III

APPLICATION OF MANGANESE SOLUTION AS CONTRAST AGENT FOR NMR MEASUREMENTS ON ASSESSMENT OF PORE-NETWORK CONNECTIVITY AND PERMEABILITY IN CARBONATE FORMATIONS∗

Nuclear magnetic resonance (NMR) logging is a well-established technology for estimating porosity, pore-size distribution, and permeability in conventional reservoirs. However, the uncertainty associated with these estimates can be significant in complex heterogeneous carbonate reservoirs, such as those with variable pore size and pore network connectivity. In such cases, distinguishing isolated pore space is often impossible using well-log measurements and conventional well-log interpretation methods, which makes permeability evaluation unreliable. I propose a new application of the NMR log-inject-log method to improve assessment of permeability and to distinguish isolated pores from connected pores. I propose injecting manganese-bearing solution in the rock samples and simultaneously analyze NMR measurements before and after injection of the contrast solution. Injection of contrast agents enables eliminating the impact of isolated pore space from the NMR T_2 (spin-spin relaxation time) distribution, which is then used to improve permeability assessment.

∗ Reprinted with the permission from "Pore network connectivity and permeability assessment using NMR log-inject-log method" by Kai Cheng and Zoya Heidari, 2017, *SPE Reservoir Evaluation & Engineering*, Copyright 2017 by SPE whose permission is required for further use.

To confirm the feasibility of the proposed method for field applications, I conduct NMR laboratory measurements in two carbonate rock types. I inject manganese-bearing solution into rock samples using a coreflood experimental procedure and measure NMR T_2 distributions before and after injection. I then estimate isolated porosity and interconnected porosity by considering the difference between the NMR T_2 distributions acquired before and after the injection of the contrast solution. I introduce a method to calculate geometric mean of T_2 distribution for interconnected pores, and also to obtain effective free fluid volume and bound fluid volume. Finally, I use the T_2 distribution corrected for the impact of isolated pores in conventional NMR-based permeability models to improve permeability assessment. I cross-validate the NMR-based permeability estimates against Klinkenberg permeability measured by an unsteady-state gas permeameter. The results confirm that the proposed method enables quantifying the isolated and connected pore volume, and finally improves NMR-based permeability assessment. The new method provides estimates of permeability with up to 10% average error in eight carbonate rock samples, which was a significant improvement compared to the average errors of up to 500%, when T_2 distribution is not corrected for the impact of isolated pores.

3.1 Introduction

One of the important applications of NMR logging is permeability assessment. Among the borehole measurements, the NMR measurements typically estimate

permeability the most accurately, due to the correlation between T_2 (spin-spin relaxation time) distribution and pore size distribution (Seevers, 1966; Sen et al., 1990). The conventional NMR-based permeability models include the Coates model and the Schlumberger Doll Research (SDR) model. The SDR model is given by (Kenyon et al. 1986)

$$k_{SDR} = a \times T_{2gm}^2 \times \phi^4, \tag{3.1}$$

where ϕ is the porosity and a is a constant coefficient that depends on the rock type. T_{2gm} is the geometric mean of T_2 distribution, which is given by

$$T_{2gm} = \left[\prod_{i=1}^{n} (T_{2i})^{\phi_i} \right]^{\frac{1}{\sum_i^n \phi_i}}, \tag{3.2}$$

where T_{2i} is T_2 relaxation time at time interval i and ϕ_i is incremental porosity at each T_2 relaxation time T_{2i}.

The Coates model is represented via (Coates et al. 1997)

$$k_{coates} = \left[\left(\frac{\phi}{C} \right)^2 \times \left(\frac{FFI}{BVI} \right) \right]^2, \tag{3.3}$$

where C is an empirical constant that can be calibrated using independent core measurements, *FFI* is free fluid volume and *BVI* is bound fluid volume. The areas below the T_2 distribution curve below and above $T_{2cutoff}$ represent the bound fluid volume (*BVI*) and the free fluid volume (*FFI*), respectively. $T_{2cutoff}$ is typically equal to 33 msec and 100 msec for sandstone and limestone formations, respectively.

Both the Coates and the SDR models assume that the pore network is all connected and contribute to the permeability. However, some carbonate formations

contain isolated pores, such as large vugs and intragranular pores. NMR logging is not capable of identifying and quantifying such pore structures. In such cases, depending on the size of isolated pores, I might experience either underestimation or overestimation of permeability. For instance, the large vugs have long relaxation times and might be misinterpreted as large connected pores. Thus, the NMR-based permeability models will inevitably result in overestimation of permeability.

To avoid the influence of isolated pores in permeability estimation, Chang et al. (1997) modified the SDR model by introducing an empirical vugs model in which the T_2 relaxation time above 750 msec is considered as evidence of isolated vugs. After excluding the isolated vugs from the porosity and geometric mean T_2 calculation, permeability is given by (Chang et al. 1997)

$$k_{SDR,Chang} = a \times T_{2gm,<750ms}^2 \times \phi_{<750ms}^4, \tag{3.4}$$

where, $T_{2gm<750\,ms}$ is geometric mean of T_2 distribution with relaxation times of less than 750 msec and $\phi_{<750\,ms}$ is cumulative porosity calculated at T_2 relaxation time of less than 750 msec. However, this model use an approximate constant cutoff value for the long relaxation time (> 750 msec) to distinguish isolated vugs, which limits its application for different rock types.

Chen et al. (2008) introduced a pore connectivity coefficient, *p*, to eliminate the influence of vugs or intragranular porosity. The pore connectivity coefficient, *p*, is determined by the rock type and the depositional environments, which cannot be quantified easily. Previous publications (Cheng, et al., 2014; Chi, et al., 2015) demonstrated that injection of magnetic negatively-charged nanoparticle contrast agents

enables distinguishing the isolated and interconnected pores using NMR measurements. This approach can, however, be challenging to be used for evaluation of carbonate and tight formations, because of deposition of contrast agents and blockage of pore throats. Here, I propose the use of contrast manganese-bearing solution and conduct NMR measurements before and after injection of the solution. This method enables quantifying the interconnected pores and isolated pores on NMR T_2 relaxation distribution. For field application, I proposed the injection of manganese-bearing solution via doping the drilling mud with manganese chloride and investigation of NMR logging data obtained before and after using manganese doped drilling mud. By this means, this method can potentially improve the assessment of permeability using NMR measurements.

The NMR log-inject-log method has been previously introduced for quantifying residual oil saturation in field applications (e.g., Neuman 1983; Horkowitz et al. 1995; CroI et al. 1997; Funk et al. 2004; Schulz et al. 2011; Toumelin et al. 2012). The NMR log-inject-log method conducted via doping the drilling mud with manganese. Nevertheless, the application of the NMR log-inject-log method in improving permeability and pore connectivity assessment is new and can significantly enhance reservoir characterization in carbonate reservoirs with complex pore structure.

3.2 Method

I introduced a new application of NMR log-inject-log method for improving permeability assessment in formations with complex pore structure such as carbonates. The contrast solution proposed in this approach includes manganese-bearing solution. Laboratory NMR measurements are performed before and after injection of manganese-bearing solution, which enables correcting NMR T_2 distribution for the effect of isolated pore space. The corrected NMR T_2 distribution is then used in the SDR and the Coates models for improved permeability assessment.

3.2.1 Preparation of Rock Samples and Contrast Solution

I used rock samples from two carbonate rock types, C1 and C2, with different pore structures. The pore network is better connected in rock type C2. The porosity and permeability of carbonate rock type C1 is in the range of 3.0 % to 6.0 % and 0.1 mD to 1 mD, respectively. The isolated pores of rock type C1 is approximately 1.0 % to 2.0 % in porosity. The carbonate rock type C2 is more porous, permeable, and homogeneous compared to rock type C1, with porosity and permeability in the range of 12.0 % to 13.0 % and 1 mD to 10 mD, respectively. The isolated pores of rock type C2 is approximately 2.0 % in porosity. The two types of carbonate rock samples (C1 and C2) used here are 1 inch in diameter and 1.5 inches in length, as shown in **Fig. 3.1**.

I prepared solutions with different manganese ion (Mn^{2+}) concentrations (i.e., 0.01 g/L, 0.1 g/L, 0.3 g/L, 0.5 g/L, 1 g/L, 2.5 g/L, and 10 g/L) by dissolving $MnCl_2$ in

distilled water. I prepared 20 kppm brine using sodium chloride (NaCl) and distilled water.

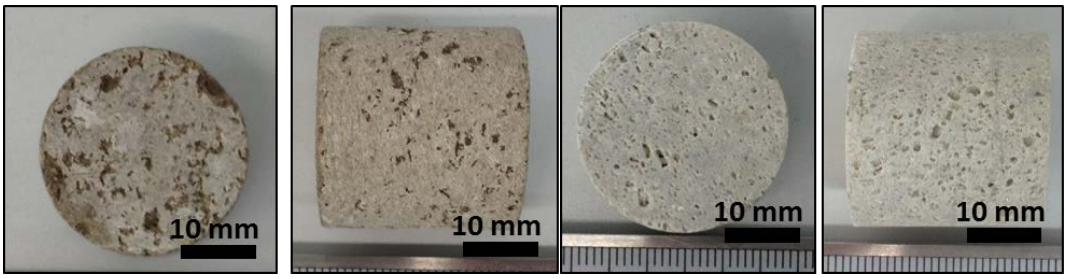

(a) (b)

Fig. 3. 1 (a) Carbonate rock type C1 and carbonate rock type C2 used for laboratory experiments.

3.2.2 Saturation of Rock Samples

For saturating the carbonate rock samples, I first immersed them in the previously prepared 20 kppm (NaCl) brine solution and kept them under vacuum pump for 4 hours as shown in **Fig. 3.2a**. I didn't observe the significant increase of water saturation after 4 hours' vacuum pumping. To guarantee that the rock samples are fully saturated, I used a coreflood equipment and injected the same brine into the rock samples which had already been saturated using the vacuum pump. I placed the rock samples in a triaxial core holder as shown in **Fig. 3.2b** and set the confining pressure between 500 and 1000 psi and the injection pressure between 100 psi and 500 psi. For saturating the rock samples with the manganese-bearing solution, I injected 10 g/L manganese-bearing solution into the samples, which displaced the brine in the pore space. To displace completely the original fluid using the coreflood experiment, I set the

flow rate to less than 0.3 ml/min and sustained injection for 30 minutes, which was approximately equivalent to injection of ten pore volumes.

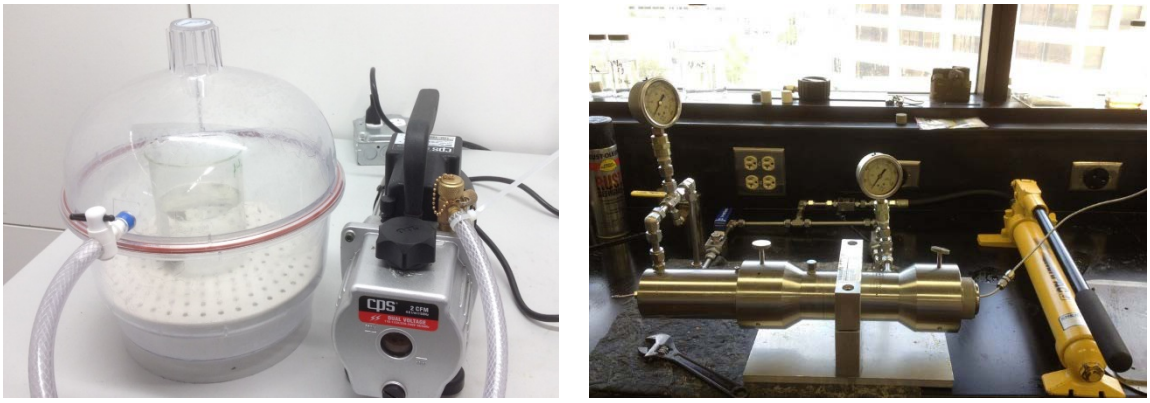

(a) (b)

Fig. 3. 2 Rock saturation apparatus: (a) vacuum system and (b) coreflood system.

3.2.3 NMR Measurements

I conducted NMR laboratory measurements using a 2 MHz benchtop NMR spectrometer. The T_2 relaxation measurements were carried out using a CPMG (Carr-Purcell-Meiboom-Gill) pulse sequence. To better capture the fluid signal of manganese-bearing solution, I set the inter-echo spacing time (TE) of the CPMG pulse sequence to 100 µsec. The signal-to-noise ratio (SNR) of the measurements was more than 200. The number of scans (NSA) depends on the total volume of fluid in the sample being measured. For the rock samples, the number of scans ranges from 200 to 500. I repeated each measurement more than three times to confirm the replicability of the measurements.

3.2.4 Correcting the Measured T_2 Distribution for the Effect of Isolated Pore Space

Before estimating permeability based on NMR measurements, I correct the measured T_2 distribution and the geometric mean of T_2 distribution for the effect of isolated pore space. The corrected T_2 distribution is then used in the SDR (**Eq. 3.1**) and the Coates (**Eq. 3.3**) models for permeability assessment.

The T_2 distribution of isolated pore space can be estimated after injection of manganese-bearing solution, which is given by

$$\phi_{i,iso} = \begin{cases} 0 & if\ T_2 < T_{2,critial} \\ \phi_{i,AI} & if\ T_2 \geq T_{2,critial} \end{cases}, \tag{3.5}$$

where $\phi_{i,iso}$ is incremental porosity of isolated pore space at each T_2 relaxation time T_{2i}, $\phi_{i,AI}$ is incremental porosity of isolated pore space at each T_2 relaxation time T_{2i} after injection of manganese-bearing solution, and $T_{2,critial}$ is critical T_2 relaxation time to distinguish isolated pores and interconnected pores. This critical value is affected by concentration of Mn^{2+} and rock type.

To calculate the updated geometric mean of T_2 distribution, I rewrite **Eq. 2** as

$$\sum_i^n \phi_i \cdot log\left(T_{2gm}\right) = \sum_i^n \left[\phi_i\, log\left(T_{2i}\right)\right]. \tag{3.6}$$

Equation 3.6 can be simplified to

$$\phi_{total} \cdot log\left(T_{2gm,total}\right) = \phi_{isolated}\, log\left(T_{2gm,iso}\right) + \phi_{inter}\, log\left(T_{2gm,inter}\right), \tag{3.7}$$

where ϕ_{total} is total porosity, ϕ_{iso} is isolated porosity, ϕ_{inter} is interconnected porosity, $T_{2gm,total}$ is geometric mean of T_2 distribution of total pore space, $T_{2gm,iso}$ is geometric mean of T_2 distribution of isolated pore space, and $T_{2gm,inter}$ is geometric mean of T_2

distribution of interconnected pore space. The geometric mean of T_2 distribution of interconnected pore space is then given by

$$T_{2gm,inter} = \left[\frac{\left(T_{2gm,total}\right)^{\phi_{total}}}{\left(T_{2gm,isolated}\right)^{\phi_{isolated}}} \right]^{\frac{1}{\phi_{inter}}}, \quad (3.8)$$

where $T_{2gm,total}$ can be calculated using T_2 distribution before injection of manganese-bearing solution. $T_{2gm,iso}$ can be calculated using **Eq. 3.2** and **Eq. 3.5**. The calculated geometric mean of T_2 distribution of interconnected pore space is used as an input parameter to the SDR model for permeability assessment.

In application of the Coates model (**Eq. 3.3**), I modified estimates of *FFI* and *BVI* by considering the isolated pore space. I also replaced the porosity in the Coates model by the calculated interconnected porosity, and calculated *FFI*/*BVI* index using the modified *FFI* and *BVI*. The T_2 cutoff for calculation of *FFI*/*BVI* in carbonate formations is approximately 100 msec (Straley et al. 1997).

3.2.5 Permeability Measurements

I first injected distilled water to the samples to completely remove the manganese-bearing solution. The rock samples were then dried in an oven at 150 °C for 3 hours. Next, I measured permeability of each rock sample using an unsteady-state gas permeameter under overburden pressure. The confining pressure for each measurement was set to 800 psi. The permeability corrected for Klinkenberg effect was later used for cross-validation of NMR-based permeability estimates.

3.3 Results

3.3.1 Bulk T_2 Relaxation Time of Manganese-Bearing Solution

First, I measured the bulk T_2 relaxation time of manganese-bearing solutions with different concentration of Mn^{2+} and carried out a sensitivity analysis on the concentration of Mn^{2+}. The solutions were contained in test tubes and scanned in GeoSpec2 NMR spectrometer. **Fig. 3.3** shows the measured bulk T_2 relaxation rate of manganese-bearing solutions with different concentrations. I observe that the relaxivity constant of manganese-bearing solution is 813.5 $g/L^{-1} \cdot sec^{-1}$, which is promising for a measurable influence of this contrast solution on NMR measurements.

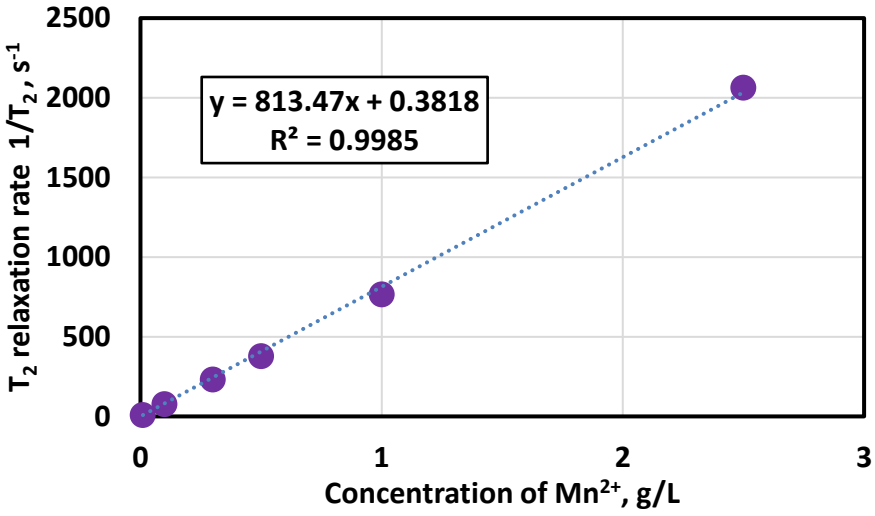

Fig. 3. 3 The experimentally measured linear relationship between NMR T_2 relaxation rate (1/ T_2) and concentration of manganese-bearing solution.

Fig. 3.4 shows the measured bulk T_2 relaxation times for the different manganese-bearing solutions. The measured bulk T_2 times for 0.01 g/L, 0.1 g/L, 0.3 g/L, 0.5 g/L, 1 g/L, 2.5 g/L, and 10 g/L manganese-bearing solutions are 126 msec, 14.1

msec, 5.01 msec, 2.82 msec, 1.41 msec, 0.631 msec, and 0.355 msec, respectively. I observe that the maximum T_2 time of 2.5 g/L and 10 g/L are 0.6 msec and 1.6 msec, respectively. The typical T_2 cutoff for clay-bound water is approximately 3 msec (Rylander et al. 2013). Therefore, to avoid the possible overlap of manganese T_2 distribution and clay-bound water T_2 distribution, I chose concentration of 10 g/L for the laboratory experiments.

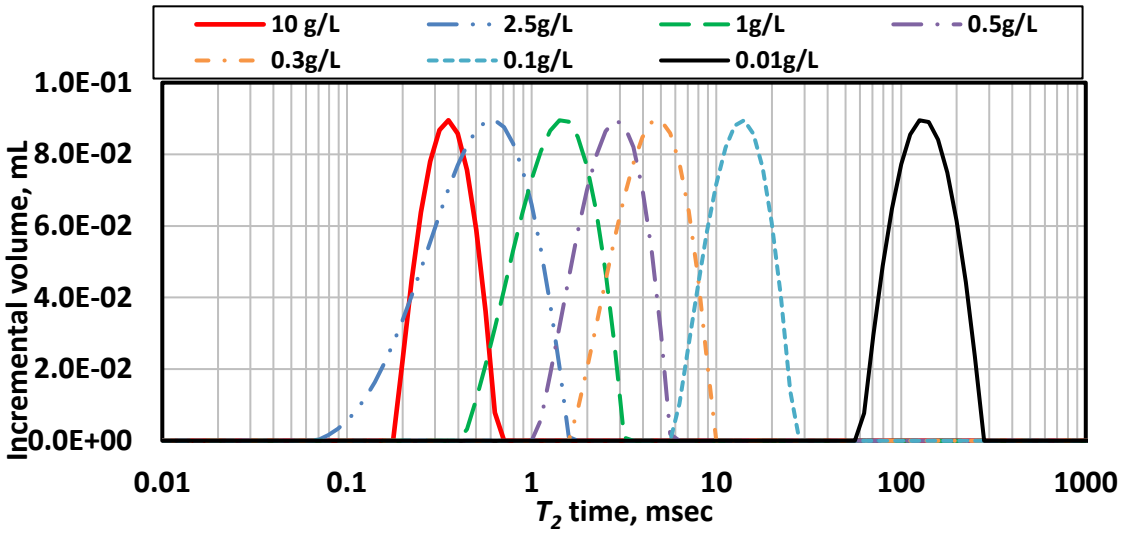

Fig. 3. 4 Bulk T_2 distribution measurements obtained for manganese-bearing solution at varying concentrations of manganese.

3.3.2 T_2 Distributions Before and After Manganese-Bearing Solution Injection

I conducted NMR T_2 measurements on the carbonate rock samples after saturating them with brine. Next, I coreflooded the rock sample with 10 g/L manganese-bearing solution and rescanned T_2 distribution using NMR spectrometer. **Figs. 3.5a**, **3.5b**, and **3.5c** show NMR T_2 distribution for the carbonate rock samples C1-1, C1-2, and C1-3, respectively, before and after injection of manganese-bearing solution.

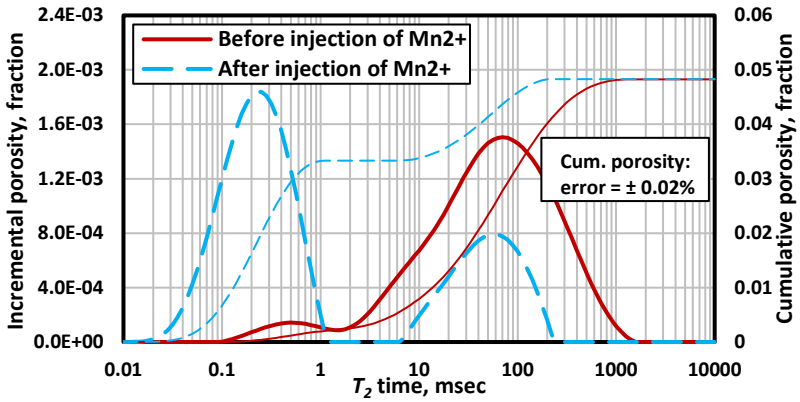

(a)

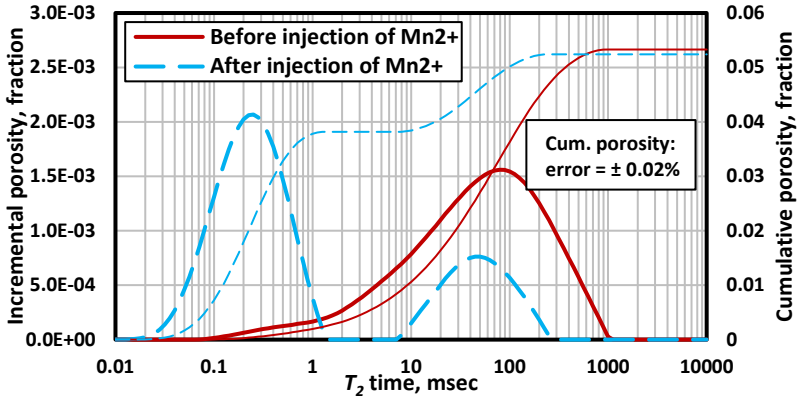

(b)

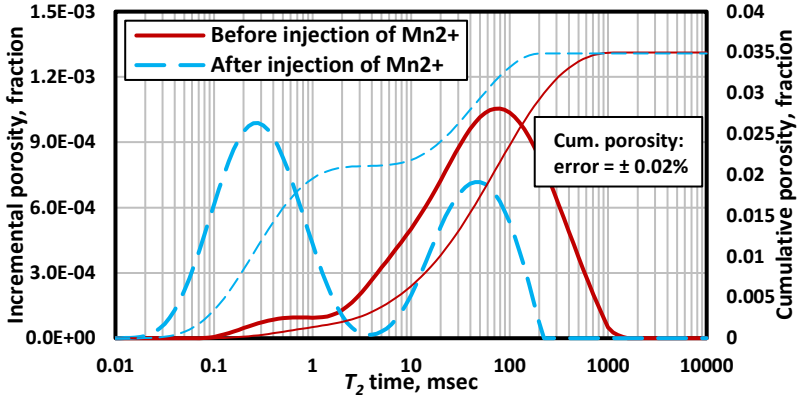

(c)

Fig. 3. 5 NMR T_2 distributions obtained before (red solid curve) and after (blue dashed curve) injection of manganese-bearing solution for carbonate rock samples (a) C1-1, (b) C1-2, and (c) C1-3.

Table 3.1 lists the total porosity, isolated porosity, interconnected porosity, and the ratio of isolated porosity to total porosity in rock samples C1-1, C1-2, and C1-3. These values are estimated using combined interpretation of NMR T_2 distributions before and after injection of the manganese-bearing solution. I observe that the cumulative volume of fluid in the rock before and after injection of manganese-bearing solution is almost the same, indicating that Mn^{2+} invasion in the rock does not affect the cumulative fluid volume obtained from NMR measurements.

Sample ID	Total Porosity, fraction	Isolated Porosity, fraction	Interconnected Porosity, fraction	Isolated Porosity/Total Porosity, %
C1-1	0.0483	0.0150	0.0333	31.1
C1-2	0.0533	0.0143	0.0390	26.8
C1-3	0.035	0.0137	0.0213	39.1

Table 3. 1 Carbonate Rock Type C1: The calculated total porosity, isolated porosity, interconnected porosity, and the ratio of isolated porosity to total porosity in carbonate rock samples C1-1, C1-2, and C1-3, using combined interpretation of NMR T_2 distributions before and after injection of the manganese-bearing solution.

I repeated the experiments for carbonate rock type C2. **Figs. 3.6a**, **3.6b**, **3.6c**, **3.6d**, and **3.6e** show NMR T_2 distribution in the carbonate rock samples C2-1, C2-2, C2-3, C2-4, and C2-5, respectively, before and after injection of manganese-bearing solution. The results before injection of the manganese-bearing solution reveal two T_2 relaxation peaks, located at approximately 70.8 msec and 1259 msec. Next, I conducted coreflood experiments using the manganese-bearing solution. The blue dashed curve shows NMR T_2 distribution after injection of the manganese-bearing solution. The T_2 peak located between 10 msec and 1000 msec represents the isolated pores. I also

observed a minor (i.e., less than 2%) change in cumulative volume of fluid after manganese-bearing solution injection. This slight loss of cumulative volume of fluid after manganese-bearing solution injection for sample C2-1 can be due to water evaporation or loss during NMR measurements. **Table 3.2** lists the total porosity, isolated porosity, interconnected porosity, and the ratio of isolated porosity to total porosity in rock samples from rock type C2. The ratio of isolated porosity to total porosity in rock type C2 is less than that in rock type C1.

3.3.3 Permeability Assessment Using the SDR Model and the T_2 Distribution Corrected for Isolated Pores

I used the estimated interconnected porosity and corrected geometric mean of T_2 distribution for permeability assessment using the SDR model. I compared the results against those obtained from the SDR model before considering the isolated pores in T_2 distribution. **Table 3.3** summarizes the permeability estimates from the SDR model using the original T_2 distribution and the one corrected for isolated pores for rock types C1 (i.e., Rock samples C1-1, C1-2, and C1-3) and C2 (i.e., Rock samples C2-1, C2-2, C2-3, C2-4, and C2-5). The new method enables calculation of interconnected and isolated porosity which was not possible using the original T_2 distribution. The same table includes geometric mean of T_2 distribution of the total and interconnected pore space and the measured Klinkenberg corrected permeability of the rock samples using unsteady state gas permeameter. The constant a in the SDR model is assumed to be 100 and 0.075 for rock type C1 and C2, respectively.

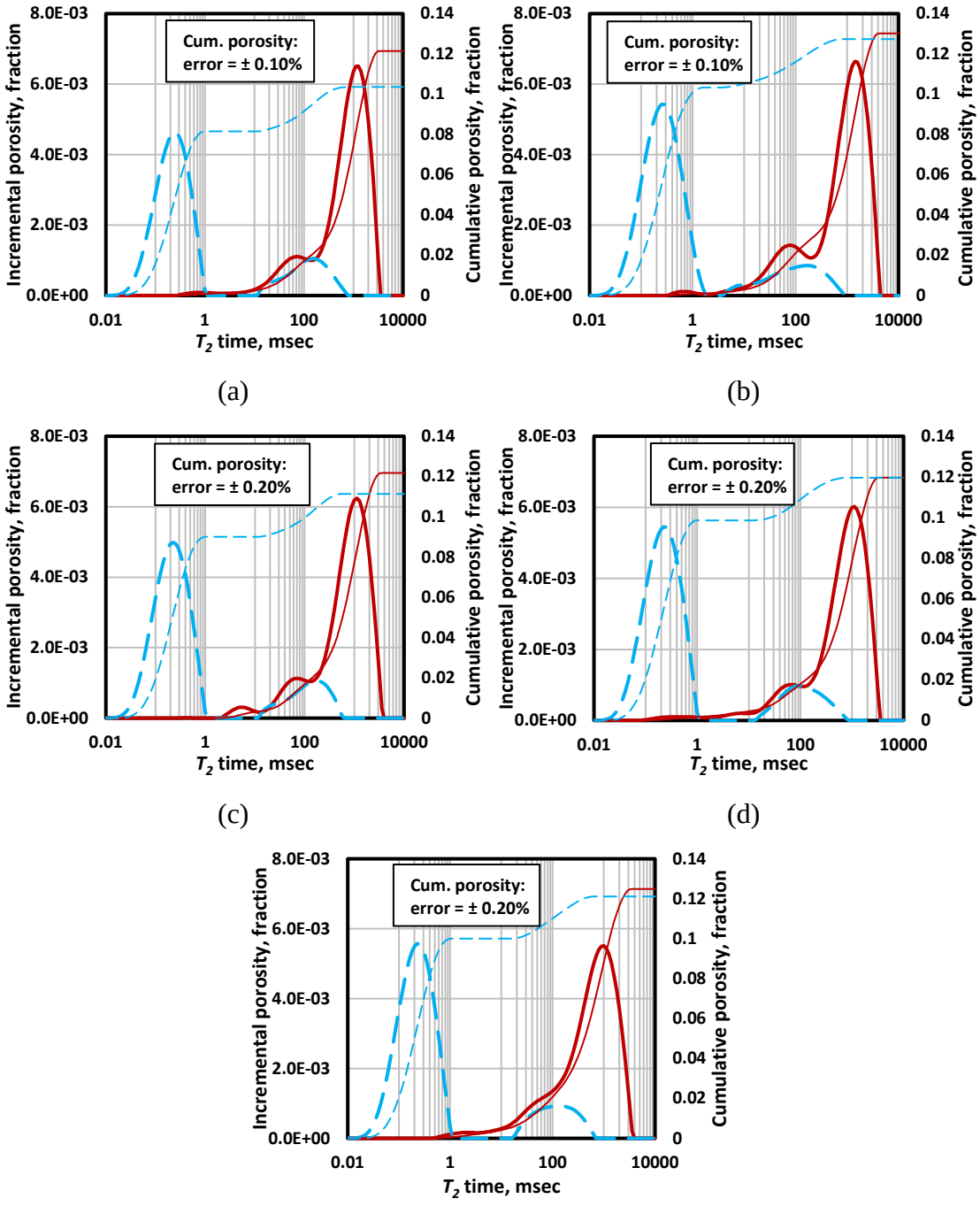

Fig. 3. 6 NMR T_2 distributions obtained before (red solid curve) and after (blue dashed curve) injection of manganese-bearing solution for carbonate rock samples (a) C2-1, (b) C2-2, (c) C2-3, (d) C2-4, and (e) C2-5.

Sample ID	Total Porosity, fraction	Isolated Porosity, fraction	Interconnected Porosity, fraction	Isolated Porosity/Total Porosity, %
C2-1	0.121	0.022	0.099	18.2
C2-2	0.130	0.023	0.107	17.7
C2-3	0.122	0.022	0.100	18.0
C2-4	0.120	0.021	0.099	17.5
C2-5	0.125	0.021	0.104	16.8

Table 3. 2 Carbonate Rock Type C2: The calculated total porosity, isolated porosity, interconnected porosity, and the ratio of isolated porosity to total porosity using combined interpretation of NMR T_2 distributions before and after injection of the manganese-bearing solution.

Sample ID	Original T_2 distribution			T_2 distribution corrected for isolated pores			Klinkenberg corrected permeability, mD
	Porosity, fraction	$T_{2gm,total}$, msec	SDR Permeability, mD	Porosity, fraction	$T_{2gm,inter}$, msec	SDR Permeability, mD	
C1-1	0.0483	45.69	1.14	0.0333	45.23	0.252	0.257
C1-2	0.0533	40.47	1.32	0.0390	38.48	0.343	0.353
C1-3	0.0350	42.87	0.276	0.0213	44.21	0.0402	0.017
C2-1	0.121	535.6	4.673	0.099	761.2	4.242	4.247
C2-2	0.130	579.8	7.245	0.107	894.9	7.814	7.640
C2-3	0.122	528.4	4.593	0.100	785.3	4.699	6.031
C2-4	0.120	461.2	3.265	0.099	666.9	3.152	3.276
C2-5	0.125	411.2	3.086	0.104	636.8	3.517	3.870

Table 3. 3 Comparison of the NMR-based permeability estimates from the SDR model using the original T_2 distribution and the one corrected for isolated pores in rock types C1 and C2 against the Klinkenberg corrected permeability measurements.

Fig. 3.7 compares the predicted permeability values from the SDR model using the original T_2 distribution and the one corrected for isolated pores against the measured Klinkenberg corrected permeability values for both rock types C1 and C2. In the case of rock type C1, I observed 500% error in NMR-based estimates of permeability compared to the Klinkenberg corrected permeability measurements, when the impact of isolated pores on T_2 distribution is not taken into account. However, in the case where the

interconnected porosity and the geometric mean T_2 of interconnected pore space is used for permeability estimation, the relative error in the NMR-based estimates of permeability is less than 10%, compared to the Klinkenberg corrected permeability. In the case of rock type C2, the average of relative errors in estimates of permeability improved from 11.9% to 6.6 % when the interconnected porosity and the corrected geometry mean of T_2 distribution are used for permeability assessment. The improvement in permeability estimates is more significant in rock type C1 compared to rock type C2. Because the ratio of isolated pore volume to total pore volume in rock type C1 is higher than that in rock type C2 (Tables 1 and 2).

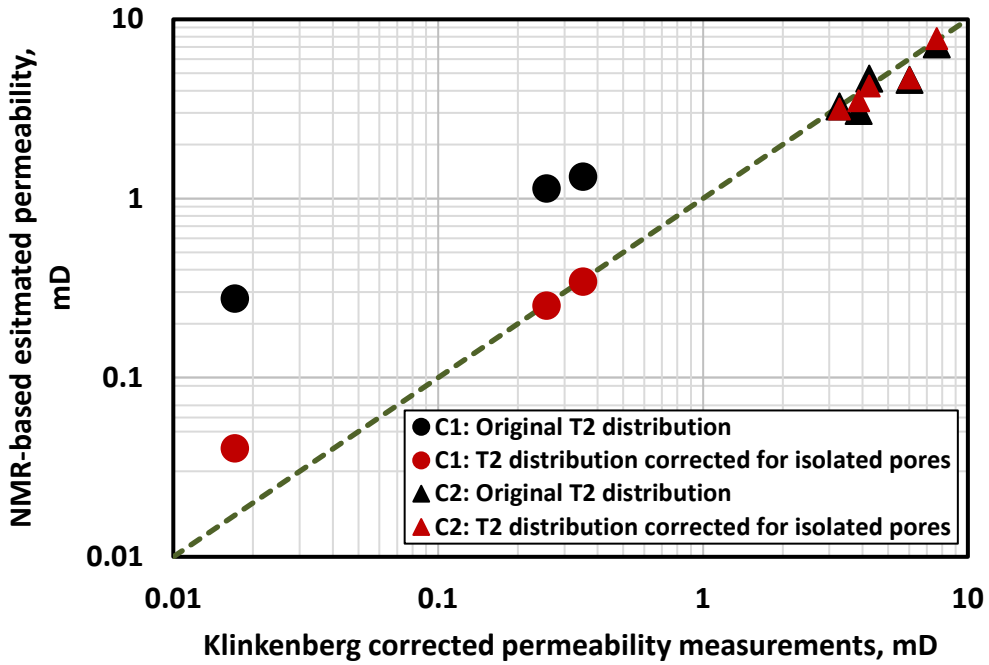

Fig. 3. 7 Comparison of the SDR permeability using the original T_2 distribution (black dots) and the one corrected for isolated pores (red dots) against the Klinkenberg corrected permeability measurements for carbonate rock types C1 (circle) and C2 (triangle).

3.3.4 Permeability Assessment Using the Coates Model and the T_2 Distribution Corrected for Isolated Pores

I also used the interconnected porosity and modified *FFI*/*BVI* index for permeability assessment using the Coates model. The results are then compared against those obtained from the Coates model before eliminating the influence of the isolated pores from T_2 distribution. **Table 3.4** summarizes the permeability estimates from the Coates model before and after correcting T_2 distribution for the impact of isolated pores in both rock types C1 and C2. Table 4 includes interconnected porosity using the proposed method, the modified *FFI*/*BVI* index and the measured permeability of the rock samples using unsteady-state gas permeameter. The constant C in the Coates model is assumed to be 0.040 and 0.224 for rock types C1 and C2, respectively.

Sample ID	Original T_2 distribution			T_2 distribution corrected for isolated pores			Klinkenberg corrected permeability, mD
	Porosity, fraction	*FFI/BVI*, msec	Coates Permeability, mD	Porosity, fraction	*Modified FFI/BVI*, msec	SDR Permeability, mD	
C1-1	0.0483	0.203	0.470	0.0333	45.23	0.266	0.257
C1-2	0.0533	0.192	0.623	0.0390	38.48	0.369	0.353
C1-3	0.0350	0.197	0.122	0.0213	44.06	0.0597	0.017
C2-1	0.121	6.103	3.236	0.099	10.95	4.680	4.247
C2-2	0.130	5.199	3.107	0.107	11.88	7.343	7.640
C2-3	0.122	6.198	3.370	0.100	12.91	6.779	6.031
C2-4	0.120	5.648	2.611	0.099	10.83	4.438	3.276
C2-5	0.125	5.053	2.486	0.104	8.830	3.603	3.870

Table 3. 4 Comparison of the NMR-based permeability estimates from the Coates model using the original T_2 distribution and the one corrected for isolated pores for rock types C1 and C2 against the Klinkenberg corrected permeability measurements.

Fig. 3.8 compares the estimated permeability values from the Coates model using the original T_2 distribution and the one corrected for isolated pores against the measured

permeability corrected for Klinkenberg effect. I also observed an average of 4.01% and 13.3% relative error (compared to the Klinkenberg corrected permeability) in estimates of permeability in rock types C1 and C2, respectively, using the interconnected porosity and the modified *FFI*/*BVI* index. This error increases to 79.7% and 36.3%, respectively, when the total porosity and original *FFI*/*BVI* index is used for permeability assessment.

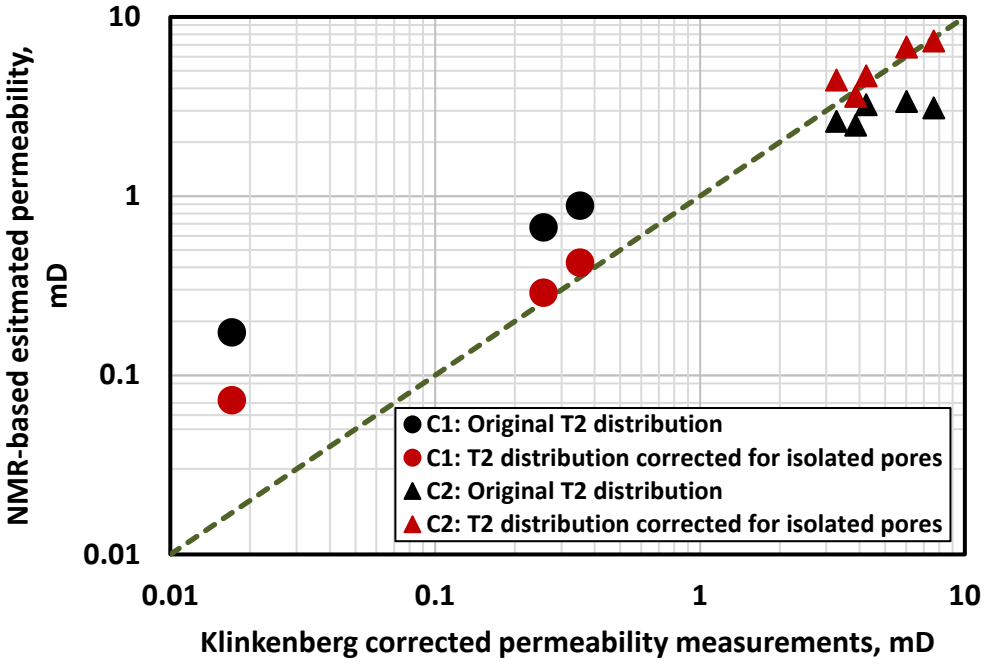

Fig. 3. 8 Comparison of the Coates permeability using the original T_2 distribution (black dots) and the one corrected for isolated pores (red dots) against the Klinkenberg corrected permeability measurements for carbonate rock types C1 (circle) and C2 (triangle).

3.4 Conclusions

I introduced a new method for assessment of permeability using NMR log-inject-log method and contrast manganese-bearing solution. I successfully applied the method to carbonate rock samples with complex pore geometry, where the isolated and

interconnected pores could not be distinguished using NMR measurements before injection of the contrast solution. The optimum concentration of Mn2+ in the contrast solution was estimated to be 10g/L via a sensitivity analysis. This concentration can, however, vary for different rock types with different pore size distribution.

The experimental results showed that the paramagnetic ions cause a decay in water signals, which enabled quantifying the connectivity of the pore network. The NMR T_2 peaks corresponding to the connected pore network were significantly shifted after injection of manganese-bearing solution, while, the T_2 peaks from the isolated pore network remained at the original location. Quantifying the interconnected and isolated pore volume significantly improved permeability estimates. After correcting T_2 distribution for the impact of isolated pores, the relative errors in NMR-based permeability estimates (compared to the permeability corrected for Klinkenberg effect) decreased from 500% to less than 10% using the SDR model and from 79.7% to 4.01% using the Coates model in one of the carbonate rock types. The improvement in permeability assessment was more significant in the rock type with larger ratio of isolated porosity to total porosity. For the rocks without isolated pore, the method would retrogress to the existing models (i.e. Coates and SDR models).

The successful application of the introduced method to carbonate core samples in the laboratory are promising for successful application of the introduced method for improved and real-time NMR-based permeability assessment in formations with complex pore structure. I propose injecting manganese-bearing solution in the formation at the desired depth intervals and applying NMR logging before and after injection of the

contrast solution. This method won't create any damage in the formations and the manganese-bearing solution is compatible with formation fluids. The feasibility of this technique for field application has been confirmed by the field examples of the existing NMR log-inject-log method. Compared against mercury injection capillary pressure (MICP) method, which is limited to few core samples and is not widely available, the method can be applied at any desired depth in the formations. This method is particularly recommended for formations with complex pore structure such as carbonates where conventional techniques cannot distinguish interconnected and isolated pore space.

CHAPTER IV

COMBINED INTERPRETATION OF NMR AND TGA MEASUREMENTS TO QUANTIFY THE IMPACT OF RELATIVE HUMIDITY ON HYDRATION OF CLAY MINERALS∗

Reliability of core measurement and analysis can be highly dependent on the humidity of measurement environment. However, impact of humidity on core measurements is often assumed to be negligible. I quantified the influence of relative humidity on the hydration of clay minerals (i.e., montmorillonite, illite, chlorite, and kaolinite) using nuclear magnetic resonance (NMR) and thermogravimetric analysis (TGA). The influence of clay hydration on the assessment of fluid volume in organic-rich mudrocks was also investigated. The NMR T_2 (spin-spin relaxation) magnetic decay of the clay samples showed existence of water even after the samples were dried in an oven at 95 °C. The TGA measurements in clay minerals confirmed the weight loss between 95°C and dehydroxylation temperature, which is approximately the same volume as that recorded by NMR measurement in dried samples. This recorded water volume corresponded to desorption of water molecules bound to interlayer cations (i.e., interlayer water). In the case of the hydration water, the NMR-based water vapor adsorption experiments showed that the volume of water accumulated on the surface of

---

∗ Reprinted with the permission from "Combined interpretation of NMR and TGA measurements to quantify the impact of relative humidity on hydration of clay minerals" by Kai Cheng and Zoya Heidari, 2017, *Applied Clay Science*, Copyright 2017 by Elsevier whose permission is required for further use.

clay minerals increased significantly as the relative humidity increased. The cation exchange capacity (CEC) measurements of clay minerals demonstrated that the volume of hydration water was strongly related to the CEC. The volume of interlayer water was, however, not related to the CEC. In the case of organic-rich mudrocks, water vapor adsorption experiments showed more than 250% change in water volume when relative humidity varies in the range of 0% to 95%, which further verified the significant impact of humidity on core measurements and the necessity of applying corrections for such an impact.

4.1. Introduction

Core analysis is an important approach in petrophysical evaluation of organic-rich mudrocks, because of significant uncertainties in well-log interpretation methods (Shafer, 2013). However, due to the complex composition and pore structure in these rocks, interpretation of core measurements is also challenging. Furthermore, laboratory environmental conditions, such as temperature, pressure, humidity, and oxygen level, can potentially impact the core samples and the corresponding core measurements (Unalmiser et al., 1998). These environmental effects can increase uncertainty in core analysis results. Therefore, quantifying the impact of environmental effects such as humidity is a required step towards improved core measurements, analysis, and evaluation. The impact of relative humidity on evaluation of water content in the

laboratory condition has not been well quantified, which can cause significant errors in the outcomes of core analysis.

Clay minerals are abundant in mudrocks and are considered to be highly sensitive to the environmental conditions. For instance, previous researches had shown that the humidity affects the hydration of montmorillonite (Cases et al., 1992, 1997; Berend et al., 1995). Cases et al. (1992, 1997) studied the structural changes that occurred during the intracryatalline swelling of a Wyoming sodium montmorillonite under controlled relative water vapor pressures. Xu et al. (2000) used environmental infrared microbalance to investigate water adsorption on montmorillonite and found that water adsorbed on the clay surface at low-water content was strongly influenced by the exchangeable cation and by the close proximity to the clay surface area. Chitale et al. (2000) reported 30-50 monolayers of water adsorbed on the surface of different types of clay minerals. Salles et al. (2008) studied the mesoscopic swelling of solid Na-montmorillonite at variable relative humidity and brought novel information about the swelling mechanisms. The hydration of clay minerals had significant influence on laboratory measurements for water saturation, especially in rock samples with high concentrations of clay minerals (Bush et al., 1970; Mooney et al., 1952). Even though the influence of humidity on the hydration of clay minerals has been discussed in previous publications, the impact of humidity on core analysis and measurements for assessment of water content in porous media has not been quantified.

The water in clay minerals in the laboratory condition includes hydration water and interlayer water (Grim 1962, Cases et al., 1992, Salles et al., 2008). Hydration water

refers to adsorbed water, which accumulates on the external surface of clay minerals (Barshad 1955). The interlayer water is strongly associated with interlayer cations and exists within the interlayer space (Salles et al., 2008). To better understand hydration of clay minerals, it is necessary to quantitatively and qualitatively evaluate hydration water and interlayer water.

NMR T_2 (spin-spin relaxation) measurements are highly sensitive to the presence of fluids in porous media and have been widely used for assessment of fluid distributions and mobility in porous media (Coates et al, 1999; Cheng et al., 2015). Another experimental approach for fluid characterization in porous media is thermogravimetric analysis (TGA). TGA measures the changes of material mass as a function of increasing temperature, which provides information about dehydration, desorption, and dehydroxylation (Doyle 1961; Handwerger et al., 2012). TGA also provides an approach to quantify the volume of fluids extracted at different temperatures and to classify different forms of fluids. Therefore, the combination of NMR and TGA measurements can potentially quantify the impact of humidity on hydration of clay minerals.

The objectives of this research are (a) to quantify the influence of relative humidity on hydration of clay minerals based on NMR and TGA methods and (b) to evaluate the impact of clay hydration on core-based petrophysical evaluation in organic-rich mudrocks. To achieve these objectives, a set of experiments was designed to examine the water content of pure clay minerals under different humidity levels and to investigate the forms of water existing on the surface of clay mineral. The following sections describe the method and the results obtained from the laboratory experiments.

4.2 Method

The impact of relative humidity on the hydration of clay minerals was investigated using laboratory NMR measurements and the interlayer water was assessed using combined NMR and TGA measurements. The saturated salt solutions were maintained in closed chambers to control relative humidity and to investigate water vapor adsorption on the surface of the clay minerals. The surface areas of clay samples were measured through analysis of nitrogen adsorption-desorption isotherms. CEC measurements on clay minerals were based on conductometric titration (Chapman, 1965). The investigation to the influence of hydration on assessment of fluid volumes in organic-rich mudrocks was conducted based on NMR measurements.

4.2.1 Preparation of Clay Minerals and Powdered Rock Samples

Five types of clay minerals used in the experiments included Na-montmorillonite, Ca-montmorillonite, illite, chlorite, and kaolinite. The Na-montmorillonite sample was from Crook County, Wyoming, USA; the Ca-montmorillonite sample was from Gonzales County, Texas, USA; the illite sample was from Silver Hill Montana, USA; the chlorite sample was from Flagstaff Hill El Dorado County, California, USA; and the kaolinite sample was from Warren County, Georgia, USA. They were all purchased from The Clay Minerals Society. The clay mineral samples were dried in an oven at 95ºC for more than 24 hours before starting the measurements. This condition was considered as initial state for the clay minerals.

Additionally, two organic-rich mudrock samples A and B were part of the experiment. Sample A was from subsurface cores and sample B was from an outcrop. The rock samples were crushed into a powder with particle size of less than 88 microns.

4.2.2 Relative Humidity Control and Water Vapor Adsorption Experiments

Seven vacuum chambers with pure water, saturated solutions of lithium chloride (LiCl), manganese chloride ($MnCl_2$), potassium carbonate (K_2CO_3), manganese nitrate ($Mn(NO_3)_2$), sodium chloride (NaCl), and potassium chloride (KCl) were kept at 25ºC for more than 24 hours to reach quasi-equilibrium. This procedure provided 11.3%, 32.8%, 43.1%, 53.9%, 75.3%, 84.3%, and 95.0% of relative humidity levels, respectively (Stokes et al., 1949; Young 1967).

The water vapor adsorption experiments were conducted under controlled relative humidity. Approximately 10g of each clay mineral was kept on a glass plate and maintained under various relative humidity levels for 5 days to reach quasi-equilibrium. The clay mineral samples were then weighed and collected in test tubes for NMR measurements. The same procedure was applied to the organic-rich mudrock samples at humidity level of 95% (the only humidity level tested in the case of mudrock samples).

4.2.3 NMR Measurements

A 2 MHz benchtop NMR spectrometer was used for the NMR laboratory measurements. The NMR T_2 relaxation measurements were carried out using a CPMG (Carr-Purcell-Meiboom-Gill) pulse sequence (Carr and Purcell, 1954; Meiboom and

Gill, 1958). I set the inter-echo spacing time (TE) of the CPMG pulse sequence to 100 μsec. The signal-to-noise ratios (SNR) of the measurements were more than 100. The fluid volumes estimated from NMR measurements were all normalized to mL per 100g mass of sample.

4.2.4 Thermogravimetric Analysis (TGA) of Clay Minerals

The TGA of clay samples was performed using a TGA Q500 equipment. The samples were maintained at room temperature for 30 minutes using helium as the purge gas, then heated to 1000°C at 5°C per minute heating rate, and maintained at 1000°C for another 30 minutes. In the case of montmorillonite, the temperature variation between dehydration and desorption of interlayer water was difficult to capture. Thus, a different procedure for TGA experiments was performed on Na-montmorillonite and Ca-montmorillonite. A three-stage TGA experiment was applied for Na-montmorillonite as illustrated by the red solid line in **Fig. 4.1**. Two intermediate temperatures (i.e., 400ºC and 500ºC) were chosen to check the dehydroxylation temperature of montmorillonite. These two temperatures were chosen based on previous publications, indicating that dehydroxylation temperature of montmorillonite is 500ºC (Cases et al., 1992). The Na-montmorillonite was firstly maintained at room temperature for 30 minutes under helium gas, then heated to 95°C at heating rate of 5°C per minute and maintained at 95°C for 1 hour, then heated to 400°C at the rated of 5°C per minute and maintained at 400°C for another 1 hour, then heated to 500°C at the same heating rated and maintained at 500°C for another 1 hour, finally heated to 1000°C at the same heating rated and maintained at

1000°C for 30 minutes. Since the temperature of dehydroxylation was determined from Na-montmorillonite TGA experiments, a one-stage TGA for Ca-montmorillonite was conducted as illustrated by the dashed line in Fig. 1. The Ca-montmorillonite sample was firstly maintained at room temperature for 1 hour under helium gas, then heated to 95°C at heating rate of 5°C per minute and maintained at 95°C for 1 hour, and then heated to 1000°C at the rated of 5°C per minute and maintained at 1000°C for another 30 minutes.

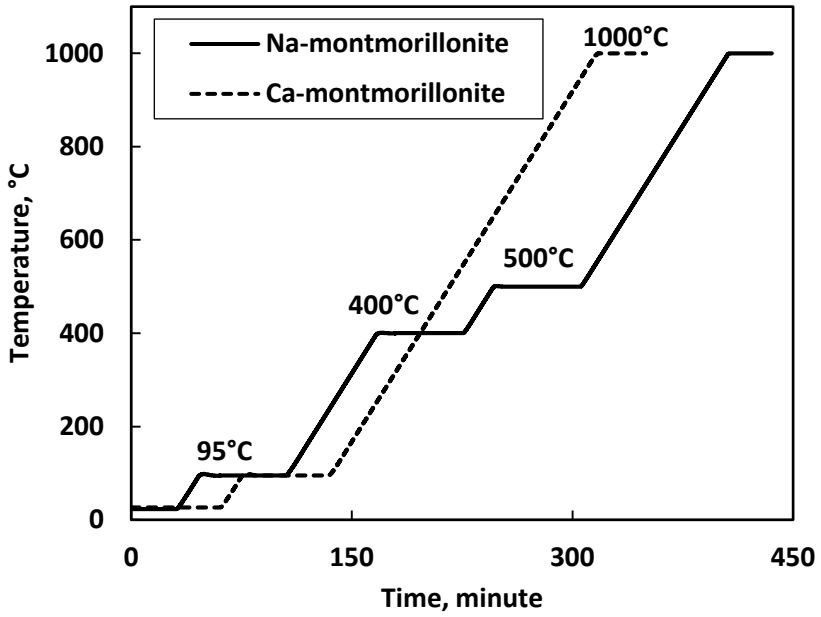

Fig. 4. 1 The temperature steps for evaluation of Na-montmorillonite and Ca-montmorillonite during TGA experiments.

4.2.5 Nitrogen Adsorption-Desorption Isotherm and Surface Area Assessment

Micromeritics 3flex equipment was used for nitrogen adsorption-desorption experiments at the temperature of 77K. It provided the Brunauer–Emmett–Teller (BET)

surface area of clay minerals. The samples were degassed using nitrogen at 150°C as the purge gas at the beginning of the test.

4.2.6 X-Ray Diffraction (XRD) of Organic-Rich Mudrocks

The clay-mineral composition of organic-rich mudrock samples was evaluated using XRD. The XRD measurements were performed with a Bruker D8 Discover with Vantec-500 2D detector. The source was copper K-alpha with tube voltage of 40 kV and 40 mA current.

4.2.7 CEC Measurements

Two grams of each clay mineral sample (Na-montmorillonite, Ca-montmorillonite, illite, chlorite, or kaolinite) was placed in 100 mL beaker. 25 mL of ammonium acetate at concentration of 1 mol/L was added to each beaker. The dispersion was stirred and kept overnight. Buchner funnel and vacuum pump were used to filter the dispersion. The clay mineral sample was leached 3 times with 15 mL increments of ammonium acetate. To remove excess ammonium acetate, the sample was also leached 3 times with ethanol. Then, the sample was transferred to 10 mL KCl solution at concentration of 1 mol/L. The dispersion was again stirred and kept overnight. The dispersion was then filtrated and leached 3 times with 5 mL portions of 1 mol/L KCl solution. The leachate was transferred to 250 mL volumetric flask and brought to volume using deionized water. The concentration of ammonium was analyzed using

ammonium-ion selective electrode. The CEC value of each clay mineral was calculated through

$$CEC = \frac{Concentration_{NH_4^+} \times Volume_{NH_4^+}}{Mass_{clay} \times m_{NH_4^+}}, \quad (4.1)$$

where $Concentration_{NH_4^+}$ is the concentration of leached ammonium ion solution, $Volume_{NH_4^+}$ is the volume of leached ammonium ion solution, $Mass_{clay}$ is the initial mass of clay mineral samples, and $m_{NH_4^+}$ is the molecular weight of ammonium ion.

4.2.8 NMR-Based Investigation of Hydration in Organic-Rich Mudrocks

The proposed method for estimation of clay hydration in organic-rich mudrocks is illustrated in **Fig. 4.2**. The first step included crushing organic-rich mudrock samples into a powder with particle size of less than 88 microns. Then, the powdered samples were dried in an oven at 95ºC for 24 hours and called as dry mudrock samples. The NMR measurements on the dry mudrock samples provided a magnetic decay expressed by

$$M(t)_{dry} = \sum_i M_i(0) e^{-\frac{t}{T_{2i}}}, \quad (4.2)$$

where $M(t)_{dry}$ is the magnitude of magnetization of dry sample at time t, $M_i(0)$ is initial magnetization from the i^{th} component of relaxation, and T_{2i} is the decay constant of the i^{th} component.

In the second step, the dry mudrock samples was put on a glass plate and maintained in a vacuum chamber at 95% relative humidity for 5 days. Those samples

were called wet mudrock samples. The NMR measurements on the wet samples then provided a second magnetic decay, given by

$$M(t)_{wet} = \sum M_i(0) e^{-\frac{t}{T_{2i}}} + M(t)_{hydration}, \quad (4.3)$$

where $M(t)_{wet}$ is the magnitude of magnetization of wet samples at time t and $M(t)_{hydration}$ is the magnitude of magnetization of hydration water at time t.

Finally, estimation of the magnetic decay of clay hydration was obtained by subtracting the magnetic decay of dry mudrock samples from that of wet mudrock samples via

$$M(t)_{hydration} = M(t)_{wet} - M(t)_{dry}. \quad (4.4)$$

NMR T_2 distribution of clay hydration was estimated through T_2 inversion of magnetization decay obtained from **Eq. 4.4**.

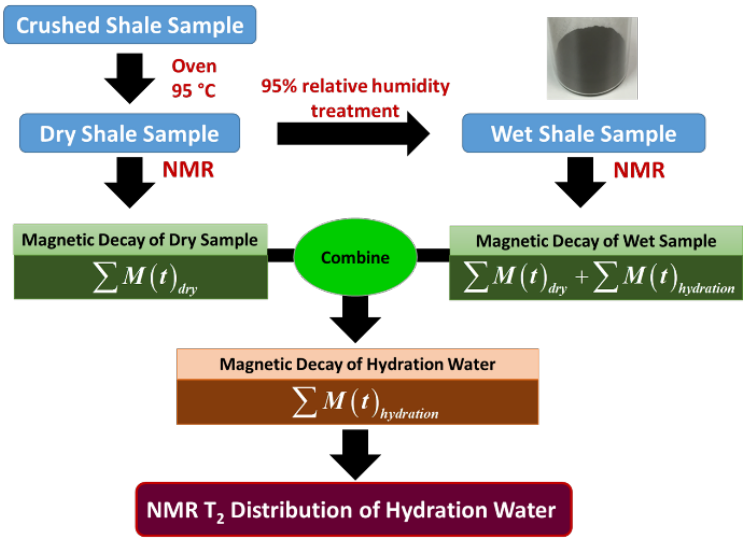

Fig. 4. 2 Workflow for assessment of clay hydration in organic-rich mudrocks.

4.3 Results and Discussion

4.3.1 Nitrogen Adsorption and Desorption Isotherms

The nitrogen adsorption and desorption isotherms of Na-montmorillonite (blue line) and Ca-montmorillonite (red line) at initial state are type-II isotherms (**Fig. 4.3**), with type H3 hysteresis loop (Sing et al., 1985), due to capillary condensation in multilayer adsorption. The shape of the hysteresis loop is usually relevant to aggregates of plate-like particles giving rise to slit-shaped pores and indicates a narrow size distribution of lamellar mesopores between different montmorillonite particles (Cases et al., 1992; Berend et al., 1995). The Ca-montmorillonite has higher nitrogen adsorption capacity than Na-montmorillonite as shown in the figure. The BET surface areas of Na-montmorillonite and Ca-montmorillonite were estimated to be 22.40 m^2/g and 91.62 m^2/g, respectively.

Similar to montmorillonite, the nitrogen adsorption and desorption isotherm of illite at initial state is also type-II with a hysteresis loop (Fig. **4.4**), indicating the existence of lamellar mesopores. The BET surface area of illite was estimated to be 20.89 m^2/g.

The nitrogen adsorption and desorption isotherm of chlorite (blue line) and kaolinite (red line) at initial state are type-II isotherms without a noticeable hysteresis loop (**Fig. 4.5**), indicating that the adsorption occurred at the surface of clay minerals. It is known as monolayer adsorption (Sing et al., 1985). The BET surface areas of chlorite and kaolinite were estimated to be 6.25 m^2/g and 8.23 m^2/g, respectively.

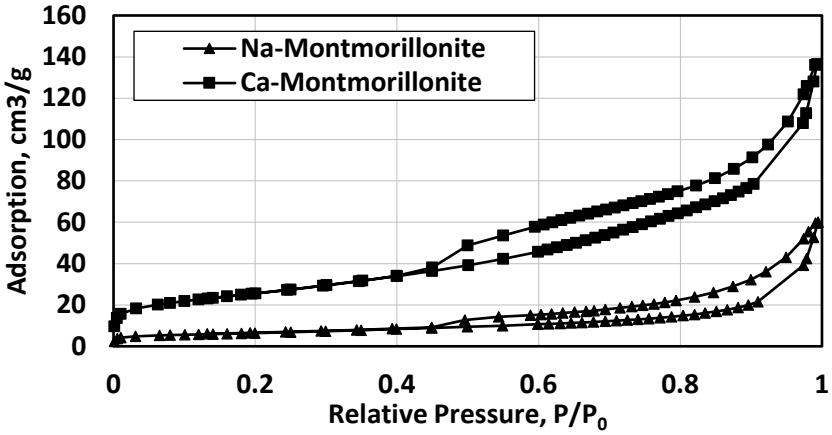

Fig. 4. 3 Nitrogen adsorption and desorption isotherm of Na-montmorillonite (triangle-dotted curve) and Ca-montmorillonite (square-dotted curve).

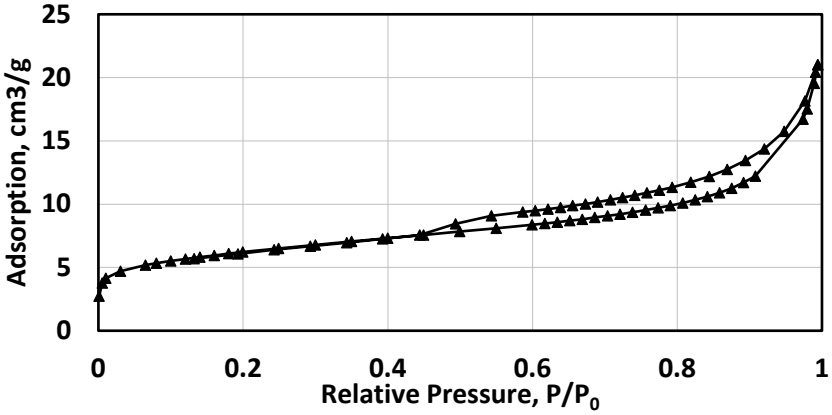

Fig. 4. 4 Nitrogen adsorption and desorption isotherm of illite.

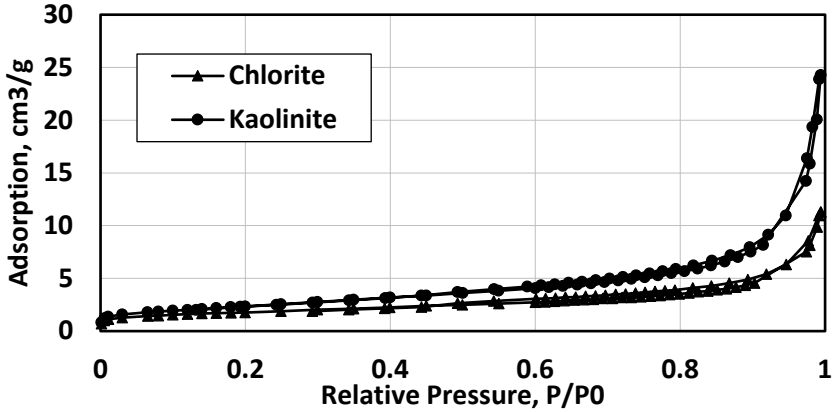

Fig. 4. 5 Nitrogen adsorption and desorption isotherm of chlorite (triangle-dotted curve) and kaolinite (circle-dotted curve).

4.3.2 Thermogravimetric Analysis (TGA)

The thermogravimetric analysis result for the Na-montmorillonite sample is shown in **Fig. 4.6a**. The TGA curve can be divided into three parts. The first part was a low-temperature region where a sharp decrease occurred at temperatures of less than 95ºC under helium gas. This region corresponded to the dehydration of Na-montmorillonite. The second part, the range of 95ºC to 500ºC, showed a total weight loss of 1.00 mass%. This region corresponded to desorption of water molecules which were directly bounded to interlayer space (i.e., interlayer water). The third part was a high-temperature region (i.e., above 500ºC), which showed the weight loss of approximately 4.99 mass%, representing dehydroxylation of the Na-montmorillonite (Cases et al., 1992). However, the distinction of desorption of interlayer water and dehydroxylation of Na-montmorillonite was not obvious.

To further investigate the range of temperature for desorption of interlayer water and dehydroxylation, a three-stage TGA for Na-montmorillonite was carried out as depicted in **Fig. 4.1**. TGA curve of Na-montmorillonite (blue line) and the derivative of weight change (black line) as a function of time are presented in **Fig. 4.6b**. Before heating the sample, a sharp decrease of mass occurred, due to dehydration of montmorillonite under helium gas condition (i.e., 0% relative humidity). During heating the sample to 95ºC, an initial fast decrease (high derivative weight change) of mass showed almost zero variation after the sample temperature reached 95ºC. After the sample was maintained at 95ºC for 1 hour, there was no variation in weight or an increase in derivative weight change. This observation indicated the completion of

dehydration of the Na-montmorillonite. When the sample was again heated to 400ºC, the weight of sample decreased and the derivative weight change increased slightly. After the sample was maintained at 400ºC for 1 hour, the weight loss became stable and the derivative weight change asymptoted to zero. The derivative weight change was approximately zero when the sample was maintained at 500ºC, but increased significantly when temperature increased to above 500ºC. This observation indicated that the dehydroxylation of Na-montmorillonite started at 500ºC. Therefore, the volume of interlayer water was estimated by calculating the weight change between 95ºC and 500ºC.

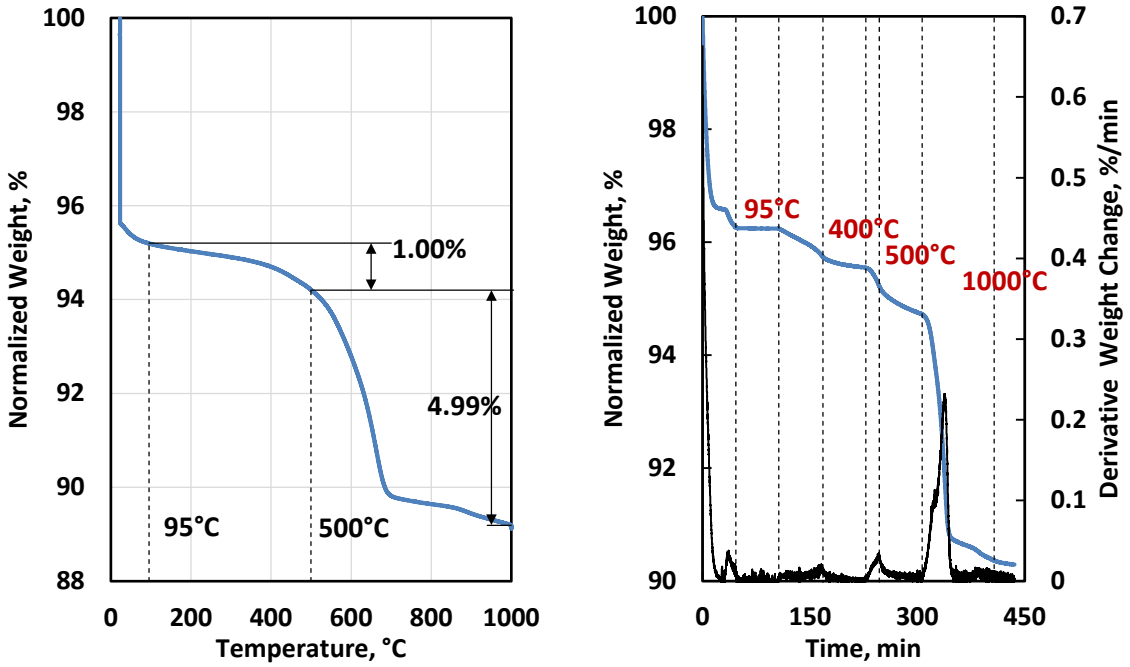

(a) (b)

Fig. 4. 6 (a) Thermogravimetric analysis of the Na-montmorillonite sample; (b) a three-stages thermogravimetric analysis of the Na-montmorillonite sample, which was maintained at 95ºC, 400ºC, and 500ºC for one hour.

Similarly, the thermogravimetric curve for the Ca-montmorillonite sample can be divided into three parts, including dehydration, desorption of interlayer water, and dehydroxylation (**Fig. 4.7a**). At the temperature of 125ºC, the change of slope indicated weight loss changes from dehydration to desorption of interlayer water. Assuming that desorption of interlayer water started at 125ºC, the weight percentage of interlayer water was estimated to be approximately 1.39 mass%. The weight loss of dehydroxylation was approximately 3.08 mass%.

To further determine the temperature for the completion of dehydration (95ºC or 125ºC), the sample was maintained at 95ºC for one hour during the process of TGA experiment. The single-stage TGA curve for Ca-montmorillonite after kept at 95ºC for one hour is shown in **Fig. 4.7b**. The black line showed the derivative of weight change as a function of time. Before heating the sample, a sharp decrease of mass occurred corresponding to dehydration. During heating the sample to 95ºC, a fast decrease of mass was observed, and didn't approach zero variation when temperature reached 95ºC. However, when the sample was maintained at 95ºC for 1 hour, the weight loss became stable and derivative weight change asymptoted to zero. The observation confirmed the completion of dehydration of Ca-montmorillonite at 95ºC. The weight change between 95ºC and 500ºC (as depicted in Fig. 8b) was 1.36 mass% weight loss, corresponding to interlayer water. This estimated weight loss agreed with that obtained from **Fig. 4.7a**. Therefore, temperature of 95ºC was high enough for dehydration of Ca-montmorillonite.

The thermogravimetric analysis for the illite sample showed a sharp decrease below 95ºC, corresponding to the dehydration of illite (**Fig. 4.8a**). The weight change

significantly increases at the temperatures above 400ºC, indicating the start of dehydroxylation of illite. Based on the assumption that the desorption of interlayer water started at 95ºC, the weight percentages of interlayer water and dehydroxylation water were calculated to be 1.08 mass% and 4.12 mass%, respectively.

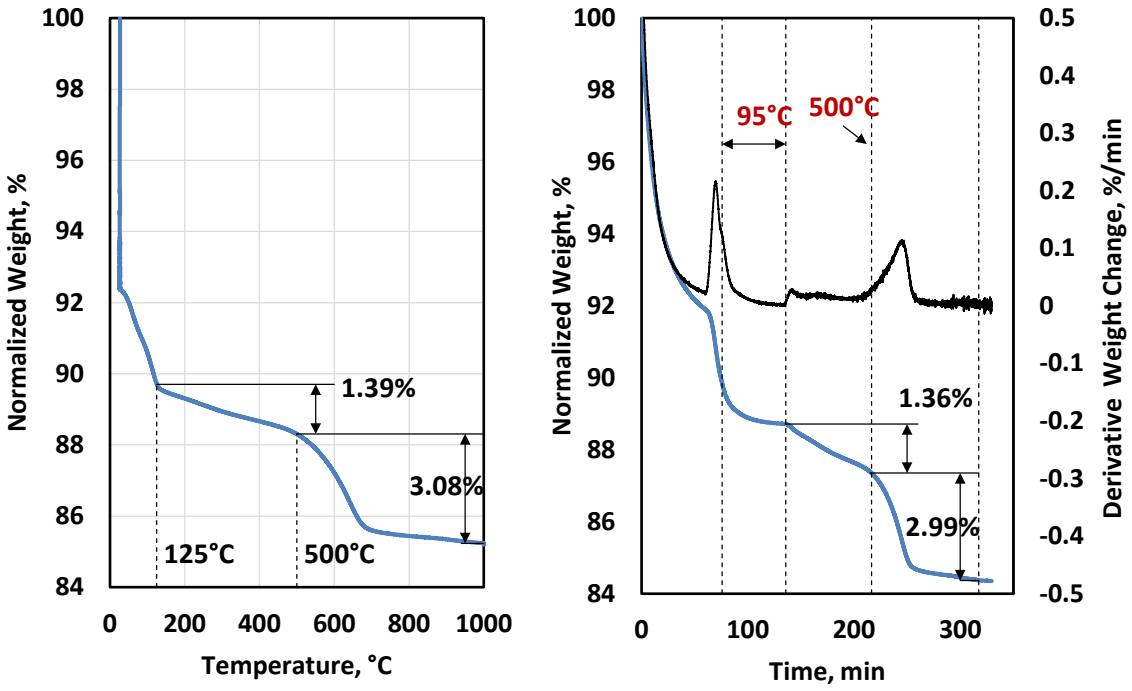

(a) (b)

Fig. 4. 7 (a) Thermogravimetric analysis of the Ca-montmorillonite sample; (b) a single-stage thermogravimetric analysis of the Ca-montmorillonite sample, which was maintained at 95ºC for one hour.

The TGA curve for the chlorite sample is shown in **Fig. 4.8b**. Before heating the sample to 95ºC, there was not much decrease of weight, indicating that dehydration of the chlorite sample was not significant. The dehydroxylation of chlorite was assumed to start at 535ºC. This assumption agreed with a previous publication which reported that the dehydroxylation of chlorite started at a temperature in the range of 500ºC to 600ºC

(Ross, 1968). Based on this assumption, the weight percentage of adsorbed water and dehydroxylation water was estimated to be approximately 1.77 mass% and 10.89 mass%, respectively.

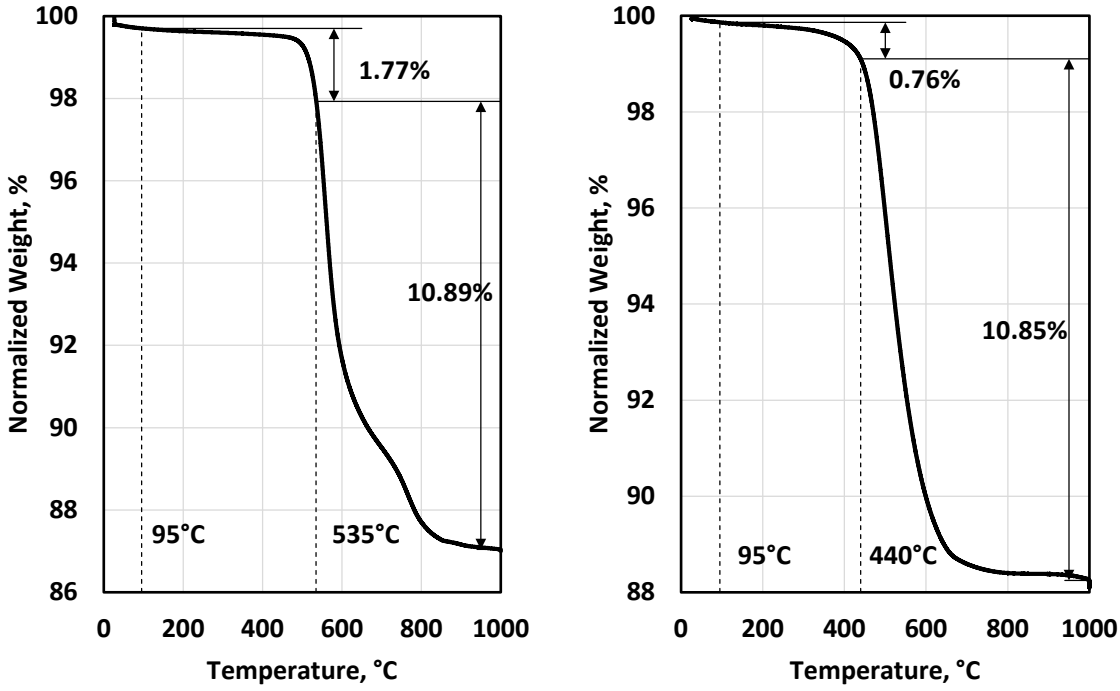

(a) (b)

Fig. 4. 8 Thermogravimetric analysis of (a) illite and (b) chlorite sample.

Similar to the case of chlorite, the dehydration of kaolinite was not significant based on TGA curve for the kaolinite sample (**Fig. 4.9**). The dehydroxylation of kaolinite occurred through the chemical reaction, given by

$$Al_4Si_4O_{10}(OH)_8 \rightarrow 2Al_2Si_2O_7 + 4H_2O. \quad (4.5)$$

The directly calculated molecular weight percent of water obtained after dehydroxylation was 13.95 mass% of total mass. The dehydroxylation of kaolinite was assumed to start at 440ºC. This assumption agrees with previous publications, which

documented that the dehydroxylation of kaolinite started in the temperature range of 430ºC to 450ºC (Toussaint et al., 1962; Sperinck et al., 2010). The weight loss was approximately 10.85 mass% in the temperature range of 440ºC to 1000ºC. The estimated value of dehydroxylation water agreed with molecular calculations. The weight loss was approximately 0.76 mass% in the temperature range of 95ºC to 440ºC.

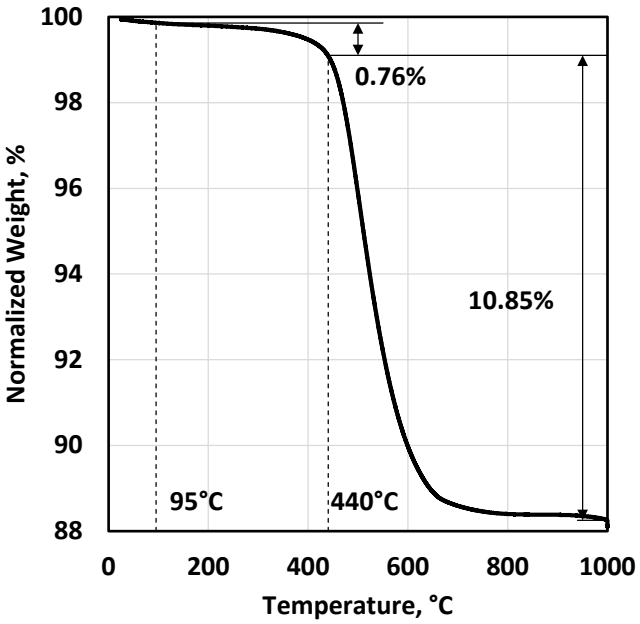

Fig. 4. 9 Thermogravimetric analysis of the kaolinite sample.

4.3.3 Water Vapor Adsorption Experiments and NMR Measurements

NMR T_2 distributions of Na-montmorillonite maintained under relative humidity of 0% (black solid line), 11.3% (blue solid line), 32.8% (green solid line), 43.1% (orange solid line), 53.9% (blue dashed line), 75.3% (green dashed line), 84.3% (orange dashed line), and 95.0% (red solid line) for 5 days are shown in **Fig. 4.10**. The total fluid volume increased when relative humidity increased. As confirmed by TGA results, the black solid line (i.e., T_2 peak located between 0.01msec to 0.2msec) represents the

interlayer water, which is the existing water in the Na-montmorillonite sample in the initial state. The volumetric concentration of interlayer water for Na-montmorillonite was 0.96 mL/100g (i.e., 0.96 mass%), based on NMR measurements. This estimate agreed with that estimated from TGA results (i.e., 1.00 mass%). With an increase in humidity level, there was a significant increase in water volume and shift of the T_2 peak to longer T_2 relaxation times. By subtracting the volume of interlayer water from total water volume, which was obtained at 95.0% relative humidity level, the volume of hydration water was calculated to be 18.9 mL/100g, which was one order of magnitude higher than the volume of interlayer water. The hydration water is normalized to mL/100g, representing the volume of water in 100 g of hydrated clay minerals. The results indicated that hydration of montmorillonite can have significant influence on assessment of water content in clay-rich formations under different humidity environment.

NMR T_2 distributions of Ca-montmorillonite were measured after the samples were maintained under eight different relative humidity levels for 5 days (**Fig. 4.11**). The black solid line of T_2 distribution represents the interlayer water, which locates between 0.01 msec to 0.2 msec. The volumetric concentration of interlayer water for Ca-montmorillonite was estimated to be 1.60 mL/100g (i.e., 1.60 mass%). This estimate was in agreement with that from TGA results (i.e., approximately 1.39 mass%). By subtracting the volume of interlayer water from total water volume, which was obtained at 95.0% relative humidity level, the volume of hydration water was calculated to be 24.50 mL/100g in Ca-montmorillonite.

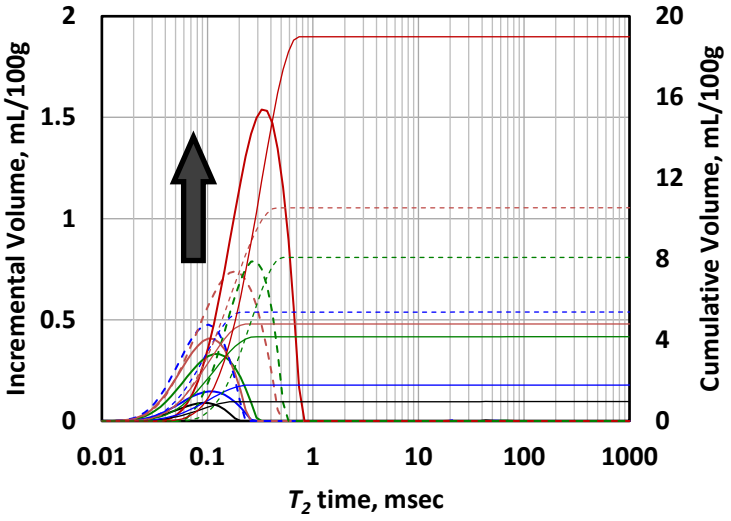

Fig. 4. 10 NMR T_2 distributions of Na-montmorillonite maintained under relative humidity levels of 0% (black solid line), 11.3% (blue solid line), 32.8% (green solid line), 43.1% (orange solid line), 53.9% (blue dashed line), 75.3% (green dashed line), 84.3% (orange dashed line), and 95.0% (red solid line).

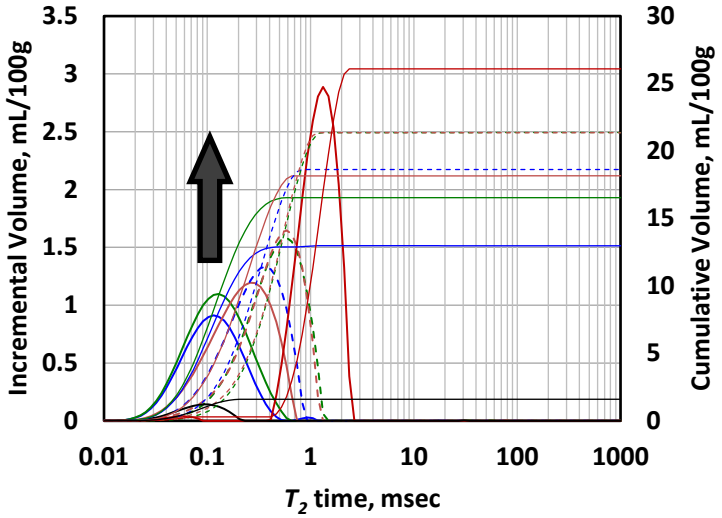

Fig. 4. 11 NMR T_2 distributions of Ca-montmorillonite maintained under relative humidity levels of 0% (black solid line), 11.3% (blue solid line), 32.8% (green solid line), 43.1% (orange solid line), 53.9% (blue dashed), 75.3% (green dashed), 84.3% (orange dashed), and 95.0% (red solid line).

NMR T_2 distributions of illite were also measured under eight different relative humidity levels for 5 days (**Fig. 4.12**). The black solid line represents the T_2 distribution

of interlayer water in illite. The volumetric concentration of interlayer water for illite was 0.86 mL/100g. The TGA results indicated the weight percentages of interlayer water to be approximately 1.08 mass%. The slight difference between NMR-based volume of water and TGA-based weight loss of water might be due to the small uncertainty in dehydroxylation temperature of illite. A shift of the T_2 peak to longer relation times occurred, as the humidity level increased. The maximum water volume was obtained at 95.0% relative humidity level. The volume of hydration water of illite was estimated to be 5.30 mL/100g, which was still five times higher than the volume of interlayer water.

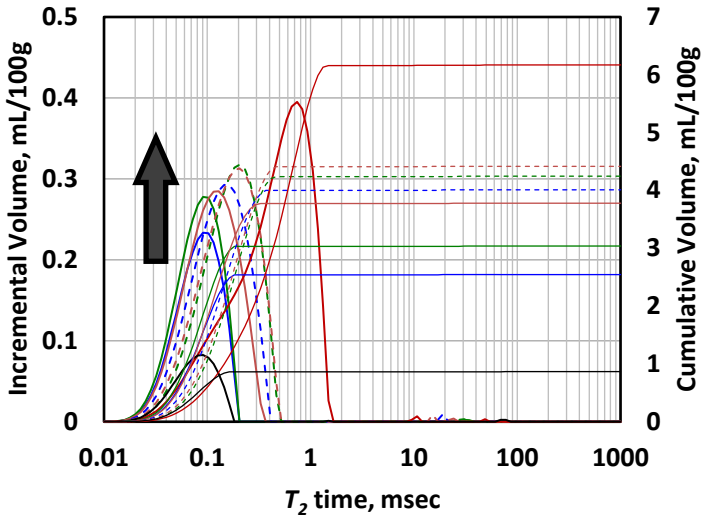

Fig. 4. 12 NMR T_2 distributions of illite maintained under relative humidity levels of 0% (black solid line), 11.3% (blue solid line), 32.8% (green solid line), 43.1% (orange solid line), 53.9% (blue dashed line), 75.3% (green dashed line), 84.3% (orange dashed line), and 95.0% (red solid line).

NMR T_2 distributions of chlorite, maintained under eight different relative humidity levels for 5 days, are shown in **Fig. 4.13**. The NMR T_2 distribution measurements, maintained under 0% relative humidity level, indicated that the volumetric concentration of adsorbed water at 0% relative humidity level (estimated

from black solid curve) for chlorite was 1.61 mL/100g (i.e., 1.61 mass%), which agreed with that from TGA results (i.e., approximately 1.77 mass%). The hydrated chlorite sample had a second T_2 peak which located in the range of 0.2 msec to 2 msec. The amplitude of the second T_2 peak increased as the relative humidity increased. This observation indicated that the second T_2 peak corresponded to the hydration of chlorite. The separation of T_2 peaks indicated that the hydration water didn't contact the adsorbed water and was mostly located at the outer surface of chlorite. The maximum water volume was obtained at 95.0% relative humidity level. The volume of hydration water in the case of chlorite was estimated to be 2.20 mL/100g.

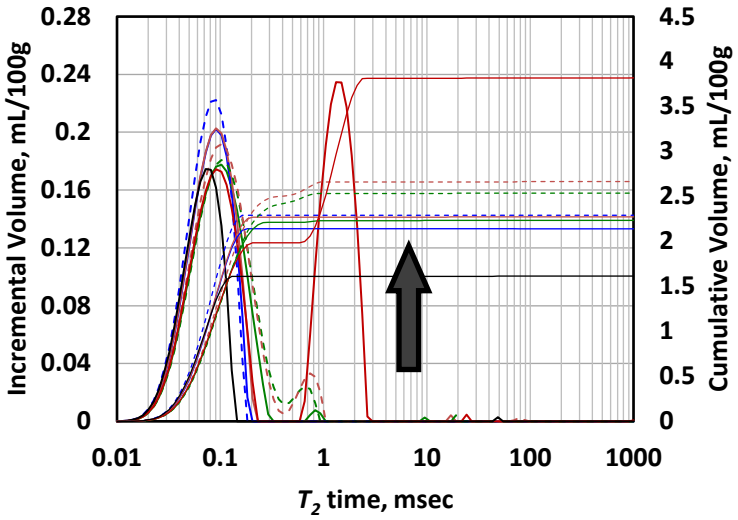

Fig. 4. 13 NMR T_2 distributions of chlorite maintained under relative humidity levels of 0% (black solid line), 11.3% (blue solid line), 32.8% (green solid line), 43.1% (orange solid line), 53.9% (blue dashed line), 75.3% (green dashed line), 84.3% (orange dashed line), and 95.0% (red solid line).

NMR T_2 distributions of kaolinite maintained under eight different relative humidity levels for 5 days are shown in **Fig. 4.14**. The black solid line of T_2 distribution

represents the adsorbed water at 0% relative humidity level. The volumetric concentration of adsorbed water for kaolinite was 0.77 mL/100g, which agreed with the results obtained from TGA (i.e., 0.76 mass%). The second T_2 peak located in the range of 0.2 msec to 2 msec. The amplitude of the second T_2 peak increased significantly, as a result of increase in relative humidity. This observation indicated that the hydration water didn't contact the adsorbed water and was mostly located at the outer surface of kaolinite. The maximum water volume was obtained at 95.0% relative humidity level. The volume of hydration water in the case of kaolinite was estimated to be 1.23 mL/100g.

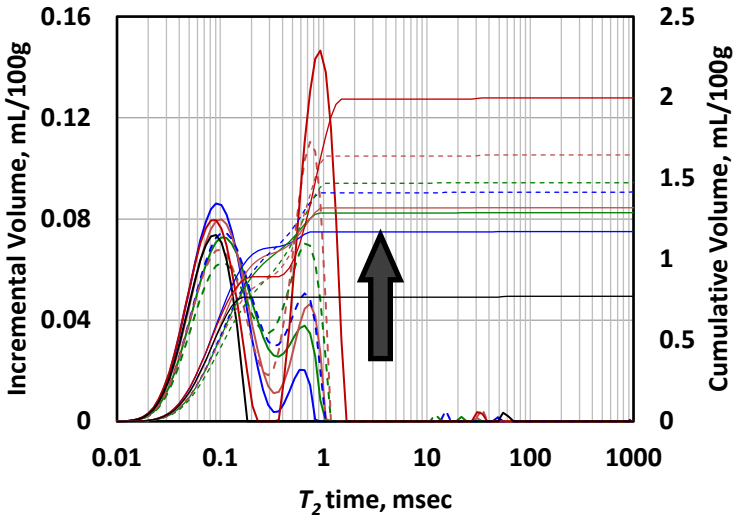

Fig. 4. 14 NMR T_2 distributions of kaolinite maintained under relative humidity of 0% (black solid line), 11.3% (blue solid line), 32.8% (green solid line), 43.1% (orange solid line), 53.9% (blue dashed line), 75.3% (green dashed line), 84.3% (orange dashed line), and 95.0% (red solid line).

The NMR measurement results at different relative humidity levels, confirmed that hydration of clay minerals intensively occurred at high humidity levels and had

significant influence on estimates of total fluid volume. The hydration of montmorillonite was much more significant than other types of clay minerals. In the case of montmorillonite and illite, the hydration of clay minerals caused the shift of T_2 peaks to longer relaxation times. However, in case of chlorite and kaolinite, the hydration resulted in the appearance of a second T_2 peak. Further investigations on structures of clay minerals are required to explain this difference.

4.3.4 CEC of Clay Minerals

The CEC measurements showed that the CEC of Na-montmorillonite, Ca-montmorillonite, illite, chlorite, kaolinite were 47.15 cmol/kg, 53.53 cmol/kg, 8.39 cmol/kg, 1.07 cmol/kg, and 1.70 cmol/kg, respectively. The volume of hydration water and interlayer water (or adsorbed water) were plotted as a function of the CEC of clay minerals (**Fig. 4.15**). The figure indicated that the volume of hydration water is strongly controlled by CEC of clay minerals. However, CEC of clay minerals did not significantly affect the volume of interlayer water.

4.3.5 Quantification of Hydration in Organic-Rich Mudrocks

NMR experiments on two powdered organic-rich mudrock samples were performed to quantify hydration in these samples in the presence of both clay and non-clay minerals as well as kerogen. **Table 4.1** summarizes weight concentrations of dominant minerals in these two samples, obtained from XRD analysis. Weight concentrations of clay minerals in mudrock samples A and B were 53.7% and 15.8%,

respectively. Dominant clay types in sample A were illite and montmorillonite. High concentration of kaolinite was observed in sample B.

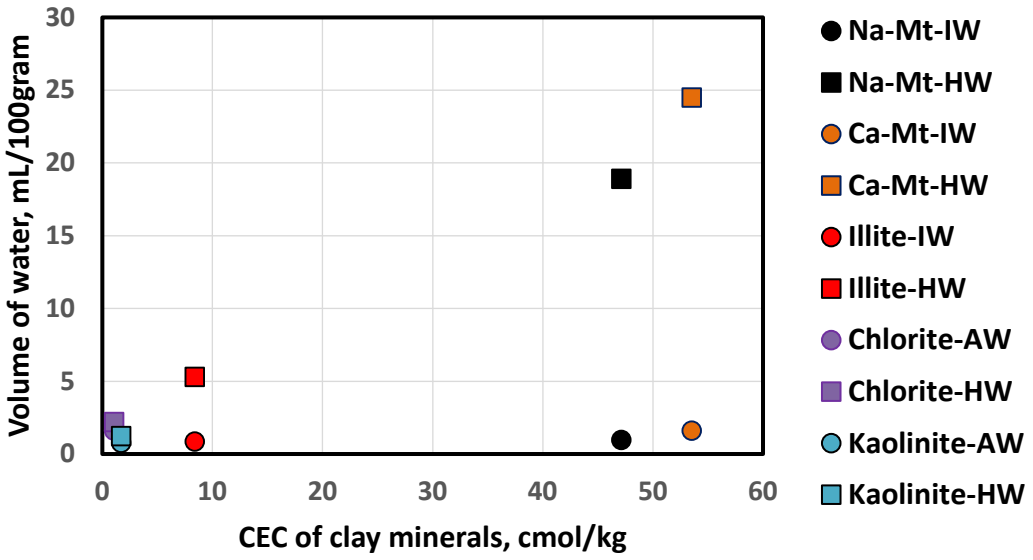

Fig. 4. 15 The experimentally measured correlation between volume of hydration water (HW) and CEC of Na-montmorillonite (Na-Mt), Ca-montmorillonite (Ca-Mt), illite, chlorite, and kaolinite, and correlation between the volume of interlayer water (IW) (or adsorbed water (AW)) and CEC of these clay minerals.

Composition	Sample A	Sample B
Quartz	20.0	22.5
Plagioclase	2.8	0.6
K-feldspars	3.3	0.0
Calcite	2.8	59.4
Dolomite	0.0	0.0
Montmorillonite	12.5	6.1
Illite	39.5	3.7
Chlorite	1.7	0.0
Kaolinite	0.0	6.0
Total clay minerals	53.7	15.8
Others	17.4	1.7

Table 4. 1 The weight concentrations of dominant minerals in organic-rich mudrock samples A and B, obtained from XRD analysis (mass%).

NMR T_2 distributions, measured in organic-rich mudrock samples A and B, are presented in **Fig. 4.16** and **Fig. 4.17**, respectively. Solid and dashed curves represent the NMR T_2 distributions before and after hydration, respectively. The dash-dotted line represents the hydration water in the samples. A significant increase in fluid volume was observed after the sample was maintained under 95% relative humidity. After hydration of mudrock sample A, the T_2 peak slightly shifted to the right and the area under T_2 distribution increased due to combination of T_2 distribution of initial-state mudrock sample and that of hydration water. The total volume of fluids in initial-state mudrock sample was 1.11 mL/100g. However, the volume of hydration water was approximately 2.78 mL/100g in mudrock sample A.

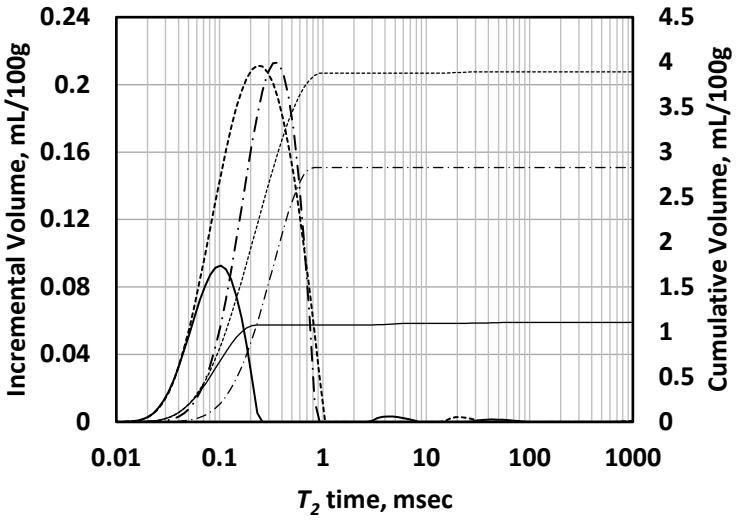

Fig. 4. 16 NMR T_2 distributions in mudrock sample A before (solid curve) and after hydration (dashed curve). The dash-dotted curve represents the calculated T_2 distributions for hydration water.

Similarly, the mudrock sample B was estimated to have 1.33 mL/100g volume of hydration water and 0.44 mL/100g volume of remaining fluid. Weight concentration of

kaolinite and total clay minerals in sample B were measured to be 6% and 15%, respectively. Therefore, a distinct T_2 peak appeared in sample B, which is typically observed in the process of kaolinite hydration.

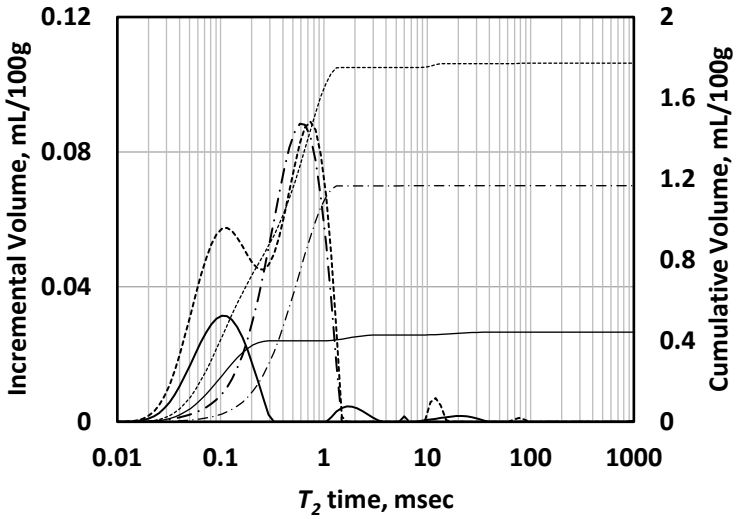

Fig. 4. 17 NMR T_2 distributions in mudrock sample B before (solid curve) and after hydration (dashed curve). The dash-dotted curve represents the calculated T_2 distributions for hydration water.

The results confirmed that higher concentration of clay minerals in the rock samples (i.e., 53.7 mass% and 15.8 mass% for mudrock samples A and B, respectively) would result in more water adsorption (i.e., 2.78 mL/100g and 1.33 mL/100g for mudrock samples A and B, respectively). The hydration of clay minerals in the two mudrock samples A and B caused 250% and 302% increase in estimates of water volume, respectively.

4.4 Conclusions

I quantified the influence of relative humidity on the hydration of clay minerals using laboratory NMR T_2 measurements. The results showed that the total fluid volume increases significantly when relative humidity increases. This increase in estimated water volume was caused by water accumulation on the surface of clay minerals (i.e., hydration of clay minerals). Montmorillonite was affected by humidity more than other clay minerals. Approximately 20 ml/100g variations in volume of hydration in montmorillonite was caused by variation of relative humidity level in the range of 0% - 95%. The results implied that hydration of clay minerals can have significant influence on assessment of water content in clay-rich formations. The results from CEC measurements confirmed a strong correlation between the volume of hydration water and the CEC of clay minerals.

Both NMR measurements and TGA confirmed the existence of interlayer water in pure-clay minerals at initial state (i.e., 0% relative humidity). The volume of interlayer water for five types of clay minerals (i.e., Na-montmorillonite, Ca-montmorillonite, illite, chlorite, and kaolinite) was estimated to be in the range of 0.77 ml/100g to 1.61 ml/100g. The volume of hydration water (or adsorbed water) in the five types of clay minerals was estimated to be in range of 1.23 ml/100g to 24.50 ml/100g. The nitrogen adsorption-desorption isothermal analysis provided the BET surface areas of five types of clay minerals. The NMR T_2 distribution also showed that the T_2 peaks, corresponding to hydration of montmorillonite and illite, overlapped with that of

interlayer water, whereas T_2 distribution of chlorite and kaolinite had two separate T_2 peaks for adsorbed water and hydration water.

In the case of organic-rich mudrocks, the NMR T_2 results showed 250% and 302% change in water volume when relative humidity changed in the range of 0% to 95%, which further verified the significant impact of humidity on core measurements. It was also confirmed that the higher concentration of clay minerals in mudrocks resulted in more sensitivity of fluid volume evaluation to the humidity level of the measurement environment.

The outcomes of this research implied the significance of humidity control during core analysis and measurements, because humidity can have a measurable influence on estimates of volumetric concentration of fluids in clay-rich rocks. To provide reliable measurements, representative of reservoir condition, I suggest that the rocks be kept at a standard humidity condition before any laboratory measurement. Corrections for the impact of humidity might also be required in certain cases depending on the type and concentration of clay minerals as well as the level of humidity.

CHAPTER V

A NEW METHOD FOR QUANTIFYING CATION EXCHANGE CAPACITY OF PURE CLAY MINERALS BASED ON THE VOLUME OF HYDRATION WATER USING NMR MEASUREMENTS*

A new method is proposed to theoretically quantify cation exchange capacity (CEC) of pure clay minerals, by use of nuclear magnetic resonance (NMR), X-ray diffraction (XRD), and nitrogen adsorption-desorption isotherm analysis. A theoretical model is introduced to estimate CEC, which is derived based on energy balance between chemical potential and electric potential energy. The change in chemical potential is a function of relative humidity and volume of hydration water. The change in electric potential energy is a function of the CEC, basal spacing, and surface area of clay minerals. XRD measurements were performed on clay minerals before and after exposure to 95% relative humidity. These measurements were used to estimate the basal spacing before and after hydration as well as the number of interlayers in each particle of clay minerals. NMR laboratory measurements were performed on the clay mineral samples before and after hydration to obtain the volume of hydration water. The nitrogen adsorption-desorption isotherms provided the surface area of clay minerals. The estimates of CEC from the new method were cross-validated against the directly-

---

measured CEC, obtained from ammonium acetate method by use of inductively coupled plasma mass spectrometry (ICP-MS) measurements. The introduced method was successfully tested on six types of clay minerals (i.e., illite, kaolinite, chlorite, and three types of montmorillonite). The calculated CEC results from the new method agreed with those from the wet chemistry method, with less than 7 meq/100g difference for all types of clay minerals. The experimental results on the performance of the new method demonstrated reliability of this method for quantification of CEC. The outcomes of this work can be potentially applied to variety of formations with measurable concentrations of clay minerals such as shaly sands and organic-rich mudrocks for reliable assessment of CEC.

5.1 Introduction

The clay minerals, which carry large number of exchangeable cations, are abundant in hydrocarbon-bearing formations, such as shaly sands and organic-rich mudrocks. The quantity of these positive exchangeable ions per unit mass of dry rock is defined as cation exchange capacity (CEC) (Johnson and Linke, 1978; Bergaya and Lagaly, 2006; Bergaya et al., 2013). The presence of the exchangeable cations in clay minerals significantly affects quantitative interpretation of electrical resistivity for assessment of hydrocarbon saturation. For instance, shaly-sand resistivity models such as Waxman-Smits (Waxman and Smits, 1968), take CEC per unit pore volume of the rock, as an input to compensate the influence of clays on electrical resistivity

measurements. Therefore, reliable assessment of CEC is crucial for dependable interpretation of electrical resistivity logs, assessment of hydrocarbon reserves, and production operations in clay-rich formations.

Methods such as wet chemistry, multiple salinity, and membrane potential are typically used for CEC quantification. There are, however, limitations associated with each one of these methods. Wet chemistry method uses ammonium or barium ions to extract the exchangeable cations from clay minerals and estimates CEC based on concentration of extracted cations (Chapman, 1965). CEC estimated using this method varies with particle size of clay minerals and pH of solution (Pinnavaia, 1983). Multiple salinity method for CEC estimation is based on resistivity measurements on the intact core plugs, which are saturated with brine at different salinity (Mian and Hilchie, 1981). This method is, however, only applicable for high permeability formations, which allow brine flow through the rock (Martin and Dacy, 2004). Membrane potential method (Thomas, 1976) requires an apparatus that could use drill cuttings as membranes in an electrochemical cell and measure the voltage using Ag-AgCl electrodes for calculating CEC. This method relies on empirical correlations between CEC and the measured voltage, obtained from previous measurements in any given shaly sand formation of interest. Such correlations are highly sensitive to the types of clay minerals in the formation and not necessarily reliable in other formations. All of the aforementioned existing methods for CEC quantification are time consuming, limited with approximations and calibration efforts, and require tedious laboratory work. Moreover, reference tables often provide a wide range of uncertainty on CEC values. Therefore, it

is necessary to develop new methods for reliable and effective quantification of CEC in rocks and rock components (e.g., clay minerals).

It is well recognized among clay mineralogists that a strong relationship exists between hydration water and cation exchange capacity. Bush and Jenkins (1977) introduced a method for CEC assessment through finding correlations between CEC and adsorbed water (i.e., hydration water) content. They compared the CEC values, which were measured from wet chemistry method, with the adsorbed water index, and established an experimental correlation between CEC and volume of hydration. This method requires much less technician time than other methods. However, it is developed based upon empirical correlations and lacks a physical model describing the correlation between CEC and volume of hydration water.

Clay swelling is significantly affected by clay-water electrochemical interactions. The type, quantity, and charge of exchangeable cations in the interlayer space can significantly impact the swelling process. There exist previous publications, investigating the process of swelling of clay minerals and clay-water interactions (Mooney et al., 1952; Norrish, 1954; Zhang and Low, 1989; Salles et al., 2008). Numerical models have been documented to investigate the swelling behavior of clay minerals based on the interaction between exchange cations, clay layers, and hydration water (Boek and Coveney, 1995; Odriozola and Aguilar, 2005). However, these models are considered expensive for the purpose of industrial use. Application of these numerical models to formations with complex composition can also be challenging (Anderson et al., 2010).

In this research, a physics-based model was developed and introduced for correlating CEC and volume of hydration water. Then, the introduced theoretical method was used for CEC estimation in clay minerals. This model took volume of hydration water, basal spacing, number of interlayers, and surface area as inputs.

5.2 Method

I proposed the following workflow for quantifying CEC of clay minerals as shown in Fig. 1. The theoretical calculation of CEC was conducted based on energy balance between chemical potential and electric potential energy. The change in electric potential energy included the energy change from hydration on the surface of clay minerals and the energy change from hydration at interlayer space in clay minerals. XRD measurement was conducted to obtain the basal spacing variation during hydration and the number of interlayers in each particle of clay minerals. N_2 adsorption-desorption isotherm analysis was carried out to get the Brunauer–Emmett–Teller (BET) surface area of clay minerals. Those experimental results were used as inputs for the calculation of electric potential energy change. The chemical potential was the Gibbs free energy from the clay hydration reaction. NMR measurements were conducted to obtain the volume of hydration water and used it as an input for calculation of total change in chemical potential. The energy balance was analyzed to obtain the calculated CEC of clay minerals. Meanwhile, ammonium acetate method was used to chemically extract cations from clay minerals (Chapman, 1965). Then, the concentrations of Na^+, Mg^{2+}, $K^{+,}$ and

Ca^{2+} ions were measured by use of inductively coupled plasma mass spectrometry (ICP-MS) and measure CEC of clay minerals. Finally, the estimated CEC from the new method was cross-validated against the chemically measured CEC using ICP-MS measurements.

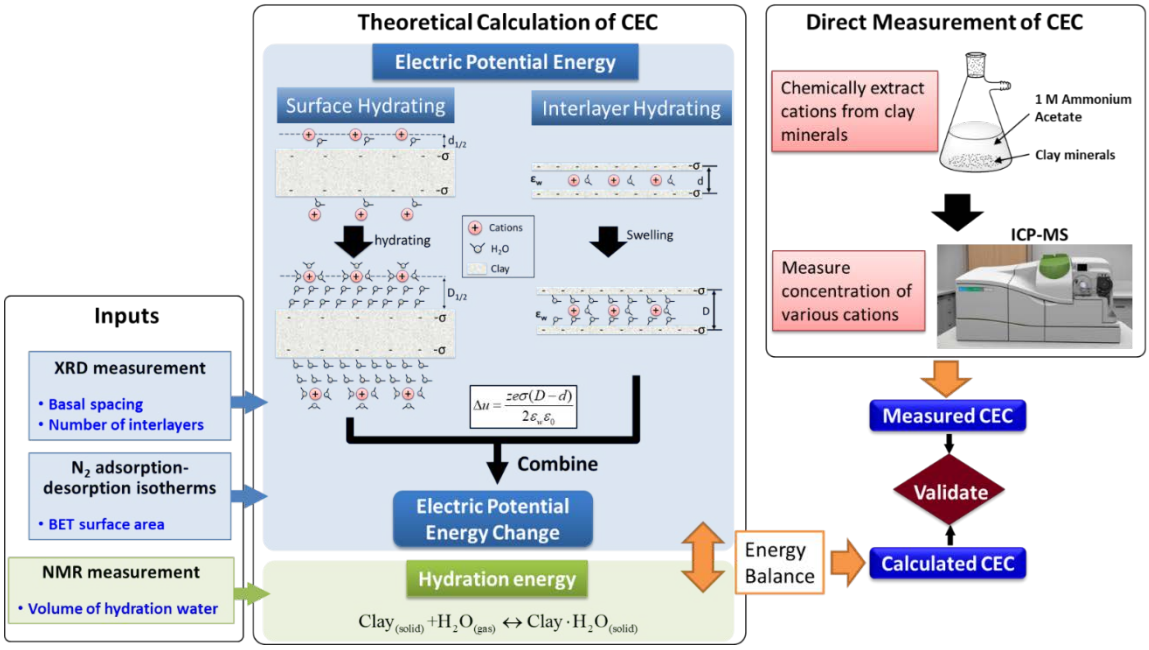

Fig. 5. 1 Workflow of the new NMR-based method for quantifying cation exchange capacity of clay minerals.

5.2.1 Experimental Procedures and Measurements

5.2.1.1 Preparation of Clay Minerals

Three types of montmorillonite (Mt1, Mt2, and Mt3), illite, chlorite, and kaolinite, were used for the experiments. Mt1 was purchased from Sigma-Aldrich and the other clay minerals were purchased from The Clay Minerals Society. Mt2, Mt3, illite, chlorite, and kaolinite samples are from Crook County, Wyoming, USA, Gonzales County, Texas, USA, Silver Hill Montana, USA, Flagstaff Hill El Dorado County,

California, USA, and Warren County, Georgia, USA, respectively. The clay mineral samples were dried in an oven at 95˚C for more than 24 hours, before starting any measurements

5.2.1.2 X-Ray Diffraction (XRD) of Clay Minerals

The structure change in clay minerals before and after hydration was evaluated by use of XRD. The XRD measurements were performed with a Bruker-AXS Venture X-ray diffractometer. The source is copper K-alpha with tube voltage of 40 kV and 25 mA currents. To capture the reflections at small angles, the data were collected from 2˚ to 70˚ with a step size of 0.02˚.

5.2.1.3 Nitrogen Adsorption-Desorption Isotherm and Surface Area Assessment

To pursue the Brunauer–Emmett–Teller (BET) surface area (SBET) of clay minerals, nitrogen adsorption-desorption experiments were conducted using Micromeritics 3flex equipment at the temperature of 77 K. The samples were degassed at temperature of 150˚C using nitrogen as the purge gas, at the beginning of the test. In the case of Mt, the BET surface area was the external surface area (Cases et al, 1992).

5.2.1.4 Relative Humidity Control and Hydration of Clay Minerals

A vacuum chamber with pure water was prepared and kept it at 25˚C for more than 24 hours to reach quasi-equilibrium. The vacuum chamber provided a closed system with 95% relative humidity (Stokes et al., 1949). The water vapor adsorption

experiments were conducted under 95% relative humidity. Approximately 10g of each clay mineral was kept on a plastic disk and maintained inside the vacuum chamber at 95% relative humidity. The clay minerals were assumed to be fully hydrated after 10 days, when water content remained unchanged. The clay mineral samples were then weighed and collected in test tubes for XRD and NMR measurements.

5.2.1.5 NMR Measurements

NMR measurements were used for quantifying the volume of hydration water after hydration process. NMR laboratory measurements were conducted using a 2 MHz benchtop NMR spectrometer. The NMR T_2 distribution measurements were carried out using a CPMG (Carr-Purcell-Meiboom-Gill) pulse sequence. The inter-echo spacing time (TE) of the CPMG pulse sequence was set to 60 µsec. The fluid volumes estimated from NMR measurements were all normalized to mL per 100 g mass of dry clay minerals. As reported in the previous work (Cheng and Heidari, 2016), The volume of hydration was estimated by subtracting the volume of water in dry clay minerals from the volume of water in hydrated clay minerals.

5.2.1.6 Inductively-Coupled Plasma Mass Spectrometry (ICP-MS) Experiments

ICP-MS measurements were used for CEC quantification for the purpose of cross-validating the outcomes of the new method. Direct measurements of CEC required the quantification of CEC for each exchangeable cation (i.e., Na^{+}, Mg^{2+}, $K^{+,}$ and Ca^{2+}). The ICP-MS measurements were conducted for quantifying the concentration of Sodium

(Na^+), Magnesium (Mg^{2+}), Potassium (K^+), and Calcium ions (Ca^{2+}) in water-based solutions. The standard calibration solution of 1000 ppm Na^+, Mg^{2+}, K^+, and Ca^{2+} was purchased from Inorganic Ventures.

5.2.1.7 CEC Measurements by Using Ammonium Acetate Method

For each type of clay mineral, two samples were prepared for CEC measurements in clay minerals Mt1 (samples Mt1.1 and Mt1.2), Mt2 (samples Mt2.1 and Mt2.2), Mt3 (samples Mt3.1 and Mt3.2), illite (samples I1 and I2), kaolinite (samples Kaol1 and Kao2), and chlorite (samples Chl1 and Chl2). Two grams of each clay mineral sample were placed in a 100-mL beaker. 25 mL of ammonium acetate at concentration of 1 mol/L was added to each beaker. The dispersion was stirred and kept overnight. Buchner funnel and vacuum pump were used to filter the suspension. The clay mineral sample was leached 3 times with 25 increments of ammonium acetate. The leachate was transferred to 250-mL volumetric flask and brought to 250 mL using deionized water. The leachate from each clay mineral was diluted for 1000 times by 2% nitric acid solution for ICP-MS measurements. The CEC of each exchangeable cation (i.e., Na^+, Mg^{2+}, K^+, and Ca^{2+}) was calculated via

$$CEC_{Na^+} = \frac{Concentration_{Na^+} \cdot V}{Mass_{clay} \cdot m_{Na^+}}, \tag{5.1}$$

$$CEC_{Mg^{2+}} = 2 \cdot \frac{Concentration_{Mg^{2+}} \cdot V}{Mass_{clay} \cdot m_{Mg^{2+}}}, \tag{5.2}$$

$$CEC_{K^+} = \frac{Concentration_{K^+} \cdot V}{Mass_{clay} \cdot m_{K^+}}, \quad (5.3)$$

and

$$CEC_{Ca^{2+}} = 2 \cdot \frac{Concentration_{Ca^{2+}} \cdot V}{Mass_{clay} \cdot m_{Ca^{2+}}}, \quad (5.4)$$

where $Mass_{clay}$ is the total mass of the clay mineral, V is the volume of leachate, and m is the atomic mass of Na^+, Mg^{2+}, K^+, and Ca^{2+}. The CEC of each clay mineral is the sum of CEC of each exchangeable cation in that clay mineral, given by

$$CEC = CEC_{Na^+} + CEC_{Mg^{2+}} + CEC_{K^+} + CEC_{Ca^{2+}}. \quad (5.5)$$

5.2.2 Theoretical Calculations

5.2.2.1 Investigation of the Basal Spacing and the Number of Interlayers of Clay Minerals

The basal spacing of clay minerals can be determined by Bragg's law (Bragg, 1933), given by

$$\eta\lambda = 2d\sin\theta, \quad (5.6)$$

where η is an integer representing the order of reflection, λ is the wavelength of XRD source (1.5418 Å), d is the basal spacing, and θ is Bragg diffraction angle.

Due to lamellar-layer structure of clay minerals, the number of interlayers can be estimated via

$$N = \tau / d, \quad (5.7)$$

where τ is the particle size of clay minerals in the lamellar direction. The particle size can be approximately estimated by Scherrer Equation (Scherrer, 1918), expressed by

$$\tau = \frac{K\lambda}{\beta \cos\theta}, \tag{5.8}$$

where K is a dimensionless shape factor, β is the line broadening at half the maximum intensity of the reflection, and θ is Bragg diffraction angle. K is approximately 0.8 for calculating the thickness of lamellar layers in one particle of clay minerals (Langford and Wilson, 1978).

5.2.2.2 Estimating the Thickness of Hydration Water on the Surface of Clay Minerals

The total hydration water includes interlayer hydration water and surface hydration water. Therefore, the thickness of hydration water on the surface of clay minerals can be estimated by

$$D_S = \frac{V_{\mathrm{HW}} - V_{\mathrm{interlayer}}}{S_{\mathrm{BET}}}, \tag{5.9}$$

where V_{HW} is the total volume of hydration water, $V_{\mathrm{interlayer}}$ is the volume of interlayer water, and S_{BET} is the BET surface area. The total volume of hydration water can be estimated using NMR T_2 measurements.

The interlayer exchangeable cations tend to adsorb water, forcing the successive layers apart (known as clay swelling). The swelling zone is filled with interlayer water. Thus, the volume of interlayer hydration water can be estimated by

$$V_{\mathrm{interlayer}} = \frac{S_{\mathrm{BET}}}{2} \cdot (D - d) \cdot (N - 1) \cdot \tag{5.10}$$

In the cases of illite, kaolinite and chlorite, where there is no swelling and *D* is equal to *d*, the volume of interlayer water is zero. Whereas, the volume of interlayer water is not zero in the case of Mt.

5.2.2.3 Surface Charge Density of Clay Minerals

Surface of clay minerals is overall negatively charged due to isomorphic substitution of metal atoms in the clay crystalline lattice (Anderson et al., 2010). This charge is neutralized by cations, which exist at interlayer space and on the surface of clay minerals. Due to electric neutrality of clay minerals, the correlation between the surface charge density of clay minerals and the measured cation exchange capacity is obtained, expressed as

$$CEC \cdot N_A \cdot e = \sigma \cdot S\,, \tag{5.11}$$

where N_A is the Avogadro constant (6.0221×10^{23} mol^{-1}), e is the elementary charge (1.6022×10^{-19} C), σ is the surface charge density of clay minerals ($C \cdot m^{-2}$), and S is the effective surface area of clay minerals ($m^2 \cdot g^{-1}$). Since CEC is in meq/100g (= 10^{-5} $mol \cdot g^{-1}$) units, **Eq. 5.11** can be rewritten as

$$\sigma = \frac{CEC}{S} \cdot 0.9648 \cdot \tag{5.12}$$

In the cases of kaolinite and chlorite, the exchangeable cations are located at the external surface. Therefore, the effective surface area required for estimating surface charge density is approximately equal to external surface area, which is BET surface area.

In the case of illite, the interlayer space is filled with potassium ions, which exactly fit into hexagonal hole in the tetrahedral sheet and form a strong interlayer bonding. These potassium ions are not exchangeable cations. Hence, only the cations on the external surface of illite contribute to CEC. The external surface area is used as the effective surface area for estimating surface charge density of illite.

In the case of Mt, **Fig. 5.2** illustrates its structure in atomic scale. Some Al at two tetrahedral sheets are replaced by Mg and some Si at octahedral sheet are replaced by Al. The combination of those substitutions leads to negatively charged layers. Thus, the surface charge density can be assumed as the combination of charges at two tetrahedral sheets and one octahedral sheet. Therefore, the effective surface area for estimating surface charge density of Mt can be approximately determined by the number of interlayers, N, and external surface area, S_{BET}, via

$$S = N \cdot \frac{S_{BET}}{2}. \tag{5.13}$$

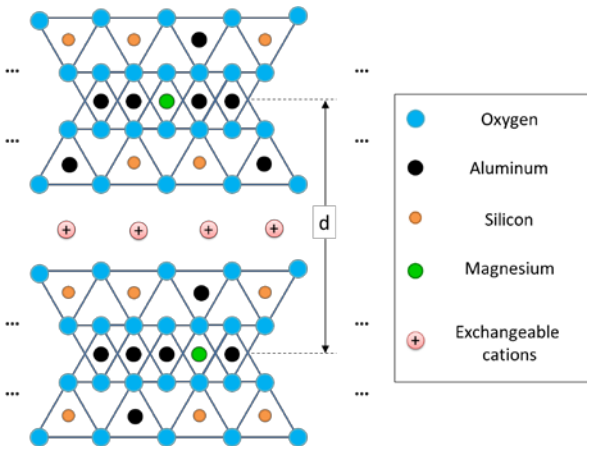

Fig. 5. 2 The structure of Mt in atomic scale.

5.2.2.4 The Change in Electric Potential Energy in the Case of Mt

The total change in electric potential energy in the case of Mt can be divided into the energy change at interlayer space and the energy change on the surface of clay minerals.

5.2.2.4.1 Energy Change at Interlayer Space

The width and length of interlayer in clay minerals are usually 300 times larger than the basal spacing (Nadeau, 1985). Therefore, it is assumed that the negatively charged surface of clay minerals is approximately an infinite charged surface. The electric field strength at interlayer space can be approximately expressed as

$$E = \frac{\sigma}{2\varepsilon_{is}\varepsilon_0}, \tag{5.14}$$

where ε_{is} is the relative permittivity of interlayer space and ε_0 is the vacuum permittivity (8.854×10^{-12} C·V^{-1}·m^{-1}).

Therefore, the electric potential energy of cations between two layers can be expressed by

$$u = ze \cdot (\frac{\sigma}{2\varepsilon_{is}\varepsilon_0} \cdot \frac{d'}{2}) \cdot 2 = \frac{ze\sigma d'}{2\varepsilon_{is}\varepsilon_0}, \tag{5.15}$$

The relative permittivity of water (ε_w) is approximately 80.4, which is significantly higher than relative permittivity of air (i.e., approximately equal to 1). Therefore, water vapor, which is abundant in air, will automatically condense in the interlayer space to decrease the electric potential energy and to become physically stable.

This explains the presence of water in the interlayer space even after the clay minerals are dried at 95˚C.

The microscopic structural variation during the process of swelling in Mt can be illustrated as **Fig. 5.3**. Water molecules enter the interlayer space, resulting in the swelling of Mt. The two/three layers of water molecules form in the interlayer space after hydration (Ferrage, et al., 2005). Since *D'*-*d'* is equal to *D*-*d*, the change in electric potential of each cation (Δu_i) can be expressed by,

$$\Delta u_i = \frac{z_i e\sigma D'}{2\varepsilon_w \varepsilon_0} - \frac{z_i e\sigma d'}{2\varepsilon_w \varepsilon_0} = \frac{z_i e\sigma (D-d)}{2\varepsilon_w \varepsilon_0}, \tag{5.16}$$

where *i* is the type of cation (i.e., Na^+, Mg^{2+}, K^+, or Ca^{2+}), z_i is the valence of cation *i*, *d'* is the distance between two successive layers before swelling, *D'* is the distance between two successive layers after swelling, *d* is the basal spacing before swelling, and *D* is the basal spacing after swelling.

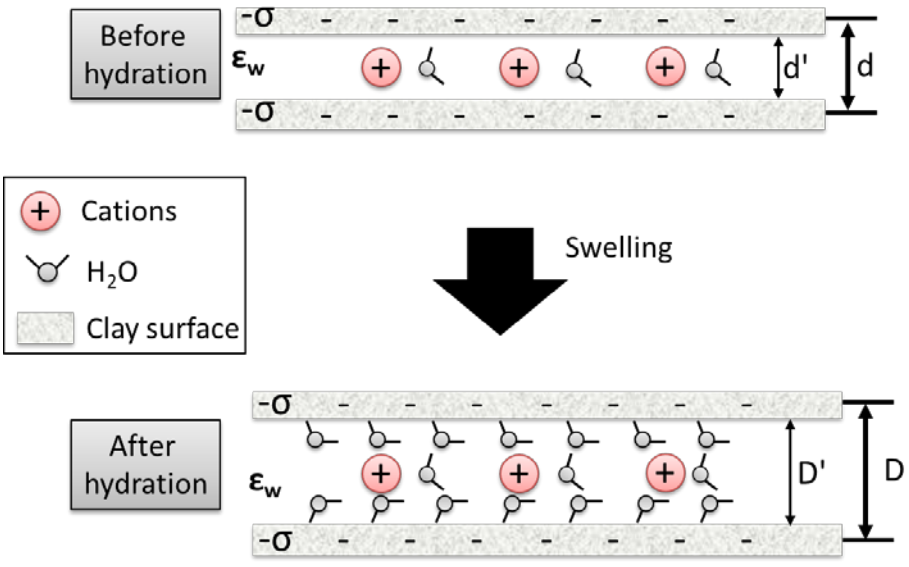

Fig. 5. 3 An illustration of hydration at interlayer space of Mt in microscopic scale.

The change in electric potential of total cations (i.e., Na^+, Mg^{2+}, K^+, and Ca^{2+}) can be written as

$$\Delta U = \sum (N_{C,i} \cdot \Delta u_i), \tag{5.17}$$

where $N_{c,i}$ is the quantity of cation i.

Substituting **Eq. 5.16** into the governing **Eq. 5.17**, the change in electric potential energy of total cations is obtained as,

$$\Delta U = \left(\sum (N_{C,i} \cdot z_i)\right) \cdot \frac{e\sigma(D-d)}{2\varepsilon_w \varepsilon_0}. \tag{5.18}$$

The CEC can be express by the quantity of valence, that is,

$$CEC \cdot N_A = \sum (N_{C,i} \cdot z_i). \tag{5.19}$$

Therefore, by substituting **Eq. 5.11** and **Eq. 5.19** into the governing **Eq. 5.18**, the change in electric potential energy can be rewritten as

$$\Delta U_{\text{interlayer}} = \frac{\sigma^2 S}{2\varepsilon_w \varepsilon_0} \cdot (D-d). \tag{5.20}$$

5.2.2.4.2 Energy Change on the Surface

The microscopic illustration for the process of hydration on the surface of clay minerals is shown in **Fig. 5.4**. The electric potential change of each cation (Δu_i) can be expressed by,

$$\Delta u_i = \frac{z_i e\sigma D_{1/2}}{2\varepsilon_w \varepsilon_0} - \frac{z_i e\sigma d_{1/2}}{2\varepsilon_w \varepsilon_0}, \tag{5.21}$$

where $D_{1/2}$ is distance from cation to the surface of clay minerals after hydration, $d_{1/2}$ is the distance from cation to the surface of clay mineral before hydration. The maximum

value of $D_{1/2}$ is equal to the thickness of hydration water on the surface of clay minerals (i.e., $D_{1/2,\,max} = D_s$).

Similarly, the total change in electric potential energy due to hydration on the surface of clay minerals can be rewritten as

$$\Delta U_{\text{surface}} = \frac{\sigma^2 S}{2\varepsilon_w \varepsilon_0} \cdot (D_{1/2} - d_{1/2}) \cdot \tag{5.22}$$

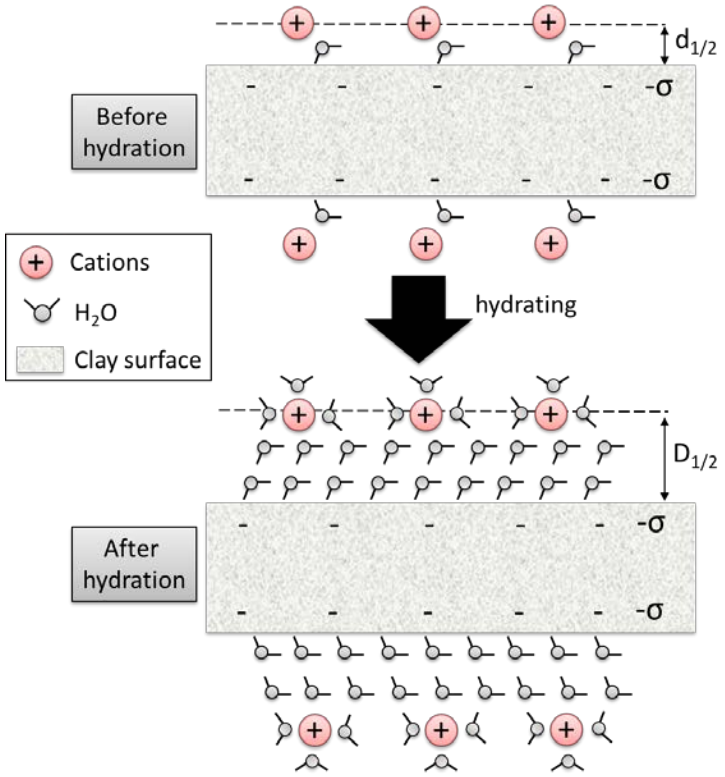

Fig. 5. 4 An illustration of hydration on the surface of clay minerals in microscopic scale.

5.2.2.4.3 The Total Change in Energy

The number of interlayers (N) in one particle of Mt can be estimated via **Eq. 5.7**. Cations exist both at interlayer space and on the surface. The number of interlayer space

and surface bearing cations is equal to N-1 and 2 (top and bottom), respectively. Thus, the number of total zones, covered with cations is equal to N+1. Assuming that cations are uniformly distributed on the surface and interlayer space, the total change in electric potential energy of Mt can be expressed by

$$\Delta U = \frac{N-1}{N+1}\Delta U_{\text{interlayer}} + \frac{2}{N+1}\Delta U_{\text{surface}} \cdot \tag{5.23}$$

5.2.2.5 The Change in Electric Potential Energy in the Cases of Illite, Kaolinite, and Chlorite

The total change in electric potential energy in the cases of illite, kaolinite, and chlorite only comes from the energy change on the surface of clay minerals, which can be expressed as

$$\Delta U = \frac{\sigma^2 S}{2\varepsilon_w \varepsilon_0} \cdot (D_{1/2} - d_{1/2}) \cdot \tag{5.24}$$

5.2.2.6 Formulation for Calculating Change in Chemical Potential

The process of hydration occurs through the chemical reaction, given by

$$\text{Clay}_{(s)} + \text{H}_2\text{O}_{(g)} \leftrightarrow \text{Clay} \cdot \text{H}_2\text{O}_{(s)}, \tag{5.25}$$

where (*s*) and (*g*) refer to solid and gaseous states, respectively.

The free energy change during the hydration process can be expressed by

$$\Delta G = \Delta G^0 + RT \ln K_p, \tag{5.26}$$

where ΔG is the Gibbs free energy change of the hydration reaction, ΔG^0 is the standard-state Gibbs free energy change of the hydration reaction, R is the gas constant (8.3145 $J \cdot K^{-1} \cdot mol^{-1}$), T is absolute temperature (in K), and K_p is the equilibrium constant. At equilibrium condition, ΔG is equal to zero. Therefore, **Eq. 5.26** converts to

$$\Delta G^0 = -RT \ln K_p, \tag{5.27}$$

where K_p can be expressed by

$$K_P = \frac{P_{\text{clay}\cdot \text{H}_2\text{O}_{(s)}}}{P_{\text{clay}_{(s)}} \cdot P_{\text{H}_2\text{O}_{(g)}}} = \frac{1}{P_{\text{H}_2\text{O}_{(g)}}}, \tag{5.28}$$

where $P_{\text{clay}\cdot \text{H2O(s)}}$ is the partial pressure of hydrated clay minerals, $P_{\text{clay(s)}}$ is the partial pressure of dry clay minerals, and $P_{\text{H2O(g)}}$ is the partial pressure of water vapor. Since partial pressures of solid states are equal to one, the equilibrium is reduced to a function of only partial pressure of water vapor.

Relative humidity (*RH*) is the ratio of the partial pressure of water vapor to the equilibrium vapor pressure of water at a given temperature, which is expressed as

$$RH = \frac{P_{\text{H}_2\text{O}_{(g)}}}{P^*_{\text{H}_2\text{O}_{(g)}}}, \tag{5.29}$$

where $P^*_{\text{H2O(g)}}$ is the equilibrium vapor pressure of water at a given temperature. It can be estimated using Tetens Equation (Tetens, 1930), given by

$$P^*_{\text{H}_2\text{O}_{(g)}} = 0.61078 \exp\left(\frac{17.27Tp}{Tp + 237.3}\right), \tag{5.30}$$

where Tp is the temperature (in ˚C).

Hence, the equilibrium vapor pressure of water at room temperature (25˚C) is 0.0313 atm (3.17 KPa).

The standard-state Gibbs free energy of the hydration reaction can be rewritten as a function of relative humidity and equilibrium vapor pressure of water, given by

$$\Delta G^0 = RT \ln RH + RT \ln P^*_{H_2O_{(g)}} . \quad (5.31)$$

The chemical potential is a form of potential energy that is released during a chemical reaction (Job and Herrmann, 2006). The change in standard-state Gibbs free energy is the energy released during the hydration process, which is equivalent to the change in chemical potential ($J \cdot mol^{-1}$), given by

$$\Delta \mu = -(RT \ln RH + RT \ln P^*_{H_2O_{(g)}}) . \quad (5.32)$$

5.2.2.7 Energy Balance between Change in Chemical Potential and Change in Electric Potential Energy

Based on energy balance, the change in electric potential energy is equal to the change in chemical potential. This energy balance can be expressed by

$$\Delta U = \frac{\rho_w V_{HW}}{m_w} \cdot \Delta \mu , \quad (5.33)$$

where ρ_w is the density of water, V_{HW} is the volume of hydration water in clay minerals, and m_w is the molar mass of water (18.0 $g \cdot mol^{-1}$). **Eq. 5.33** can be used for assessment of CEC. The final formulation for CEC can be derived for different types of clay minerals as follows:

In the case of Mt, CEC can be estimated by substituting **Eq. 5.12**, **5.20**, **5.22**, and **5.23** into **Eq. 5.33**, which leads to

$$CEC = \frac{1}{0.9648}\sqrt{S \cdot \frac{\frac{\rho_w V_{HW}}{m_w} \cdot \Delta\mu}{\frac{N-1}{N+1}\frac{(D-d)}{2\varepsilon_w\varepsilon_0} + \frac{2}{N+1}\frac{(D_{1/2}-d_{1/2})}{2\varepsilon_w\varepsilon_0}}}. \quad (5.33)$$

In the cases of illite, kaolinite, and chlorite, after substituting Equations 12 and 24 into Equation 33, CEC can be estimated by

$$CEC = \frac{1}{0.9648}\sqrt{S \cdot \frac{\frac{\rho_w V_{HW}}{m_w} \cdot \Delta\mu}{\frac{(D_{1/2}-d_{1/2})}{2\varepsilon_w\varepsilon_0}}}. \quad (5.33)$$

5.3 Results

The hydration process of Mt occurred both at the interlayer space and on the surface of the clay mineral, whereas, that of illite, kaolinite, and chlorite only occurred on the surface. Thus, the results obtained in the case of Mt and other types of clay minerals were discussed separately.

5.3.1 X-Ray Diffraction Analysis

5.3.1.1 XRD Analysis of Mt

The XRD patterns of Mt1, Mt2, and Mt3, before (blue line) and after (red line) hydration are shown in **Fig. 5.5a**, **5.5b**, and **5.5c**, respectively. The reflection index (d001) represents the interlayer space of Mt. A shift of reflection (d001) to smaller

reflection angle was observed after hydration. Based on Bragg's law (**Eq. 5.6**), this shift indicated an expansion in basal spacing. Other reflections almost overlapped before and after hydration, confirming that hydration process only occurred at interlayer space. The results showed that the basal spacing of Mt1, Mt2, and Mt3 before hydration was equal to 9.646, 9.646, and 11.97 Å, respectively. The basal spacing of Mt1, Mt2, Mt3 after hydration was equal to 16.43, 18.47, and 18.31 Å, respectively. Therefore, the basal spacing of Mt1, Mt2, and Mt3 increased by 6.48, 8.82, and 6.34 Å, respectively, after hydration. Based on Scherrer Equation, the particle size in Mt1, Mt2, and Mt3, was estimated to be equal to 139, 97, and 35 Å, respectively, in the lamellar direction. Therefore, the average number of interlayers in one particle of Mt1, Mt2, and Mt3, was approximately equal to 14, 10, and 3, respectively.

5.3.1.2 XRD Analysis of Illite, Kaolinite, and Chlorite

The X-ray diffraction patterns of illite, kaolinite, and chlorite before (blue line) and after (red line) hydration are shown in Fig**. 5.5d**, **5.5e**, and **5.5f**, respectively. The overlaps between blue and red lines at reflection index (d001) indicated that no swelling occurred in illite, kaolinite, and chlorite during the hydration process. The basal spacing of illite, kaolinite, and chlorite was estimated to be 9.990, 7.154, and 14.24 Å, respectively. Based on **Eq. 5.7** and **Eq. 5.8**, the average number of interlayers in one particle of illite, kaolinite, and chlorite was approximately equal to 17, 70, and 30, respectively.

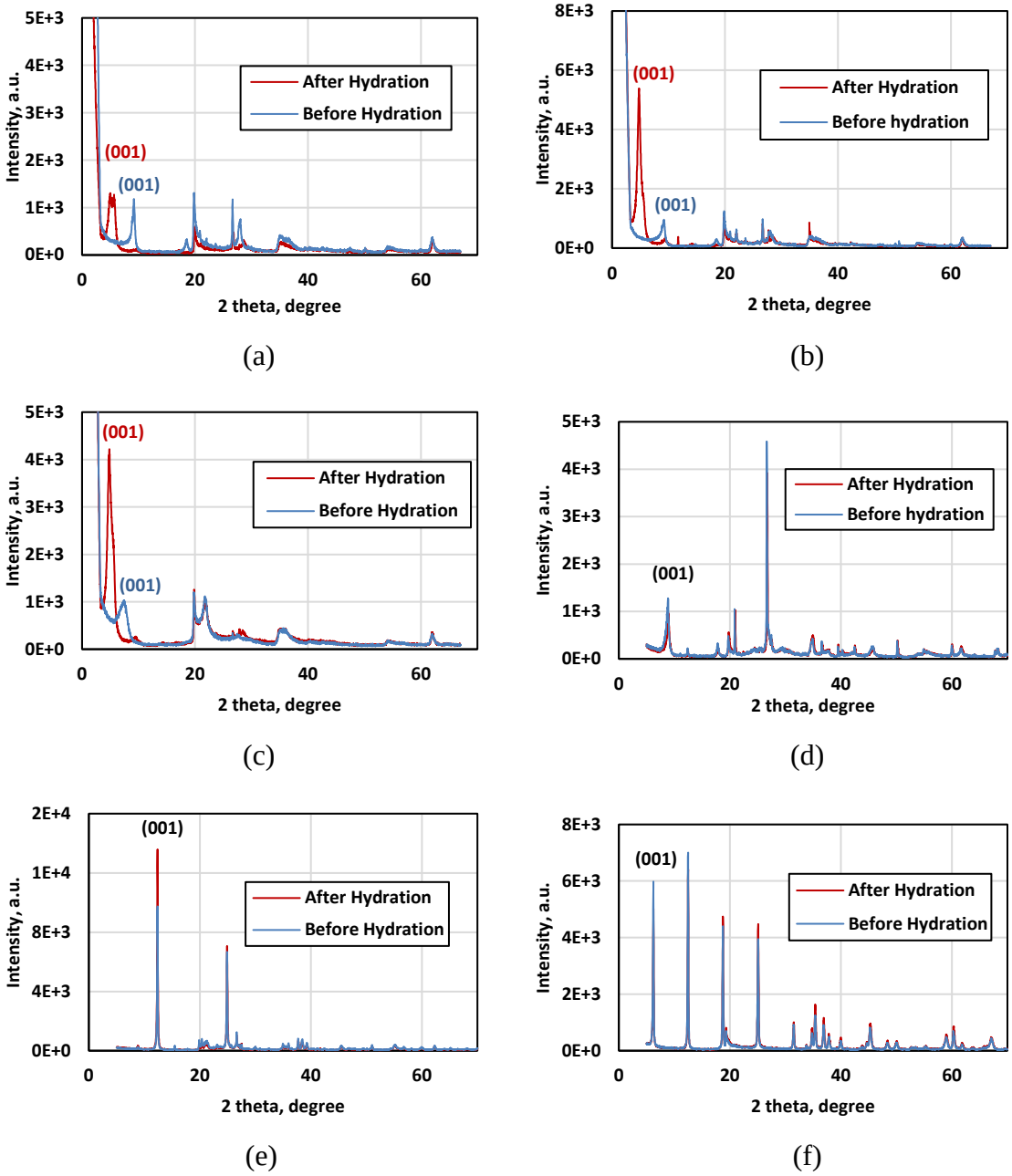

Fig. 5. 5 XRD analysis of samples (a) Mt1, (b) Mt2, and (c) Mt3, (d) illite, (e) kaolinite, and (f) chlorite samples.

5.3.2 Nitrogen Adsorption-Desorption Isotherms

5.3.2.1 Isothermal curves of Mt

The nitrogen adsorption-desorption isotherms of Mt1 (black line), Mt2 (blue line), and Mt3 (red line) are shown in **Fig. 5.6**. The demonstrated isothermal curves were type-IV isotherms with hysteresis loop, which showed the capillary condensation in multilayer adsorption (Sing et al., 1985). The shape of the hysteresis loop was indicative of lamellar mesopores between Mt particles (Cases et al., 1992; Berend et al., 1995). Based on the measured nitrogen adsorption-desorption isotherms, the BET surface areas of Mt1, Mt2, and Mt3 were estimated to be 22.40, 31.05, and 94.24 m^2/g, respectively.

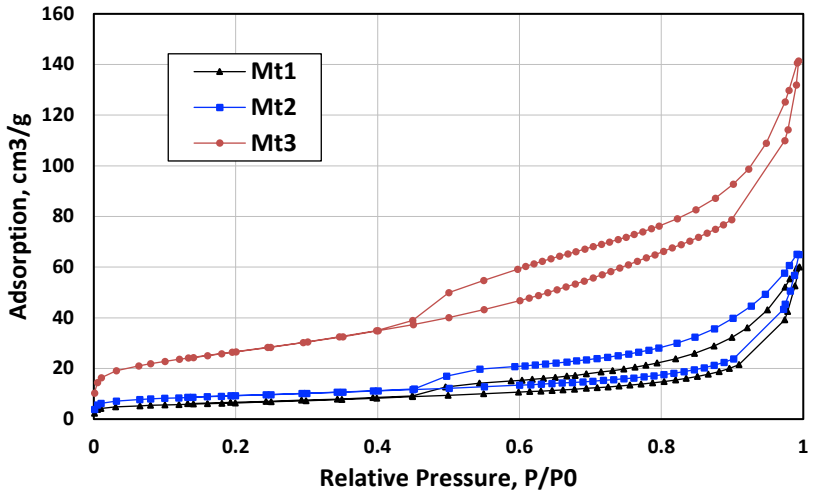

Fig. 5. 6 Nitrogen adsorption-desorption isotherms of Mt1 (black line), Mt2 (blue line), and Mt3 (red line).

5.3.2.2 Isothermal curves of illite, kaolinite, and chlorite

The nitrogen adsorption-desorption isotherms of illite (black line), kaolinite (blue line), and chlorite (red line) are shown in **Fig. 5.7**. The isothermal curve of illite was

type-IV isotherm with a hysteresis loop, indicating the presence of lamellar mesopores. Whereas, the isotherms of kaolinite and chlorite were type II isotherms without a noticeable hysteresis loop, indicating non-porous or microporous structure. The BET surface areas of illite, kaolinite, and chlorite were estimated to be 20.80, 8.49, and 8.17 m^2/g, respectively.

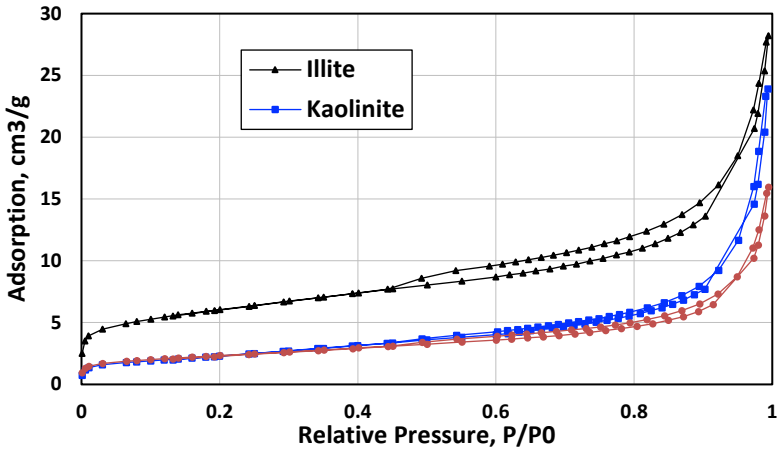

Fig. 5. 7 Nitrogen adsorption-desorption isotherms of illite (black line), kaolinite (blue line), and chlorite (red line).

5.3.3 NMR Measurements

5.3.3.1 Hydration of Mt

The NMR T_2 distributions of Mt1, Mt2, and Mt3 were measured before and after hydration (**Fig. 5.8a**, **5.8b**, and **5.8c**). A significant increase in the total water volume was observed after hydration. The initial volume of interlayer water in Mt1, Mt2, and Mt3 were measured to be 1.55, 1.41, and 2.88 mL/100g, respectively. By subtracting the initial volume of interlayer water from the total water volume, the volume of hydration water in Mt1, Mt2, and Mt3 were calculated to be 34.34, 34.67, and 36.88 mL/100g, respectively.

5.3.3.2 Hydration of illite, kaolinite, and chlorite

The NMR T_2 distributions of illite, kaolinite, and chlorite were measured before and after hydration (**Fig. 5.8d**, **5.8e**, and **5.8f**). A significant increase in total water volume was observed after hydration. The initial volume of water in illite, kaolinite, and chlorite were measured to be 1.57, 0.78, and 1.62 mL/100g, respectively. By subtracting the initial volume of water from the total water volume, the volume of hydration water in illite, kaolinite, and chlorite were calculated to be 4.62, 1.26, and 2.33 mL/100g, respectively.

5.3.3.3 Time-lapse hydration of Mt

The NMR T_2 distribution for Mt1 was recorded (**Fig. 5.9**) at adsorption times ranging from 1 hour to 10 days (hydrated state). The total water volume increased significantly with an increase in adsorption time. A slight shift of the T_2 peaks to longer relaxation times was observed. This shift can be explained by the expanding of interlayer space during swelling of Mt and the increase in thickness of hydration water at the surface of clay mineral. The volume of hydration water, measured using NMR measurements, as a function of adsorption time, is shown in **Fig. 5.10**. It was observed that hydration of Mt occurred most intensively within the first 24 hours. The total volume of water increased from initially less than 2 mL/100g to more than 20 mL/100g in 24 hours.

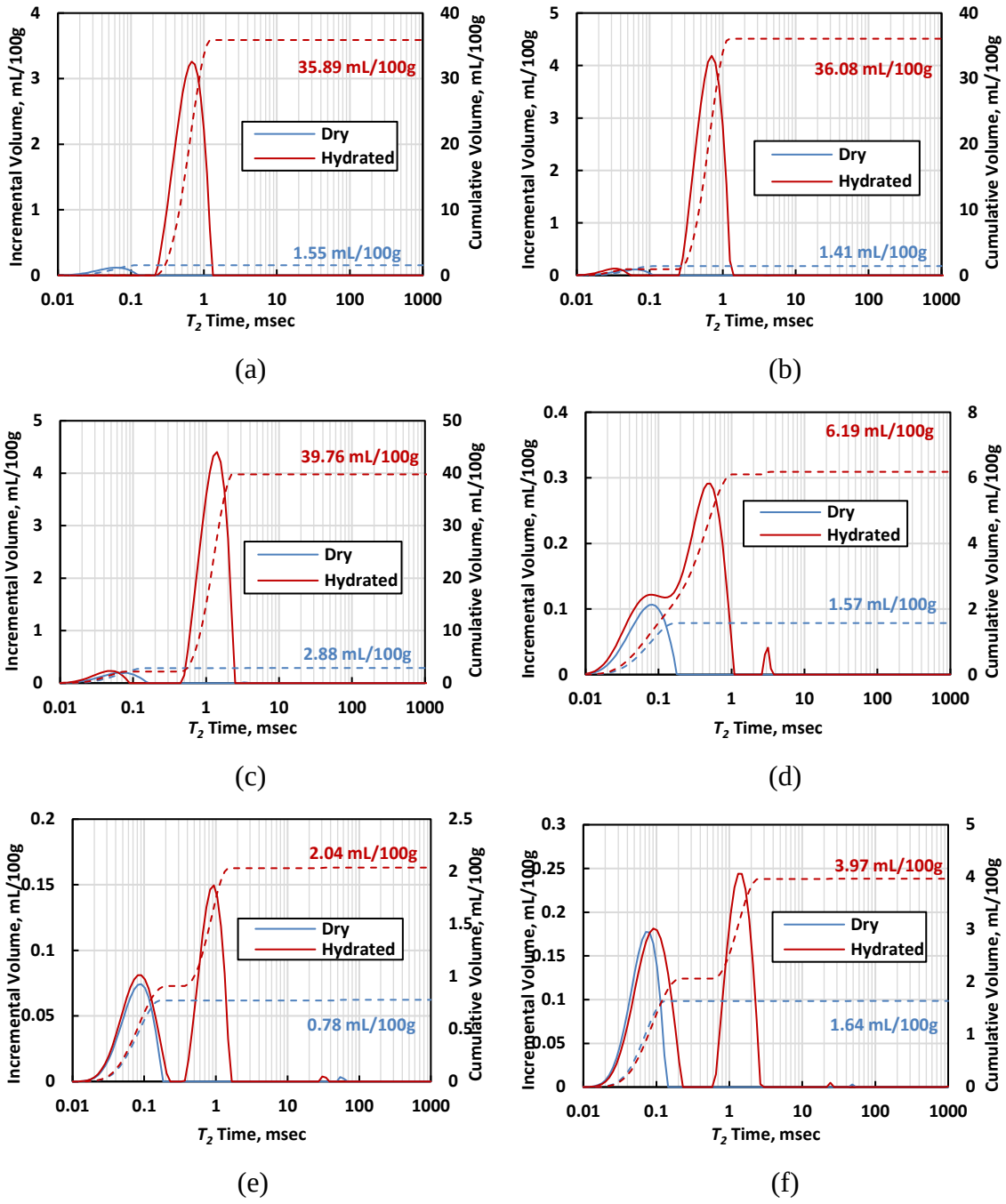

Fig. 5. 8 NMR T_2 distribution in samples of (a) Mt1, (b) Mt2, and (c) Mt3, (d) illite, (e) kaolinite, and (f) chlorite before (blue curve) and after (red curve) hydration.

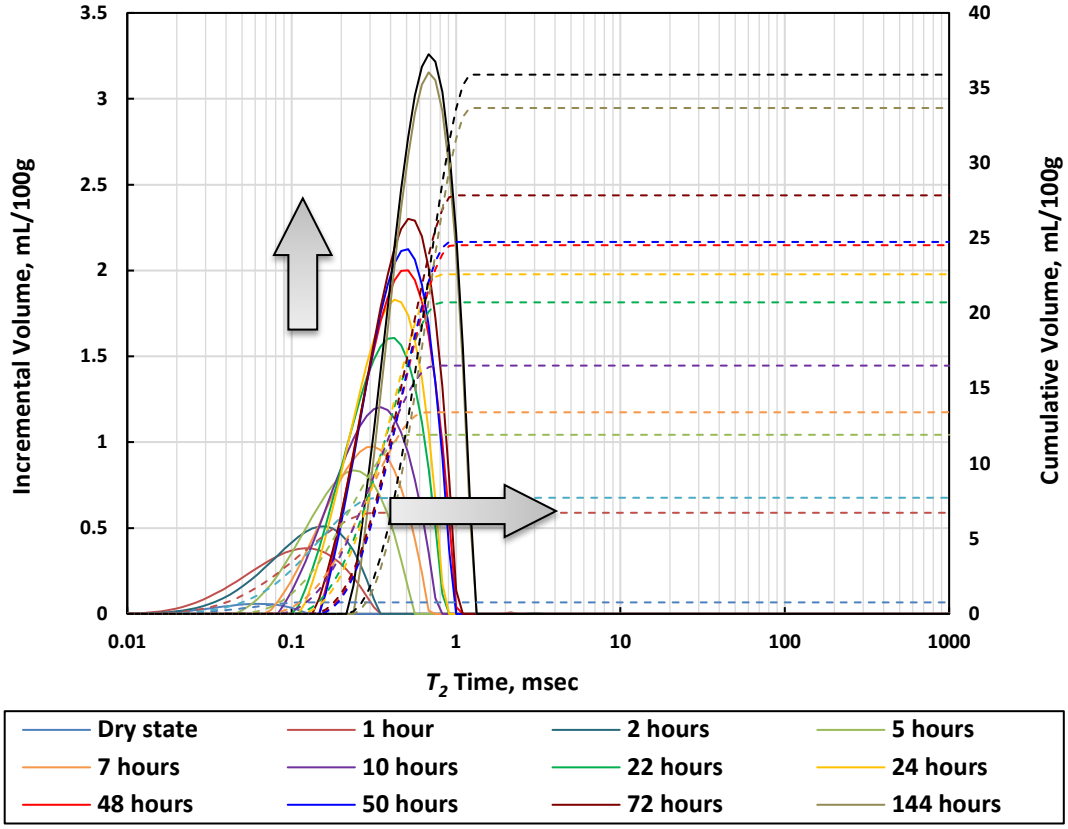

Fig. 5. 9 NMR T_2 distribution for Mt1, recorded after hydration time intervals, ranging from 1 hour to 10 days.

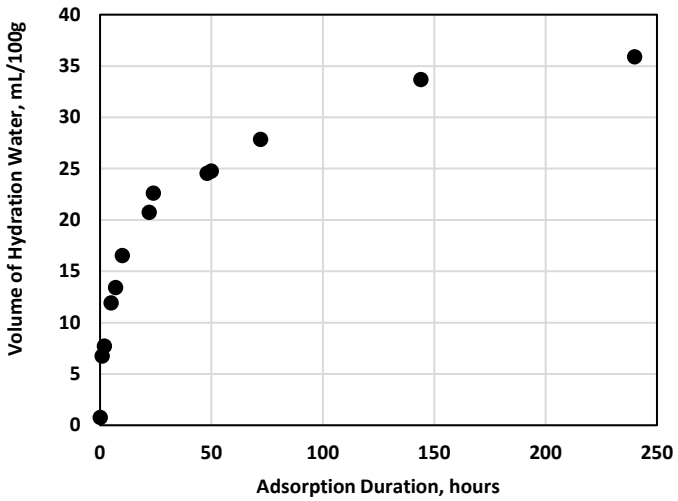

Fig. 5. 10 Volume of hydration water at different adsorption times, obtained from NMR measurements.

5.3.4 CEC Measurements

Table 5.1 lists the results of CEC of four types of cations in twelve clay mineral samples based on ammonium acetate method and ICP-MS measurements. Mt1 and Mt2 had high CEC of Na^+, but Mt3 had high CEC of Ca^{2+}, indicating that Mt1 and Mt2 were sodium-rich Mt samples and Mt3 was a calcium-rich Mt sample. The CEC of K^+ in illite sample was significantly low, confirming that potassium ions at interlayer space of illite were not exchangeable cations. **Table 5.2** lists the CEC value of each sample, calculated based on CEC of four types of cations, the average value of CEC (CEC_{avg}) for each clay mineral, and the documented CEC value in previous publications for each clay mineral. Mt had the highest CEC value compared to the rest of the clay minerals. This observation agreed with the previously documented measurements (Carroll, 1969; Ellis and Singer, 2007).

Clay Mineral	Sample No.	Na^+	Mg^{2+}	K^+	Ca^{2+}
Mt1	Mt1.1	65.5	19.0	1.84	33.8
	Mt1.2	61.3	18.0	1.47	31.2
Mt2	Mt2.1	40.6	29.4	1.38	35.6
	Mt2.2	39.7	31.0	1.32	37.0
Mt3	Mt3.1	24.5	24.8	25.6	79.8
	Mt3.2	24.6	25.3	25.9	78.5
Illite	I1	1.62	8.44	1.60	8.55
	I2	1.40	8.67	1.88	9.24
Kaolinite	Kaol1	0.41	1.93	0.38	1.85
	Kaol2	0.58	1.91	0.38	1.75
Chlorite	Chl1	0.63	7.64	0.37	1.24
	Chl2	0.76	8.76	0.92	1.75

Table 5. 1 Measured CEC of Na^+, $Mg^{2+,}$ K^+, and Ca^{2+} in Mt, illite, kaolinite, and chlorite (meq/100g) using ICP-MS measurements.

Clay Mineral	Sample No.	CEC	CEC_{avg}	Reported CEC
Mt1	Mt1.1	120.1	116.1	70-150
	Mt1.2	112.0		
Mt2	Mt2.1	106.9	108.0	
	Mt2.2	109.0		
Mt3	Mt3.1	154.7	154.5	
	Mt3.2	154.4		
Illite	I1	20.2	20.7	10-40
	I2	21.2		
Kaolinite	Kaol1	4.57	4.59	3-15
	Kaol2	4.62		
Chlorite	Chl1	9.88	11.04	10-40
	Chl2	12.19		

Table 5. 2 Comparison of CEC values (meq/100g) measured for Mt, illite, kaolinite, and chlorite samples using ammonium acetate method and the ones reported in previous publications (Carroll, 1969; Ellis and Singer, 2007).

5.3.5 CEC Assessment Using the Introduced Method

5.3.5.1 Calculation of Change in Chemical Potential

Eq. 5.32 shows that chemical potential is a function of relative humidity and equilibrium vapor pressure of water. The equilibrium vapor pressure of water is a function of temperature. The hydration process was conducted at room temperature (25˚C) and 95% relative humidity. Therefore, the chemical potential change per mole of hydration water was approximately 8.716 $KJ \cdot mol^{-1}$.

5.3.5.2 Estimation of CEC based on energy balance

The effective surface area (*S*) of clay minerals can be estimated by **Eq. 5.13**. The volume of hydration water from NMR measurements as well as XRD-based estimates of basal spacing, number of layers, and effective surface area, was used for CEC estimation through **Eq. 5.34** and **5.35**. In the cases of Mt and illite, it was assumed that the distance

from cations to the surface of clay mineral before hydration ($d_{1/2}$) was equal to half of basal spacing before hydration (d). In the cases of kaolinite and chlorite, this distance as assumed to be 5 Å. The distance from cations to the surface of clay minerals after hydration ($D_{1/2}$) was assumed to be the thickness of hydration water (D_s) at the surface of all types of clay minerals. The size of cations was assumed to be negligible compared to the distance from cations to the surface of clay minerals. The estimates of CEC were compared against those obtained from the ammonium acetate method. **Table 5.3** lists the volume of hydration water, basal spacing, average number of interlayers, thickness of hydration water at clay surface, effective surface area, surface charge density, the estimates of CEC using the new method, and the directly measured CEC using the ammonium acetate method. **Fig. 5.11** compares the calculated CEC values using the new method against those measured directly using ammonium acetate method. The results indicated that the calculated CEC using the new method agreed with the ones from the ammonium acetate method. The difference between the estimated CEC from the new method and the measured ones from the ammonium acetate method was less than 7 meq/100g.

The uncertainty of CEC calculation was mainly caused by the distance between cations and surface, which cannot be directly measured. The distance from cation to the surface before hydration ($d_{1/2}$) is similar to the distance of cation to clay minerals at the interlayer space. Therefore, it was assumed that the distance was approximately equal to half of basal spacing. However, the estimation of distance from cations to the surface after hydration ($D_{1/2}$) was challenging. A sensitivity analysis for the impact of distance

variation on CEC calculation had to be conducted, which is described in the following section.

Clay Mineral	V_{HW}	d	D	N	D_s	S	σ	CEC, New Method	Measured CEC
Mt1	34.34	9.646	16.43	12	116.0	134.4	0.75	122.0	116.1
Mt2	34.67	9.646	18.47	8	80.8	112.2	0.99	115.6	108.0
Mt3	36.88	11.97	18.31	3	32.8	141.4	1.04	152.2	154.5
Illite	4.62	9.990	9.990	17	22.2	20.80	0.98	20.3	20.7
Kaolinite	1.26	7.154	7.154	70	14.8	8.49	1.05	8.95	4.59
Chlorite	2.33	14.24	14.24	30	28.5	8.17	0.95	7.72	11.0

Table 5. 3 The volume of hydration water (V_{HW}, mL/100g), basal spacing before hydration (d, Å) and after hydration (D, Å), average number of layers (N), thickness of hydration water at surface (D_s, Å), effective surface area (S, $m^2 \cdot g^{-1}$), surface charge density (σ, $C \cdot m^{-2}$), calculated CEC from new method (meq/100g), and measured CEC (meq/100g).

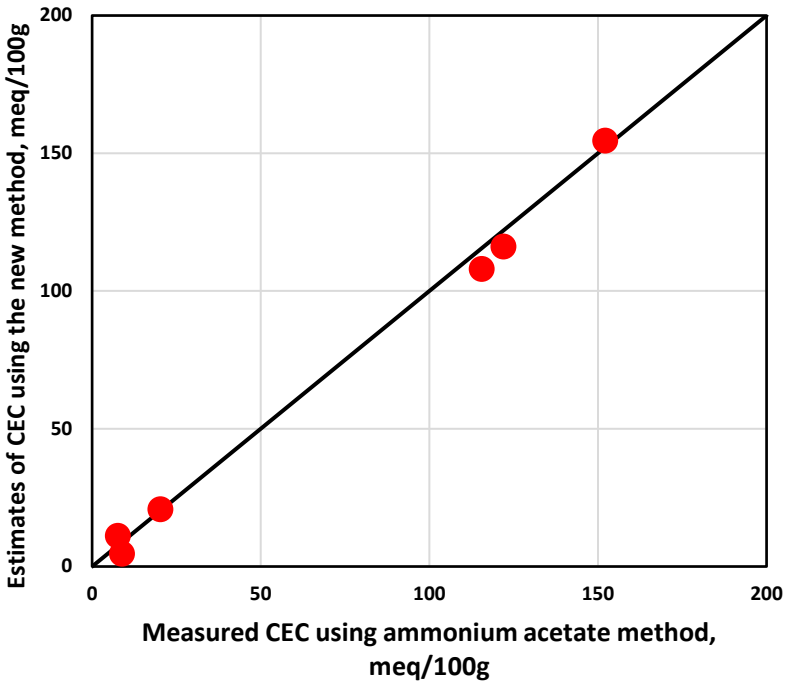

Fig. 5. 11 Comparison of the estimates of CEC from the new method against those direct measured using the ammonium acetate method.

5.3.6 Sensitivity Analysis

As discussed in the previous sections, there might be uncertainty in estimates of the distance change (before and after hydration) between cations and surface of clay minerals. This uncertainty can potentially affect estimates of CEC using the new method. To quantify the impact of this uncertainty on the final estimates of CEC, a sensitivity analysis was conducted on the distance change (before and after hydration) between cations and clay surface (i.e., $D_{1/2}$-$d_{1/2}$). The maximum value of $D_{1/2}$ (i.e., $D_{1/2,\ max}$) was assumed to be equal to the thickness of hydration water on the surface of clay minerals. Hence, the sensitivity analysis was performed for the distance change between cations and clay surface, ranging from half of $D_{1/2}$, max to $D_{1/2,\ max}$. The range of distance change (before and after hydration) for Mt1, Mt2, Mt3, illite, kaolinite, and chlorite was considered to be 54.6 – 109.2 Å, 36 – 72 Å, 16.4 – 32.8 Å, 11.1 – 22.2 Å, 7.4 – 14.8 Å, and 14.3 – 28.5 Å, respectively. **Figs. 5.12a**, **5.12b**, **5.12c**, **5.12d**, **5.12e**, and **5.12f** show the sensitivity of calculated CEC to the distance change (before and after hydration) between cations and clay surface of Mt1, Mt2, Mt3, illite, kaolinite, and chlorite, respectively. The results show that the relative changes in calculated CEC in Mt1, Mt2, Mt3, illite, kaolinite, and chlorite are 21.2%, 20.1%, 23.8%, 29.3%, 29.2%, and 29.2%, respectively. It was also observed that the uncertainty in calculated CEC in the case of Mt was less than that of illite, kaolinite, and chlorite even though the variation of distance in Mt was much larger than that of other clay minerals. The results indicated that the proposed method for CEC estimation was more accurate in Mt compared to the other clay types, documented in this chapter.

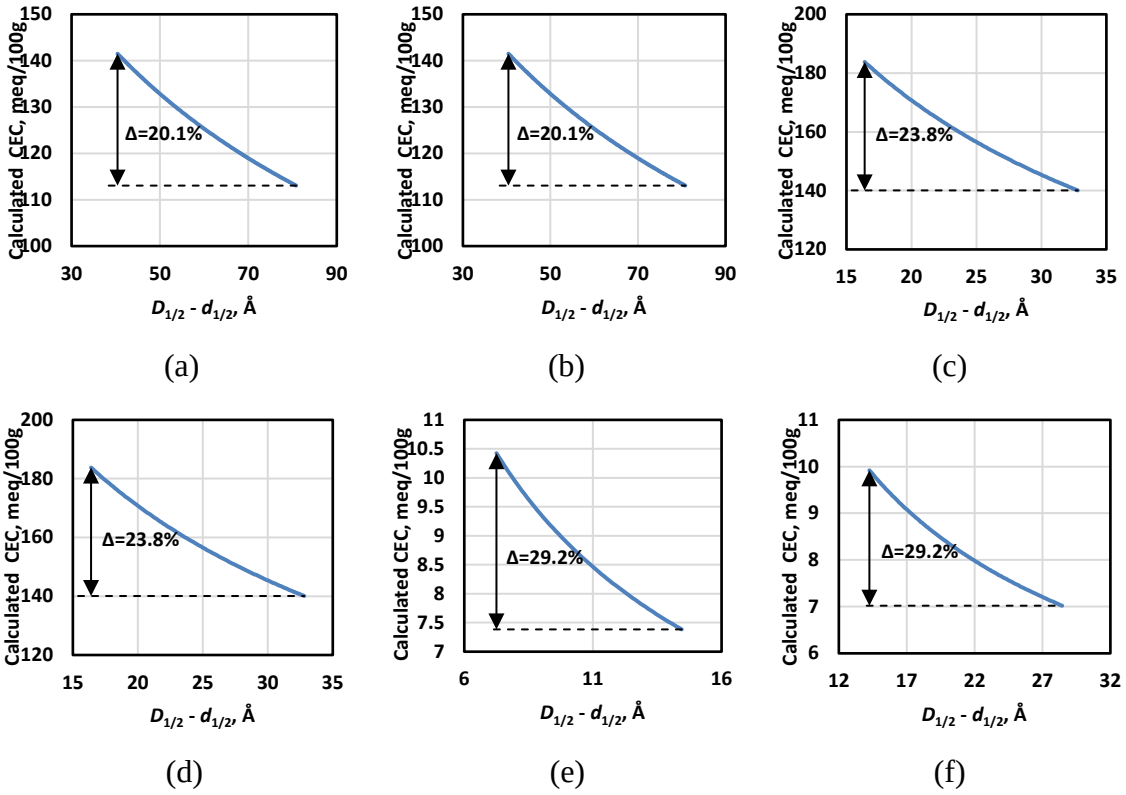

Fig. 5. 12 Sensitivity of the calculated CEC to the distance change (before and after hydration) between cations and the surface of (a) Mt1, (b) Mt2, (c) Mt3, (d) illite, (e) kaolinite, and (f) chlorite.

5.4 Conclusions

I introduced a new method to calculate the CEC of clay minerals by integrating the analysis of data collected from XRD, NMR, and nitrogen adsorption-desorption isotherm measurements. Direct measurements of CEC based on ammonium acetate method and ICP-MS measurements were used as ground truth for cross-validation of the results obtained from the new method.

The CEC values of Mt1, Mt2, Mt3, illite, kaolinite, and chlorite were calculated to be 121.99, 115.58, 152.21, 20.3, 8.95, and 7.72 meq/100g, respectively. The directly-

measured CEC of those clay minerals were 116.1, 108.0, 154.5, 20.7, 4.59, and 11.04, respectively. The calculated CEC values from the new method agreed with direct measurements, with difference of less than 7 meq/100g. One reason for this difference can be the uncertainty in distance change (before and after hydration) between cations and clay surface. Results confirmed that the introduced new method can be used for estimating CEC in different types of clay minerals.

As demonstrated in the results section, CEC can vary significantly even in the same clay types from different formations. The variation in CEC and the existing uncertainty in the look-up tables, made it important to have access to a method that can reliably estimates CEC.

The introduced method can be potentially considered more convenient for the industrial purposes compared to the wet chemistry method. The reasons include (a) wet chemistry method highly depended on chemical skills and (b) the accuracy of wet chemistry method significantly relies on every step of the procedure, such as deionized water preparation, particle size, and pH. The accuracy of the new method, however, only relies on the reliability of the equipment and the estimates of distance change (before and after hydration) between cations and clay surface. Moreover, the introduced method can be applied for any formations, while the multiple salinity method is limited to highly-permeable formations and required intact core plugs. Finally, the membrane potential method requires special equipment and relies on the empirical correlations, while the new method is analytically established on the physics-based correlations among CEC, volume of hydration water, and structure of clay minerals.

The outcomes of this research imply the feasibility of the new method for CEC estimates in any rock physics laboratory with typical equipment, such as XRD and NMR. This research only documents the new method and its application to pure clay minerals. This new method can potentially be applied to rock samples with complex mineralogy and clay minerals in the future by adding quantitative XRD measurements to the introduced workflow. With the known minerology composition of rock samples, the proposed method can be used to estimate CEC of different minerals in rock samples and then to provide the apparent CEC of rock samples. Development of tis workflow will, however, require further research and advancement of the introduced method.

CHAPTER VI

APPLICATION OF NEW NMR-BASED METHOD FOR QUANTIFYING CATION EXCHANGE CAPACITY IN SHALY SAND AND ORGANIC-RICH MUDROCK FORMATIONS*

A new workflow is proposed to quantify cation exchange capacity (CEC) in rock with complex mineralogy and presence of multiple types of clay minerals by integrating nitrogen adsorption-desorption, nuclear magnetic resonance (NMR), and X-ray diffraction (XRD) measurements (including quantitative XRD). The new workflow is developed based on the recently introduced method which theoretically calculated CEC of pure clay minerals. The successive controlled nitrogen adsorption-desorption measurements as well as NMR measurements were performed on multiple samples. Then, an inversion algorithm was introduced to estimate surface area and volume of hydration water of each mineral, which were used as inputs for CEC estimation. The CEC estimates from new workflow were compared against those from wet chemistry method by use of inductively coupled plasma mass spectrometry (ICP-MS)

---

* Sections 2, 3.2, and 4 are modified and Reprinted with permission from the Unconventional Resources Technology Conference, whose permission is required for further use (A new method for quantifying cation exchange capacity: application to organic-rich mudrock formations by Kai Cheng and Zoya Heidari, 2018, URTEC-2901029-MS, Unconventional Resources Technology Conference in Houston, Texas, USA, July 23–25). Section 3.1 is modified and reprinted with the permission from "An experimental multi-physics method for quantifying cation exchange capacity of clay-rich rocks" by Kai Cheng and Zoya Heidari, 2018, SPWLA-2018-TT, SPWLA 59th Annual Symposium in London, UK, June 2–6. Copyright 2018 by SPWLA whose permission is required for further use.

measurements and membrane potential method. For the case of shaly sand formations, the results showed that the CEC estimates from the new method and wet chemistry method were in good agreement, with less than 4 meq/100g difference. For the case of organic-rich mudrock formations, the results showed that CEC estimates from the new method agreed with those from the membrane potential method. The experimental results demonstrated reliability of the introduced method for CEC quantification. The outcomes of this research can be applied to variety of formations with complex lithology.

6.1 Introduction

Quantification of electrical rock-fluid interfacial interactions is crucial for reliable formation evaluation, since they impact borehole geophysical measurements such as electromagnetic measurements as well as fluid flow in porous media. These interactions become even more important in clay-rich formations. Cation exchange capacity (CEC), which is defined as quantity of the positive exchangeable ions per unit mass of dry rock (Johnson and Linke, 1978; Bergaya and Lagaly, 2006; Bergaya et al., 2013), is used for quantification of the clay-water interfacial interactions. Also, some shaly-sand resistivity models, such as Waxman-Smits (Waxman and Smits, 1968), take CEC per unit pore volume of the rock, as an input to compensate the influence of clays on electrical resistivity measurements. Therefore, reliable assessment of CEC is

necessary for interpretation of electrical resistivity logs and assessment of hydrocarbon reserves in clay-rich formations.

The conventional methods for CEC quantification include wet chemistry, multiple salinity, and membrane potential. However, reliable quantification of CEC is challenging due to the limitations associated with each one of these methods. Wet chemistry method uses ammonium or barium ions to extract the exchangeable cations from clay minerals and estimates CEC based on concentration of extracted cations (Chapman, 1965). CEC estimates from this method vary with particle size of clay minerals and pH of solution (Pinnavaia, 1983). This method shows successful applications in soil science. However, its application is limited in high-salinity formations. The salt precipitants in pore space inevitably cause overestimation of CEC. Multiple salinity method for CEC estimation is based on resistivity measurements on the intact core plugs, which are saturated with brine at different salinities (Mian and Hilchie, 1981). This method is, however, only applicable to high-permeability formations (Martin and Dacy, 2004). Membrane potential method (Thomas, 1976) uses cuttings as membranes in an electrochemical cell and measure the voltage for calculating CEC. This method relies on empirical correlations, which are highly sensitive to the types of clay minerals in the formation. All of the aforementioned existing methods for quantifying CEC are limited to certain formation types, approximations, and calibration efforts. Therefore, it is critical to develop new methods for reliable and effective quantification of CEC in rocks.

The relationship between hydration water and cation exchange capacity was used by Bush and Jenkins (1977) for CEC assessment. They compared the CEC values, which were measured from the wet chemistry method, with the volume of hydration water, and established an experimental correlation between CEC and volume of hydration. This method seems interesting and more cost-effective than other methods. However, it is developed based upon empirical correlations and lacks a physical model describing the correlation between CEC and volume of hydration water. Cheng and Heidari (2018) recently introduced a new method to analytically establish a correlation between CEC and volume of hydration water, as well as basal spacing and surface area, and successfully quantified CEC of pure clay minerals.

This chapter extended the application of this new method to rocks with complex mineralogy and presence of multiple types of clay minerals, including shaly sand formations and organic-rich mudrock formations. The new workflow incorporated quantitative characterization of mineral composition and TOC and an inversion algorithm to obtain volume of hydration water and surface area of each clay mineral in the powdered rock samples. CEC values of each mineral (CEC of non-clay mineral is zero) were then estimated based on the analytically-derived physics-based correlations. Finally, CEC values of the rocks can be quantified through a combination of CEC values of each mineral.

6.2 Method

6.2.1 Experimental Procedures and Measurements

6.2.1.1 Preparation of Shaly Sand and Organic Rich Mudrock Samples

Seven types of synthetic shaly sand samples (i.e., samples SR1, SR2, SR3, SR4, SR5, SR6, and SR7) were used for the experiments. The synthetic powdered rock samples were composed of quartz, montmorillonite (Mt), and illite. **Table 6.1** lists the composition of each synthetic sample. The samples were dried in an oven at 95ºC for more than 24 hours, before starting the measurements.

Sample	Quartz	Mt	Illite
SR1	90wt%	10wt%	-
SR2	80wt%	20wt%	-
SR3	90wt%	-	10wt%
SR4	80wt%	-	20wt%
SR5	80wt%	10wt%	10wt%
SR6	70wt%	20wt%	10wt%
SR7	60wt%	20wt%	20wt%

Table 6. 1 The composition of synthetic rock samples.

Six shaly sand samples (i.e., samples S1, S2, S3, S4, S5, and S6) from the same well were used for the experiments. The salinity of formation water in this formation was approximately 100 kppm, porosity was approximately 10%, and water saturation was 100%. The rock samples were ground to powder with size smaller than 63 μm (i.e., equivalent to sieve number 230). The samples were dried in an oven at 95ºC for more than 24 hours, before starting the measurements. Twelve organic-rich mudrock samples from two types of unconventional formations (formation M1 and M2) were sued for the

experiments. The mudrock samples (i.e., samples M1.1, M1.2, M1.3, M1.4, M1.5, and M1.6, and samples M2.1, M2.2, M2.3, M2.4, M2.5, and M2.6) were ground to powder with size smaller than 63. I dry the samples in an oven at 95ºC for more than 24 hours, before starting the measurements.

6.2.1.2 X-Ray Diffraction (XRD) Analysis and Quantitative XRD (QXRD) Analysis

The characterization of basal spacing and number of clay minerals was evaluated by use of XRD. The XRD measurements were performed with a Bruker-AXS Venture X-ray diffractometer. The source is copper K-alpha with tube voltage of 40 kV and 25 mA current. To capture the diffraction peaks at small angles, the data were collected from 2˚ to 70˚ with a step size of 0.02˚.

QXRD analysis was conducted by KT Geoservices. The measurements were performed using a Siemens D500 automated powder diffractometer equipped with a copper X-ray source (40kV, 30mA) and a scintillation X-ray detector. The rock samples were analyzed at the 2-theta range of 5˚ to 60˚ at a scan rate of 1˚ per minute. The glycol solvated oriented clay mounts were analyzed at the 2-theta range of 2˚ to 36˚ at a scan rate of 1˚ per minute.

6.2.1.3 Pyrolysis Measurements

The total organic carbon (TOC) of organic mudrock samples were quantified by use of HAWK analyzer. Approximately 70 mg of finely powdered mudrock (approximately 60 μm) was placed in a crucible and heated in an inert atmosphere of

helium gas. The samples were heated from 300°C to 650°C at a rate of 25°C⁄min. This ensured complete pyrolysis of organic matter (Vandenbroucke and Largeau, 2007). The outputs of pyrolysis included S1, S2, S3, S4, and T_{max}. TOC is then estimated from the output parameters.

6.2.1.4 Nitrogen Adsorption-Desorption Isotherm and Surface Area Assessment

To pursue the Brunauer–Emmett–Teller (BET) surface area (SBET) of clay minerals, nitrogen adsorption-desorption experiments were conducted using a Micromeritics 3Flex equipment at the temperature of 77 K. The samples were degassed at temperature of 150˚C using nitrogen as the purge gas, at the beginning of the test.

6.2.1.5 Relative Humidity Control and Hydration of Rock Samples

The water vapor adsorption experiments were conducted under 95% relative humidity. Approximately 10g of each sample was kept on a plastic disk and maintained inside the vacuum chamber at 95% relative humidity. The samples were assumed to be fully hydrated after 10 days, when water content remained unchanged. The samples were then weighed and collected in test tubes for XRD and NMR measurements.

6.2.1.6 NMR Measurements

NMR measurements were used for quantifying the volume of hydration water after hydration process. NMR laboratory measurements were conducted using a 2 MHz benchtop NMR spectrometer. The NMR T_2 distribution measurements were carried out

using a CPMG (Carr-Purcell-Meiboom-Gill) pulse sequence. The inter-echo spacing time (TE) of the CPMG pulse sequence was set to 100 µsec. The fluid volumes estimated from NMR measurements were all normalized to mL per 100g mass of dry samples.

6.2.1.7 Inductively-Coupled Plasma Mass Spectrometry (ICP-MS) Experiments

ICP-MS measurements were used for CEC quantification for the purpose of cross-validating the outcomes of the new method. Direct measurements of CEC required the quantification of CEC for each exchangeable cation (i.e., Na^{+}, Mg^{2+}, $K^{+,}$ and Ca^{2+}). The ICP-MS measurements were conducted for quantifying the concentration of Sodium (Na^{+}), Magnesium (Mg^{2+}), Potassium (K^{+}), and Calcium ions (Ca^{2+}) in water-based solutions. The standard calibration solution of 1000 ppm Na^{+}, Mg^{2+}, K^{+}, and Ca^{2+} was purchased from Inorganic Ventures.

6.2.1.8 CEC Measurements and Corrections

Two grams of each clay mineral sample were placed in a 100-mL beaker. 25 mL of ammonium acetate at concentration of 1 mol/L was added to each beaker. The dispersion was stirred and kept overnight. Buchner funnel and vacuum pump were used to filter the suspension. The clay mineral sample was leached 3 times with 25 increments of ammonium acetate. The leachate was transferred to 250-mL volumetric flask and brought to 250 mL using deionized water. The leachate from each clay mineral was

diluted for 1000 times by 2% nitric acid solution for ICP-MS measurements. The CEC of each exchangeable cation (i.e., Na^+, Mg^{2+}, K^+, and Ca^{2+}) was calculated via

$$CEC_{Na^+} = \frac{Concentration_{Na^+} \cdot V}{Mass_{clay} \cdot m_{Na^+}}, \quad (6.1)$$

$$CEC_{Mg^{2+}} = 2 \cdot \frac{Concentration_{Mg^{2+}} \cdot V}{Mass_{clay} \cdot m_{Mg^{2+}}}, \quad (6.2)$$

$$CEC_{K^+} = \frac{Concentration_{K^+} \cdot V}{Mass_{clay} \cdot m_{K^+}}, \quad (6.3)$$

and

$$CEC_{Ca^{2+}} = 2 \cdot \frac{Concentration_{Ca^{2+}} \cdot V}{Mass_{clay} \cdot m_{Ca^{2+}}}, \quad (6.4)$$

where $Mass_{clay}$ is the total mass of the clay mineral, V is the volume of leachate, and m is the atomic mass of Na^+, Mg^{2+}, K^+, and Ca^{2+}. The CEC of each clay mineral is the sum of CEC of each exchangeable cation in that clay mineral, given by

$$CEC = CEC_{Na^+} + CEC_{Mg^{2+}} + CEC_{K^+} + CEC_{Ca^{2+}}. \quad (6.5)$$

However, for the rock samples from high-salinity formations, salt precipitants in the rock significantly affected the CEC quantification from the ammonium acetate method and ICP-MS measurements. Therefore, for these rock samples, the measured CEC had to be corrected for the influence of salt precipitants. The CEC estimation was adjusted by adding a correction factor to consider the influence of salt precipitant, expressed by

$$CEC_{corrected} = CEC_{apparent} - Corr, \quad (6.6)$$

where $CEC_{apparent}$ is the sum of CEC for each exchangeable cation from ICP-MS measurements, and *Corr* is the correction factor, which is a function of salinity of formation fluid, porosity, and water saturation. *Corr* can be estimated via

$$Corr = \frac{Salinity \cdot \phi \cdot S_w \cdot \rho_{brine}}{\rho_{\text{rock}} \cdot m_{\text{NaCl}}}, \tag{6.7}$$

where ϕ is the porosity of the rock, S_w is the water saturation, ρ_{brine} is the density of the formation fluid, ρ_{rock} is the density of the sample, and m_{NaCl} is the molecular mass of NaCl. In experiment of actual shaly sand samples, the salinity of formation water was approximately 100 kppm, porosity was approximately 10%, and water saturation was 100%, so the correction factor *Corr* was estimated to be approximately 6.9 meq/100g.

6.2.1.9 Membrane Potential Method for CEC Quantification

I built up an apparatus for membrane potential method for CEC quantification based on Thomas's work (Thomas, 1976). The schematic diagram of the apparatus is shown in **Fig. 6.1** and actual image of the apparatus is shown in **Fig. 6.2a**. The rock-chip holder is enclosed in a Teflon holder and sealed with wax to let each face of the rock chips get exposed to a different brine solution (**Fig. 6.2b**). The salinities of two injected brines are 0.0964 mol and 1.288 mol. The injection rate is 2 mL/min. The Ag/AgCl electrodes are used for the liquid-liquid junction potential measurements. The voltage between the two brine solutions is measured by use of a multimeter at DC voltage of 200 mV with an accuracy of 0.1 mV. The CEC per unit pore volume of the rock, Q_v, can be calculated through

$$emf = \frac{-2RT}{F}\int_{m1}^{m2}\frac{t_{Na}^{hf} + R_w B_e Q_v}{1 + R_w B_e Q_v} d\ln m\gamma_{\pm}, \tag{6.8}$$

where *emf* is the liquid-liquid junction potential, *RT*/*F* is the thermodynamic constant (equal to 25.69 mV at 25 ˚C), m_1 and m_2 is the molar concentrations of brine at the two sides of the membrane, t_{Na}^{hf} is the Hittorf transport number of the sodium ion, B_e is the equivalent conductance of clay cation, $\gamma_{\pm}$ is the mean ionic activity coefficient of the electrolyte (NaCl solution).

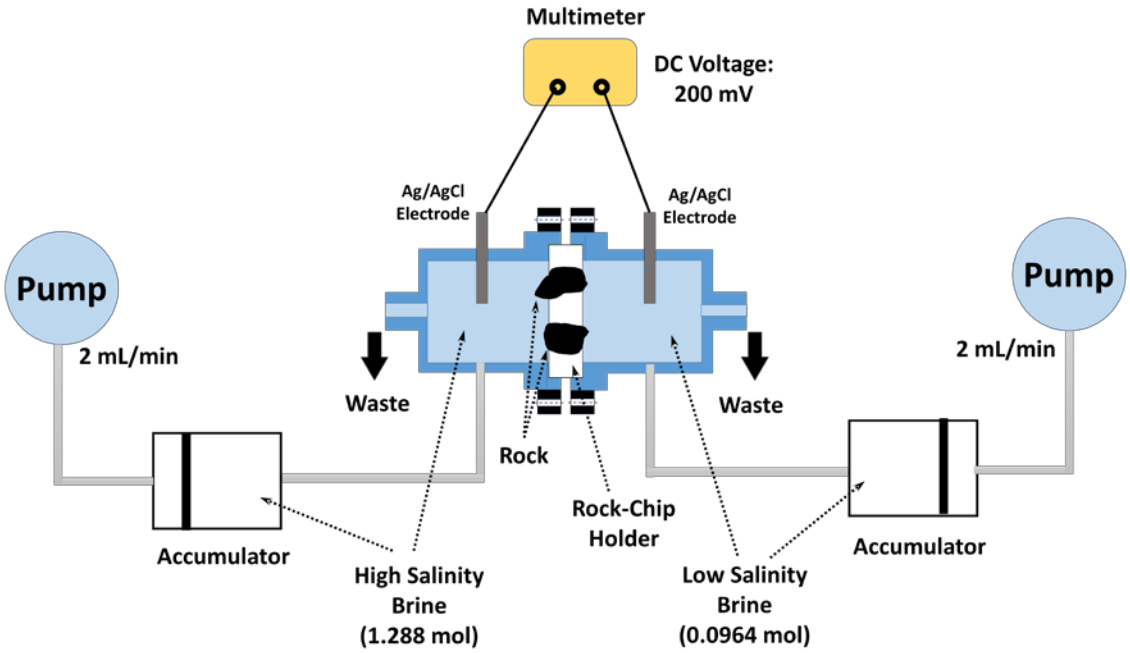

Fig. 6. 1 Schematic diagram of the apparatus designed and fabricated for performing membrane potential measurements for assessment of CEC.

The CEC from the membrane potential method is estimated through the correlation between CEC and Q_v, expressed as

$$CEC = 100 \cdot \frac{Q_v \cdot \phi}{\rho_{rock}}, \tag{6.9}$$

where ρ_{rock} is the density of the rock, which can be determined by

$$\rho_{rock} = \sum_{i}^{n} M_i \cdot \rho_i \,, \tag{6.10}$$

where ρ_i is the density of mineral i.

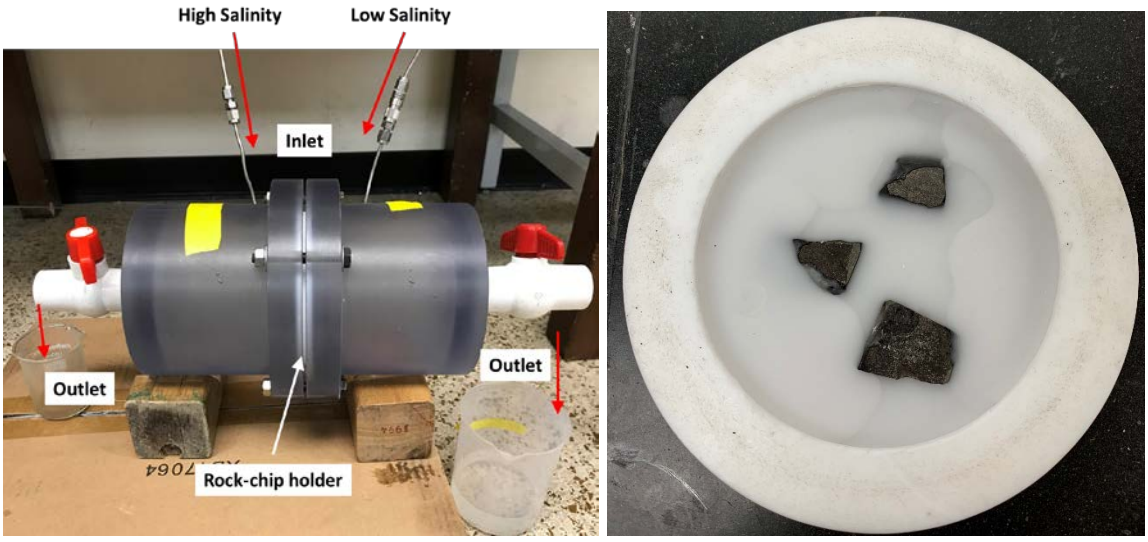

(a) (b)

Fig. 6. 2(a) The apparatus designed and fabricated for performing membrane potential measurements for assessment of CEC and (b) the rock-chip holder used for membrane potential measurements.

6.2.2 Theoretical Calculations for Pure Clay Minerals

As reported in the previous work (Cheng and Heidari, 2018), a new method was introduced for quantifying CEC of pure clay minerals based on energy balance between chemical potential and electric potential energy during hydration process. In the case of swelling clay minerals, such as montmorillonite, CEC can be estimated by

$$CEC = \frac{1}{0.9648}\sqrt{S \cdot \frac{\frac{\rho_w V_{HW}}{m_w} \cdot \Delta\mu}{\frac{N-1}{N+1}\frac{(D-d)}{2\varepsilon_w\varepsilon_0} + \frac{2}{N+1}\frac{(D_{1/2}-d_{1/2})}{2\varepsilon_w\varepsilon_0}}}\,. \tag{6.11}$$

In the case of non-swelling clay minerals, CEC can be estimated by

$$CEC = \frac{1}{0.9648}\sqrt{S \cdot \frac{\frac{\rho_w V_{HW}}{m_w} \cdot \Delta\mu}{\frac{(D_{1/2} - d_{1/2})}{2\varepsilon_w \varepsilon_0}}}, \tag{6.12}$$

where S is the effective surface area, ρ_w is the density of water, V_{HW} is the volume of hydration water, mw is the molecular mass of water, $\Delta\mu$ is the change in chemical potential of hydration reaction (8.716 KJ·mol^{-1}), N is the average number of interlayers, d is the basal spacing before hydration, D is the basal spacing after hydration, $d_{1/2}$ is the distance from cations to the surface of clay minerals before hydration, $D_{1/2}$ is the distance from cations to the surface of clay minerals after hydration, ε_0 is the vacuum permittivity, and ε_w is the relative permittivity of water.

6.2.3 Inversion Algorithm for Rocks including Multiple Types of Clay Minerals

The major challenging for CEC estimation of rocks with multiple types of clay minerals was quantification of volume of hydration water and BET surface area of each clay mineral, which were required for estimating CEC of each clay mineral as well as the CEC of the rock. NMR measurements quantified the total volume of hydration water, not the volume of hydration water for each clay mineral. Nitrogen adsorption-desorption measurement only provided the BET surface area of the whole rock samples, not BET surface area of each clay mineral. Therefore, an inversion algorithm was developed for quantifying volume of hydration water and BET surface area of each clay mineral.

6.2.3.1 Quantification of Volume of Hydration Water for Each Mineral

The total volume of hydration water was the sum of volume of hydration water for each clay mineral, which can be expressed as

$$V_{HW,total} = \sum_{j}^{n} M_j \times V_{HW,j}, \tag{6.13}$$

where j represents different types of minerals, n is the total number of clay minerals in the rock sample, M_j is the mass concentration of mineral j, and $V_{HW,j}$ is the volume of hydration water for each mineral j.

It was proposed to collect rock samples with the same composition and different concentration of mineral constituents from the same rock type. The number of required samples depended on the number of clay types existing in the rock of interest. **Eq. 6.13** can then be converted to matrix form, expressed as

$$\begin{bmatrix} M_{11} & \cdots & M_{1n} \\ \vdots & \ddots & \vdots \\ M_{k1} & \cdots & M_{kn} \end{bmatrix} \bullet \begin{bmatrix} V_{HW,1} \\ \vdots \\ V_{HW,n} \end{bmatrix} = \begin{bmatrix} V_{HW,total,1} \\ \vdots \\ V_{HW,total,k} \end{bmatrix}, \tag{6.14}$$

where k represents the number of rock samples with the same composition and different concentration of mineral constituents, M_{kn} is the mass concentration of clay mineral n in rock sample k, $V_{HW,n}$ is the volume of hydration water for clay mineral n, $V_{HW,total,k}$ is total volume of hydration for rock sample k.

To calculate the volume of hydration water for each clay mineral, **Eq. 6.14** can be rewritten as

$$\begin{bmatrix} V_{HW,1} \\ \vdots \\ V_{HW,n} \end{bmatrix} = \begin{bmatrix} M_{11} & \cdots & M_{1n} \\ \vdots & \ddots & \vdots \\ M_{k1} & \cdots & M_{kn} \end{bmatrix}^{-1} \bullet \begin{bmatrix} V_{HW,total,1} \\ \vdots \\ V_{HW,total,n} \end{bmatrix}. \tag{6.15}$$

Therefore, the volume of hydration water for each clay mineral can be quantified, as long as that the number of rock samples is equal or more than the number of clay types in the rock samples.

6.2.3.2 Quantification of Surface Area for Each Mineral

Similarly, BET surface area of a sample was the sum of surface area for each mineral, which can be expressed as

$$S_{total} = \sum_{j}^{m} M_j \times S_j \,, \tag{6.16}$$

where m is the total number of minerals in the samples and S_j is the surface area of mineral j.

Similarly, the number of required samples depended on the number of mineral types existing in the rock of interest. **Eq. 6.16** can then be converted to matrix form, expressed as

$$\begin{bmatrix} M_{11} & \cdots & M_{1m} \\ \vdots & \ddots & \vdots \\ M_{k1} & \dots & M_{km} \end{bmatrix} \bullet \begin{bmatrix} S_1 \\ \vdots \\ S_m \end{bmatrix} = \begin{bmatrix} S_{total,1} \\ \vdots \\ S_{total,k} \end{bmatrix}, \tag{6.17}$$

where M_{km} is the mass concentration of mineral m in rock sample k, S_m is the surface area for mineral m, $S_{total,\,k}$ is the BET surface of rock sample k.

To calculate surface area for each mineral, **Eq. 6.17** can be rewritten as

$$\begin{bmatrix} S_1 \\ \vdots \\ S_m \end{bmatrix} = \begin{bmatrix} M_{11} & \cdots & M_{1m} \\ \vdots & \ddots & \vdots \\ M_{k1} & \dots & M_{km} \end{bmatrix}^{-1} \bullet \begin{bmatrix} S_{total,1} \\ \vdots \\ S_{total,k} \end{bmatrix}. \tag{6.18}$$

Therefore, the surface area of each mineral can be quantified, as long as the number of rock samples is equal or more than the number of minerals in the rock type of interest.

6.2.3.3 Estimation of CEC for Rock Samples

After quantification of hydration water for each clay mineral and surface area of each clay mineral, those values can be used as inputs to **Eqs. 6.11** or **6.12** to calculate CEC of each clay mineral. Finally, the CEC of rock with multiple types of clay minerals can be calculated based on the CEC of each mineral *j*, via

$$CEC_{rock} = \sum_{j}^{n} M_j \times CEC_j \text{ ,} \tag{6.19}$$

where CEC_i is CEC of pure mineral *j*.

6.3 Results

This section documents application of the introduced CEC assessment method to synthetic and actual shaly sand samples, and two types of organic-rich mudrock samples.

6.3.1 Shaly Sand Rock Samples

6.3.1.1 Synthetic Rock Samples

6.3.1.1.1 XRD Analysis

Since the properties of minerals in synthetic rock samples are identical, one three-component synthetic rock sample (SR5) was chosen to quantify the basal spacing

variation of clay minerals. The XRD pattern of sample SR5 before (blue line) and after (red line) hydration is shown in **Fig. 6.3a**. The XRD pattern focused on a smaller range of diffraction angle is shown in **Fig. 6.3b** to better illustrate the diffraction index of basal spacing. The reflection index (d001), which represents the basal space of Mt and illite, can be observed at 2-theta of 8.881˚. The reflection index (d001) of Mt and illite overlapped, indicating that the basal spacing of Mt and illite were equal. A shift of reflection (d001) to smaller reflection angle was observed after hydration. Based on Bragg's law, this shift indicated an expansion in basal spacing of Mt. Other reflections almost overlapped before and after hydration, confirming that hydration process only occurred at interlayer space. The results showed that the basal spacing of Mt and illite were equal to 9.96 Å. The basal spacing of Mt expanded to 15.32 Å after hydration. Based on Scherrer Equation, the average number of interlayers in Mt particle was approximately 16.

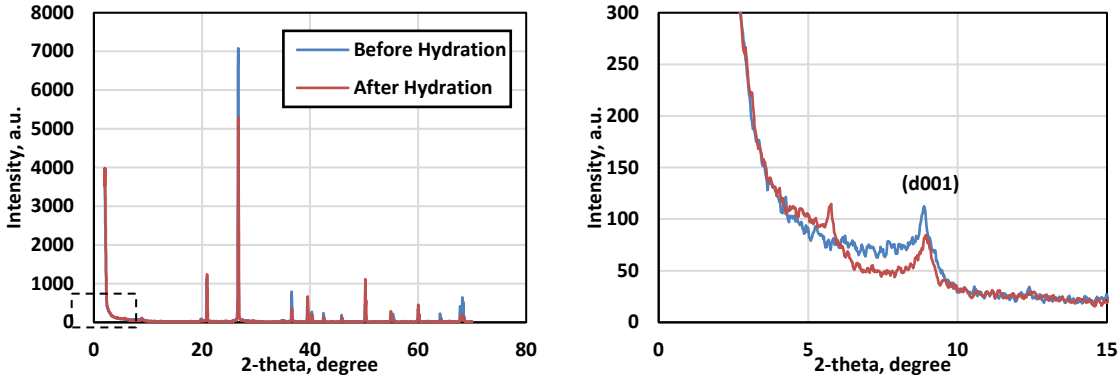

(a) (b)

Fig. 6. 3 XRD analysis of synthetic rock sample SR5.

6.3.1.1.2 Nitrogen Adsorption-Desorption Measurements

The nitrogen adsorption-desorption isotherms of pure Mt, pure quartz, and synthetic rock samples SR1 and SR2 are shown in **Fig. 6.4**. The demonstrated isothermal curves were type-IV isotherms with a hysteresis loop, which showed the capillary condensation in multilayer adsorption (Sing et al., 1985). The shape of the hysteresis loop was indicative of lamellar mesopores (Cases et al., 1992; Berend et al., 1995). Based on the measured nitrogen adsorption-desorption isotherms, the BET surface areas of Mt, quartz, SR1, and SR2 were 14.851, 0.594, 1.987, and 3.444 m^2/g, respectively. The surface area of Mt and quartz can also be estimated based on the surface area of SR1 and SR2 (**Eq. 6.18**), which were 15.10 and 0.53 m^2/g, respectively. This result indicated a good agreement between surface area estimated from inversion algorithm and the directly-measured surface area.

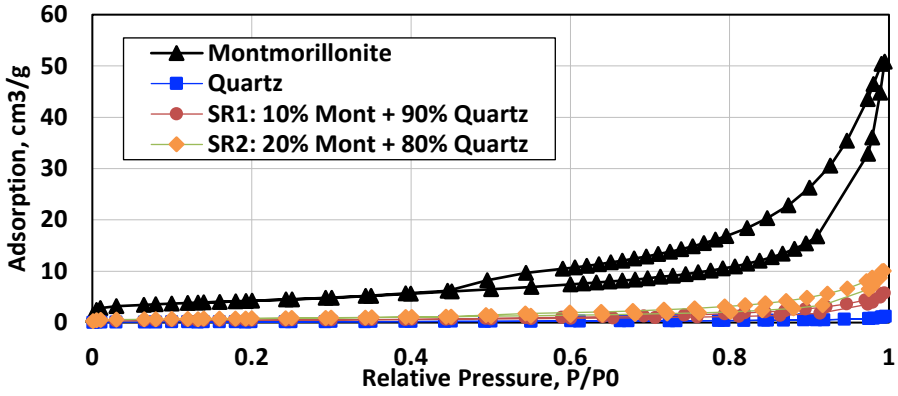

Fig. 6. 4 Nitrogen adsorption-desorption isotherms of Mt, quartz, and SR1 and SR2 samples.

The nitrogen adsorption-desorption isotherms of pure illite, pure quartz, two-component sample SR3, and sample SR4 are shown in **Fig. 6.5**. Based on the measured

nitrogen adsorption-desorption isotherms, the BET surface areas of illite, quartz, SR3, and SR4 were 20.199, 0.594, 2.445, and 4.352 m^2/g, respectively. Similarly, the surface area of illite and quartz were estimated to be 19.61 and 0.54 m^2/g, respectively, with the proposed algorithm. These estimates were in good agreements with the directly-measured surface area of the rock components.

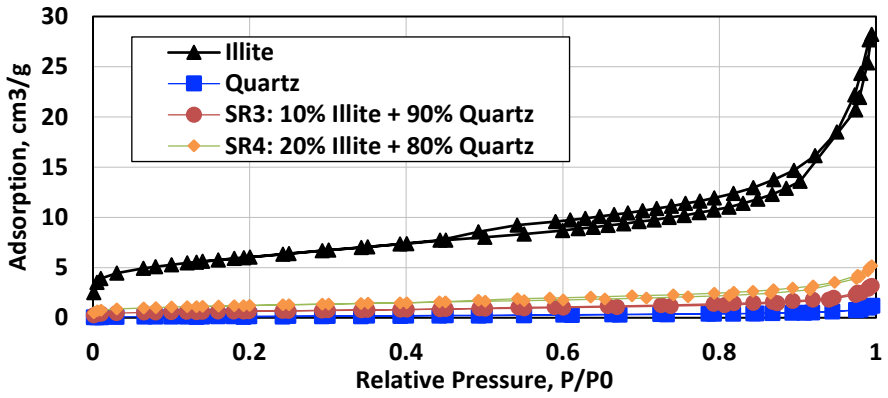

Fig. 6. 5 Nitrogen adsorption-desorption isotherms of illite, quartz, and SR3 and SR4 sample.

The nitrogen adsorption-desorption isotherms of three-component sample SR5, sample SR6, and sample SR7 are shown in **Fig. 6.6**. Based on the measured nitrogen adsorption-desorption isotherms, the BET surface areas of SR5, SR6, and SR7 were estimated to be 3.961, 5.380, and 7.398 m^2/g, respectively. Similarly, the surface area of Mt, illite, and quartz were calculated to be 14.714, 20.704, and 0.524 m^2/g, respectively, with the proposed algorithm (**Eq. 6.18**). These results indicated a good agreement between the surface areas estimated from the introduced inversion algorithm and the directly-measured surface areas for the three-component synthetic rock samples.

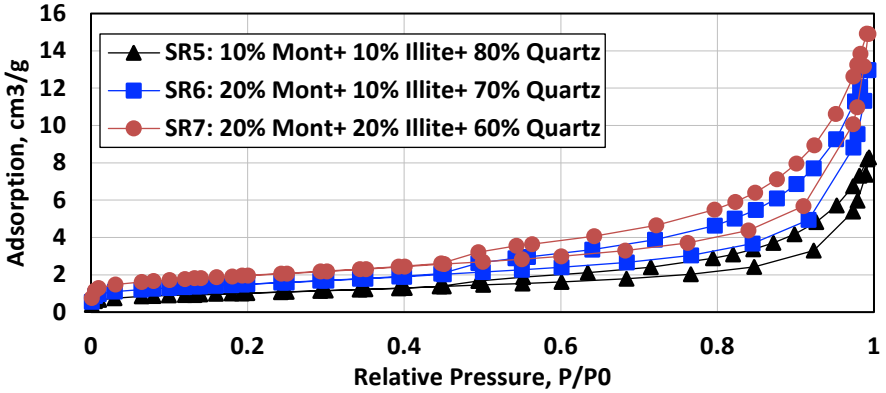

Fig. 6. 6 Nitrogen adsorption-desorption isotherms of the SR5, SR6, and SR7 samples.

6.3.1.1.3 NMR Measurements

The NMR T_2 distributions of hydration water in samples SR1 (red) and SR2 (blue) are shown in **Fig. 6.7**. The volumes of hydration water in samples SR1 and SR2 were quantified to be 3.99 and 7.97 mL/100g, respectively. Since mass concentration of Mt was 10wt% and 20wt% for samples SR1 and SR2, respectively, the volume of hydration water in unit mass of Mt was estimated to be 39.9 mL/100g.

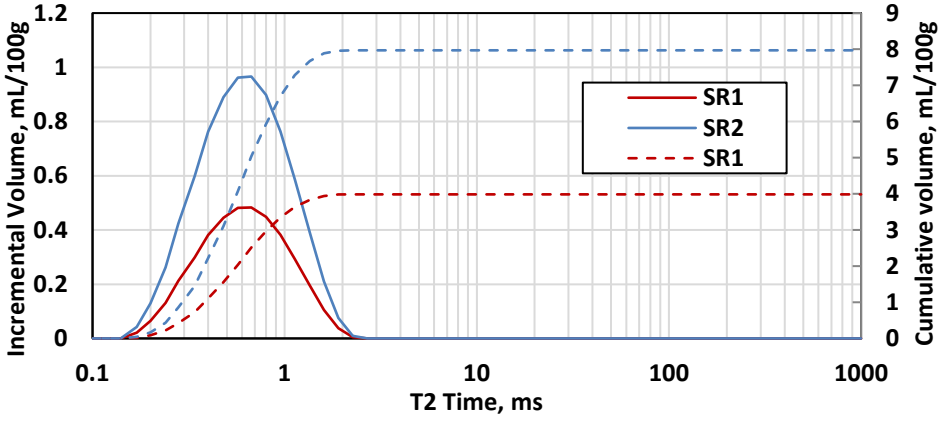

Fig. 6. 7 Hydration water quantification: T_2 distribution in samples SR1 (red) and SR2 (blue).

The NMR T_2 distributions of hydration water in samples SR3 (red) and SR4 (blue) are shown in **Fig. 6.8**. The volume of hydration water in samples SR3 and SR4 are quantified to be 0.62, and 1.24 mL/100g, respectively. Similarly, the volume of hydration water in unit weight of illite is equal to 6.2 mL/100g.

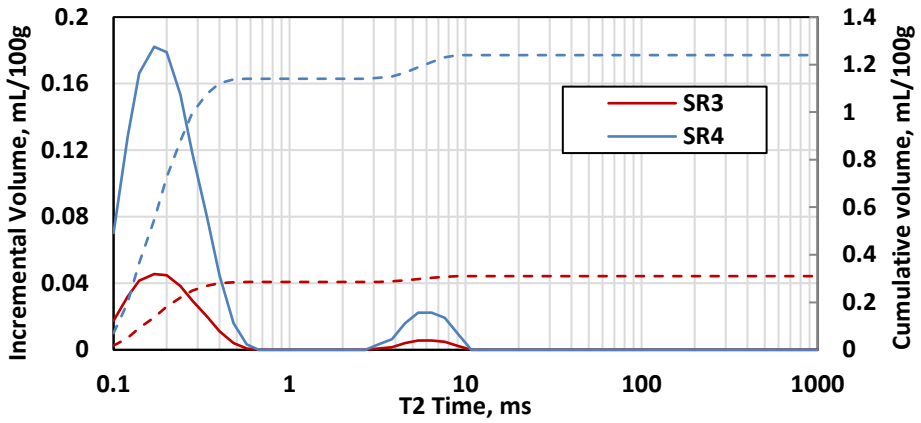

Fig. 6. 8 Hydration water quantification: T_2 distribution in samples SR3 (red) and SR4 (blue).

The NMR T_2 distributions of hydration water in three-component samples SR5 (red), SR6 (blue), and SR7 (black) are shown in **Fig. 6.9**. The volume of hydration water in SR4, SR5 and SR6 were quantified to be 4.60, 8.61, and 9.20 mL/100g, respectively. Therefore, based on **Eq. 6.15**, the volumes of hydration water in unit mass of Mt and illite were 40.1 and 5.9 mL/100g, respectively. The estimate of hydration water in the three-component samples was consistent with those from the two-component samples (i.e., samples SR1, SR2, SR3, and SR4).

The result of surface area and volume of hydration water based on the proposed inversion algorithm showed good agreement between different samples. These results

were promising for the application of the proposed workflow in rocks with multiple types of clay minerals.

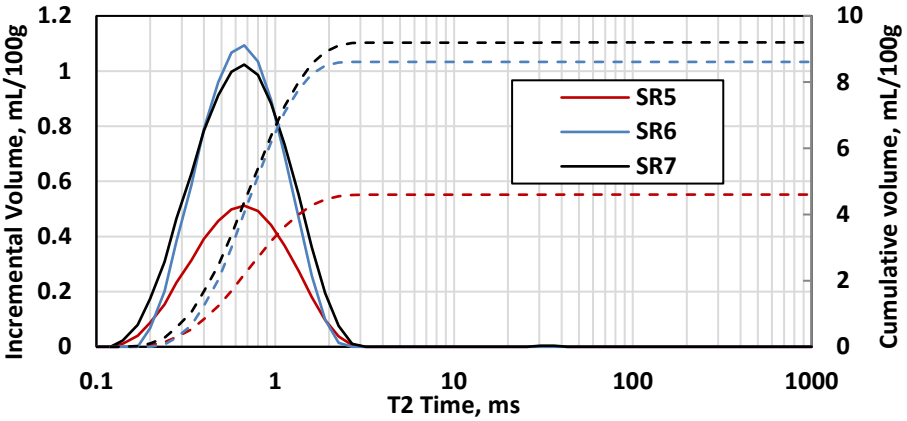

Fig. 6. 9 Hydration water quantification: T_2 distribution in samples SR5 (red), SR6 (blue), and SR7 (black).

6.3.1.1.4 ICP-MS Measurements and CEC Quantification

Table 6.2 lists the results of CEC for four types of cations and total CEC in seven synthetic rock samples based on the ammonium acetate method and the ICP-MS measurements. CEC values of the rock samples were equal to the sum of CEC values for each exchangeable cation in the sample.

Sample	**Na^+**	**Mg^{2+}**	**K^+**	**Ca^{2+}**	**CEC**
SR1	6.31	1.49	0.05	3.24	11.09
SR2	12.42	2.65	0.08	6.17	21.33
SR3	0.24	0.92	0.12	2.20	3.48
SR4	0.27	1.51	0.23	4.09	6.10
SR5	6.35	2.08	0.16	5.13	13.71
SR6	12.45	3.24	0.19	8.06	23.95
SR7	12.49	3.83	0.30	9.96	26.58

Table 6. 2 The directly measured CEC for Na+, Mg2+, K+, and Ca2+, and the total measured CEC in seven synthetic rock samples (meq/100g) using ICP-MS measurements.

6.3.1.1.5 CEC Assessment using the Introduced Method

CEC of each clay mineral component in rock samples was estimated first. The volume of hydration water from NMR measurements as well as XRD-based estimates of the basal spacing, the number of layers, and the effective surface area were used as inputs to the CEC estimation model presented in **Eqs 6.11** and **6.12**. It was assumed that the distance from cations to the surface of clay mineral before hydration ($d_{1/2}$) was equal to half of interlayer spacing before hydration (d). The distance from cations to the surface of clay minerals after hydration ($D_{1/2}$) was assumed to be equal to the thickness of hydration water (D_s) at the surface of all types of clay minerals. The size of cations was assumed to be negligible compared to the distance of cations to the surface of clay minerals. **Table 6.3** lists the volume of hydration water, the basal spacing, the average number of layers, the thickness of hydration water at clay surface, the effective surface area, and the estimates of CEC using the new method for two of the clay minerals (i.e., Mt and illite) within the rock samples. Then, CEC of the rock samples were estimated through **Eq. 6.19** based on mineral composition and the estimates of CEC were compared against those obtained from the ammonium acetate method and the ICP-MS measurements. **Table 6.4** lists the estimated and the measured CEC for each synthetic rock sample. **Fig. 6.10** compares the calculated CEC values using the new method against those measured directly using the ammonium acetate method and ICP-MS measurements.

Clay	V_{HW}	d	D	N	D_s	S	CEC, New Method
Mt	40.1	9.96	15.32	16	232.3	117.7	105.4
Illite	5.9	9.96	9.96	16	28.5	20.7	19.61

Table 6. 3 The volume of hydration water (VHW, mL/100g), the basal spacing before hydration (d, Å) and after hydration (D, Å), the average number of layers (N), the thickness of hydration water at surface (Ds, Å), the effective surface area (S, $m^2 \cdot g^{-1}$), and the estimated CEC from the new method (meq/100g) in two clay minerals.

Sample	CEC, New Method	CEC, Measured
SR1	10.54	11.09
SR2	21.08	21.33
SR3	1.96	3.48
SR4	3.92	6.10
SR5	12.50	13.71
SR6	23.04	23.95
SR7	25.00	26.58

Table 6. 4 Synthetic rock samples: comparison of the estimates of CEC from the new method against those directly measured using the ammonium acetate method. CEC values are reported in meq/100g.

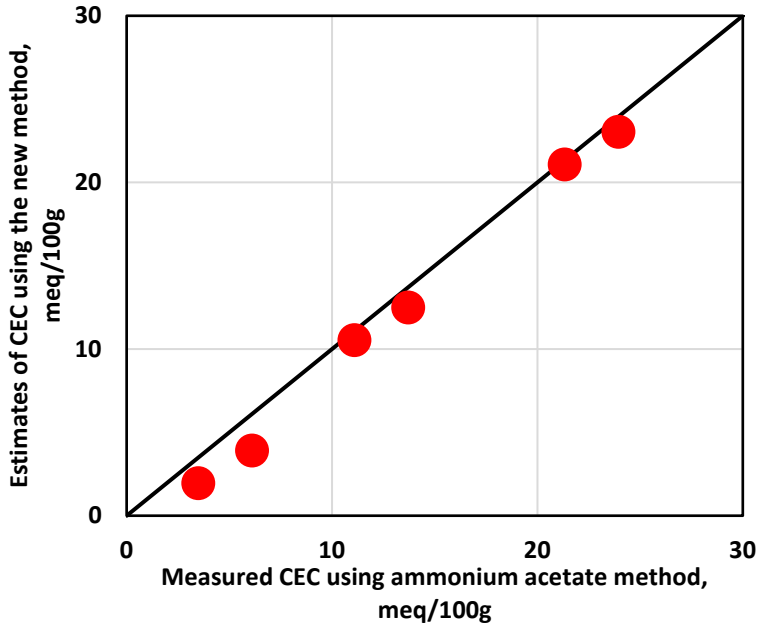

Fig. 6. 10 Synthetic rock samples: Comparison of the estimates of CEC from the new method against those directly measured using the ammonium acetate method and ICP-MS measurements.

The results indicated that the calculated CEC using the new method agreed with those from the ammonium acetate method. The difference between the estimated CEC from the new method and the measured ones from the ammonium acetate method were less than 3 meq/100g. After the successful tests in the synthetic samples, the application of the new method to actual shaly sand samples were documented in the next section.

6.3.1.2 Actual Rock Samples

6.3.1.2.1 XRD Analysis

The XRD measurements in the actual rock samples S1, S2, S3, S4, S5, and S6 before (blue line) and after (red line) hydration are show in **Figs. 6.11a–f**, respectively. Reflection indexes (d001) of illite (or Mt), kaolinite, and chlorite located at 2-theta of 8.881˚, 12.526˚, and 6.260˚, respectively. Based on Bragg's Law, the basal spacing of illite (or Mt), kaolinite, and chlorite were equal to 9.96 Å, 7.07 Å, and 14.12 Å, respectively. The shift of reflection for basal spacing before and after hydration was not observed, indicating no swelling phenomenon for the actual rock samples. It implied the concentration of swelling clay minerals, such as Mt, might be low in these rock samples.

6.3.1.2.2 Quantitative X-Ray Diffraction (QXRD) Analysis

Table 6.5 summarizes mass concentrations of dominant minerals in the six rock samples, obtained from QXRD analysis. The dominant clay types were illite, kaolinite, and chlorite. The results confirmed low contents of montmorillonite in the rock samples.

Hence, the contribution of CEC from montmorillonite was assumed to be negligible and was not considered for estimating CEC of the rock samples.

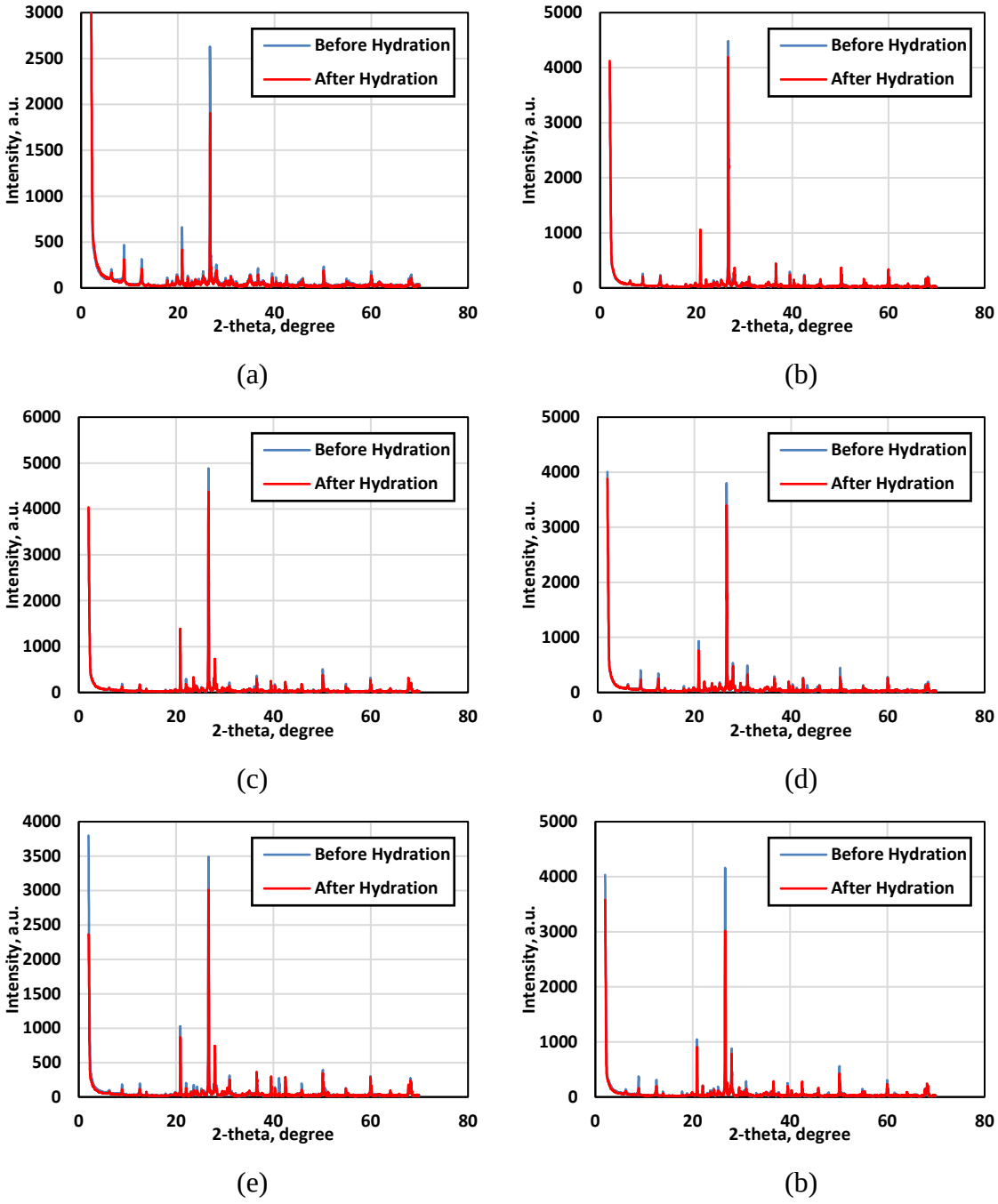

Fig. 6. 11 Actual rock samples: XRD analysis on rock samples (a) S1, (b) S2, (c) S3, (d) S4, (e) S5, and (f) S6.

Composition	S1 (wt%)	S2 (wt%)	S3 (wt%)	S4 (wt%)	S5 (wt%)	S6 (wt%)
Quartz	28.9	43.1	46.5	36.5	44.5	42.3
Feldspars	14.8	18.3	22.6	21	22	22.5
Calcite	4.6	9.4	9.2	9.8	9.9	9.9
Mt	1.4	2.1	1	1.3	1	1.1
Illite	36.5	14.1	10.5	16.9	10.7	11.8
Kaolinite	5.4	4.3	3.7	5	3.7	3.7
Chlorite	8.4	8.7	6.5	9.5	8.2	8.7

Table 6. 5 Actual rock samples: The mass concentrations of dominant minerals, obtained from QXRD analysis.

6.3.1.2.3 Nitrogen Adsorption-Desorption Measurements

The nitrogen adsorption-desorption isotherms in the rock samples S1, S2, S3, S4, S5, and S6 were measured (**Fig. 6.12**). Based on the measured nitrogen adsorption-desorption isotherms, the BET surface areas of S1, S2, S3, S4, S5, and S6 were estimated to be 16.559, 7.148, 5.894, 8.859, 6.100, and 6.613 m^2/g, respectively. Based on Equation 15 and mineral composition from QXRD, the surface area of quartz, feldspar, calcite, illite, kaolinite, and chlorite were estimated to be 0.510, 0.827, 0.517, 39.967, 8.114, 8.094 m^2/g, respectively.

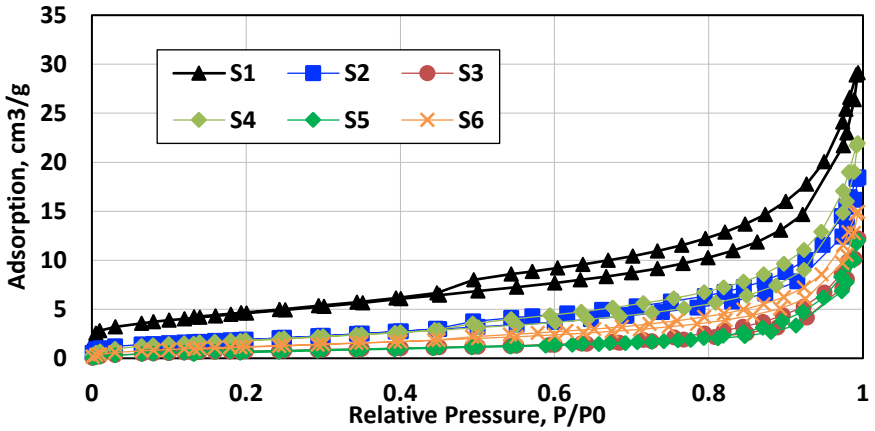

Fig. 6. 12 Nitrogen adsorption-desorption isotherms of actual rock samples S1, S2, S3, S4, S5, and S6.

6.3.1.2.4 NMR Measurements

The NMR T_2 distributions of hydration water in samples S1, S2, S3, S4, S5, and S6, are shown in **Figs. 6.13a–f**, respectively. The volumes of hydration water in S1, S2, S3, S4, S5, and S6 were quantified to be 3.926, 1.622, 1.308, 2.037, 1.360, and 1.483 mL/100g, respectively. Based on **Eq. 6.15** and mineral composition from QXRD, the volume of hydration water from illite, kaolinite, and chlorite were estimated to be 9.65, 2.11, and 1.84 mL/100g, respectively.

6.3.1.2.5 ICP-MS Measurements and CEC Quantification

Table 6.6 lists the results of CEC for four types of cations and total CEC in six actual rock samples based on the ammonium acetate method and the ICP-MS measurements. The CEC quantified from ICP-MS measurements had to be corrected for the influence of salt precipitation in actual rock samples.

Sample	**Na^+**	**Mg^{2+}**	**K^+**	**Ca^{2+}**	**CEC**
S1	6.05	2.30	0.00	13.25	21.60
S2	3.24	2.04	0.06	7.15	12.49
S3	4.06	0.60	1.06	9.47	15.19
S4	4.21	1.00	0.73	5.59	11.53
S5	3.55	1.57	0.00	9.57	14.69
S6	5.34	1.06	0.00	8.56	14.96

Table 6. 6 The directly measured CEC for Na^+, Mg^{2+}, K^+, and Ca^{2+}, and the total measured CEC in six actual rock samples (meq/100g) using ICP-MS measurements.

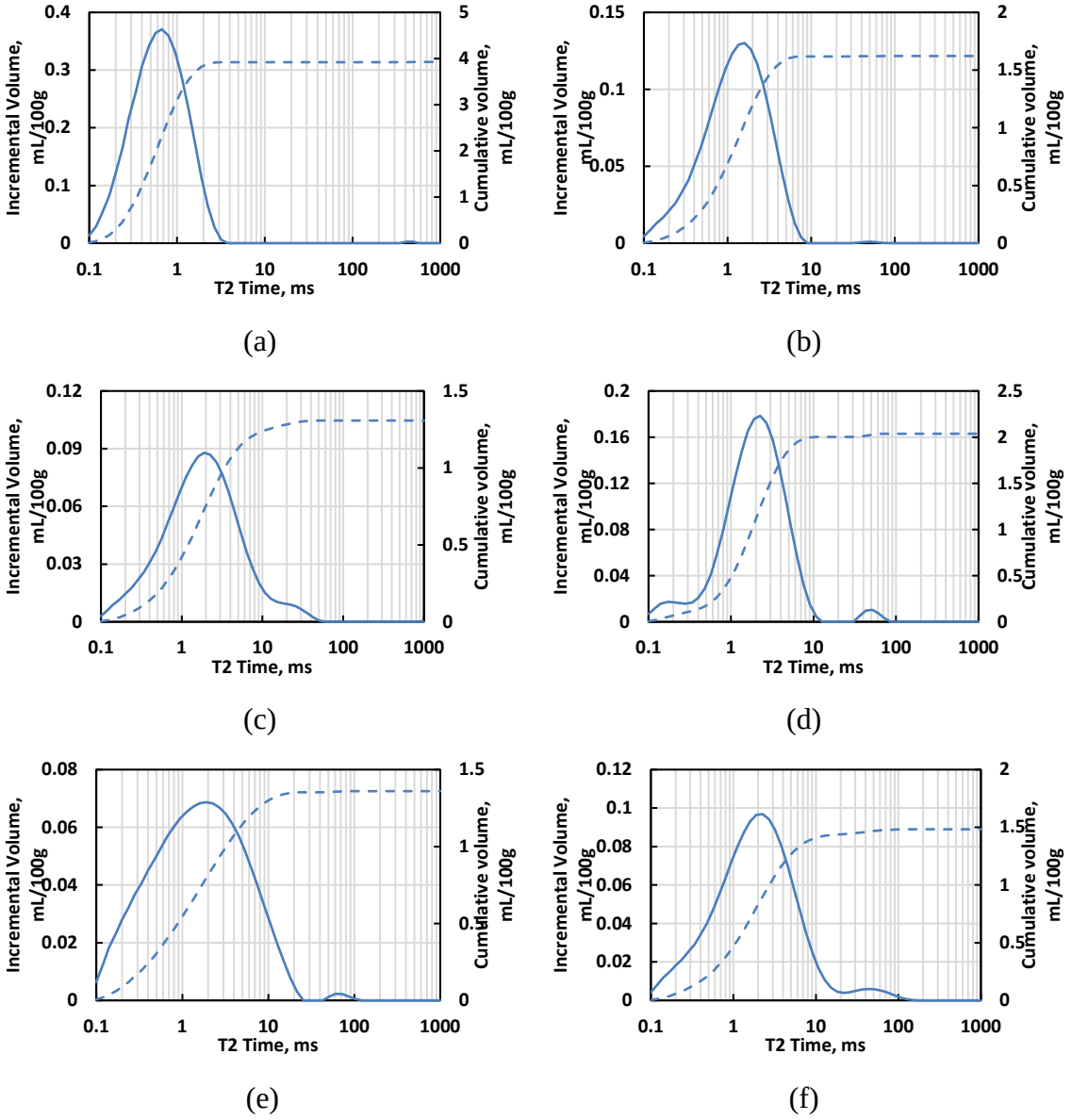

Fig. 6. 13 Hydration water quantification in actual rock samples: NMR T_2 distribution in samples (a) S1, (b) S2, (c) S3, (d) S4, (e) S5, and (f) S6.

6.3.1.2.6 CEC Assessment Using the Introduced Method

The CEC of each clay mineral in the actual rock samples was estimated first. The volume of hydration water from NMR measurements as well as the basal spacing, the

number of layers, and the effective surface area were used as inputs to the CEC estimation model presented in **Eq. 6.12**. **Table 6.7** lists the volume of hydration water, the basal spacing, the average number of layers, the thickness of hydration water at clay surface, the effective surface area, and the estimates of CEC using the new method for three of the clay minerals (i.e. illite, kaolinite, and chlorite) within the rock samples. Then, the CEC of the rock sample were estimated through **Eq. 6.19** based on mineral composition. The estimates of CEC obtained from the ammonium acetate method and ICP-MS measurements were corrected for the influence of salt precipitant through Equation 6. Finally, the estimates of CEC from proposed method were compared against the measured CEC after correction for salt precipitation. **Table 6.8** lists the estimated and the measured CEC for actual rock samples before and after correction. **Fig. 6.14** compares the CEC values from proposed method against those measured directly using the ammonium acetate method (after correction). The results indicated that the estimated CEC values from the new method agreed with those from the ammonium acetate method, with difference of less than 4 meq/100g.

Clay	V_{HW}	d	D_s	S	**CEC**
Illite	9.65	9.96	24.1	39.97	38.60
Kaolinite	2.11	7.07	26.0	8.11	7.76
Chlorite	1.84	14.12	22.7	8.09	7.88

Table 6. 7 For each clay mineral, the volume of hydration water (V_{HW}, mL/100g), basal spacing (d, Å), thickness of hydration water at surface (D_s, Å), effective surface area (S, $m^2 \cdot g^{-1}$), estimated CEC from new method (meq/100g).

Sample	CEC, New Method	CEC, Measured	CEC, Corrected
S1	15.71	21.60	14.7
S2	6.50	12.49	5.59
S3	5.24	15.19	8.29
S4	8.16	11.53	4.63
S5	5.45	14.69	7.79
S6	5.95	14.96	8.06

Table 6. 8 Actual rock samples: comparison of the estimates of CEC from the new method against those directly measured using the ammonium acetate method (before and after correction). CEC values are reported in meq/100g.

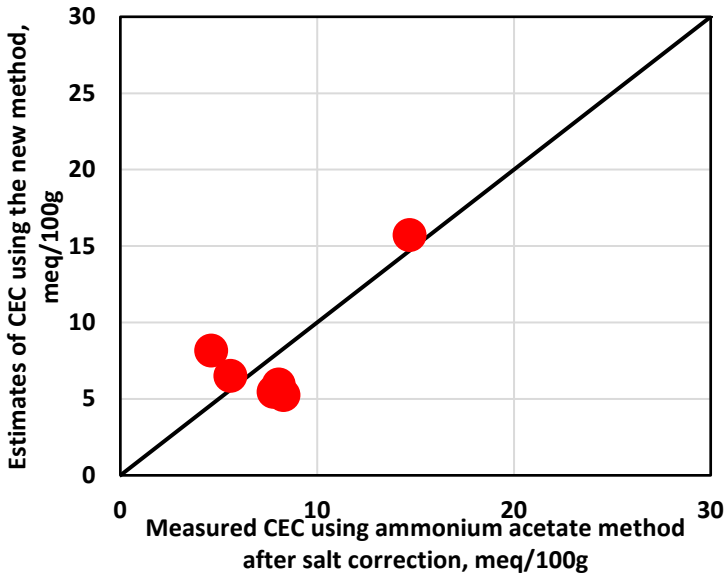

Fig. 6. 14 Actual rock samples: Comparison of the estimates of CEC from the new method against those directly measured using the ammonium acetate method after salt correction.

6.3.2 Organic-Rich Mudrock Samples

6.3.2.1 Formation M1

6.3.2.1.1 XRD Analysis

The XRD measurements in the organic-rich mudrock samples M1.1, M1.2, M1.3, M1.4, M1.5, and M1.6 before (blue line) and after (red line) hydration are show in

Figs. 6.15a–f, respectively. Reflection indexes (d001) of illite (or Mt) and chlorite cannot be detected in the measurements, indicating low concentration of illite (or Mt) and chlorite in the mudrock samples. Reflection index of kaolinite can be observed and locates at 2-theta of 12.383˚. Based on Bragg's Law, the basal spacing of kaolinite was equal to 7.15 Å. The shift of reflection for basal spacing before and after hydration was not detectable, indicating that no swelling phenomenon was observed for the rock samples. This observation also implied the concentration of swelling clay minerals, such as montmorillonite, might be low in these rock samples.

6.3.2.1.2 Mineralogy and TOC Analysis

Table 6.9 summarizes weight concentrations of dominant minerals and TOC in the six rock samples M1.1–M1.6, obtained from quantitative XRD analysis and pyrolysis. The dominant clay types were illite, kaolinite, and chlorite. The results confirmed absence of montmorillonite and low contents of illite and chlorite in the rock samples. TOC of the mudrock samples M1.1–M1.6 were in range of 3.5wt% to 5.5wt%.

Composition	**M1.1 (wt%)**	**M1.2 (wt%)**	**M1.3 (wt%)**	**M1.4 (wt%)**	**M1.5 (wt%)**	**M1.6 (wt%)**
Quartz	19.4	20.5	18.1	20.7	19.2	19.6
Feldspars	1.0	0.7	0.0	0.7	0.5	0.7
Calcite	59.8	61.8	71.0	61.3	60.2	60.9
Mt	0.0	0.0	0.0	0.0	0.0	0.0
Illite	2.4	2.8	1.5	2.4	2.7	3.1
Kaolinite	11.0	9.7	5.0	8.8	10.8	9.5
Chlorite	1.0	0.9	0.6	0.8	1.3	0.9
TOC	5.32	3.63	3.82	5.38	5.26	5.28

Table 6. 9 The weight concentrations of dominant minerals in the mudrock samples M1.1–M1.6 obtained from QXRD analysis.

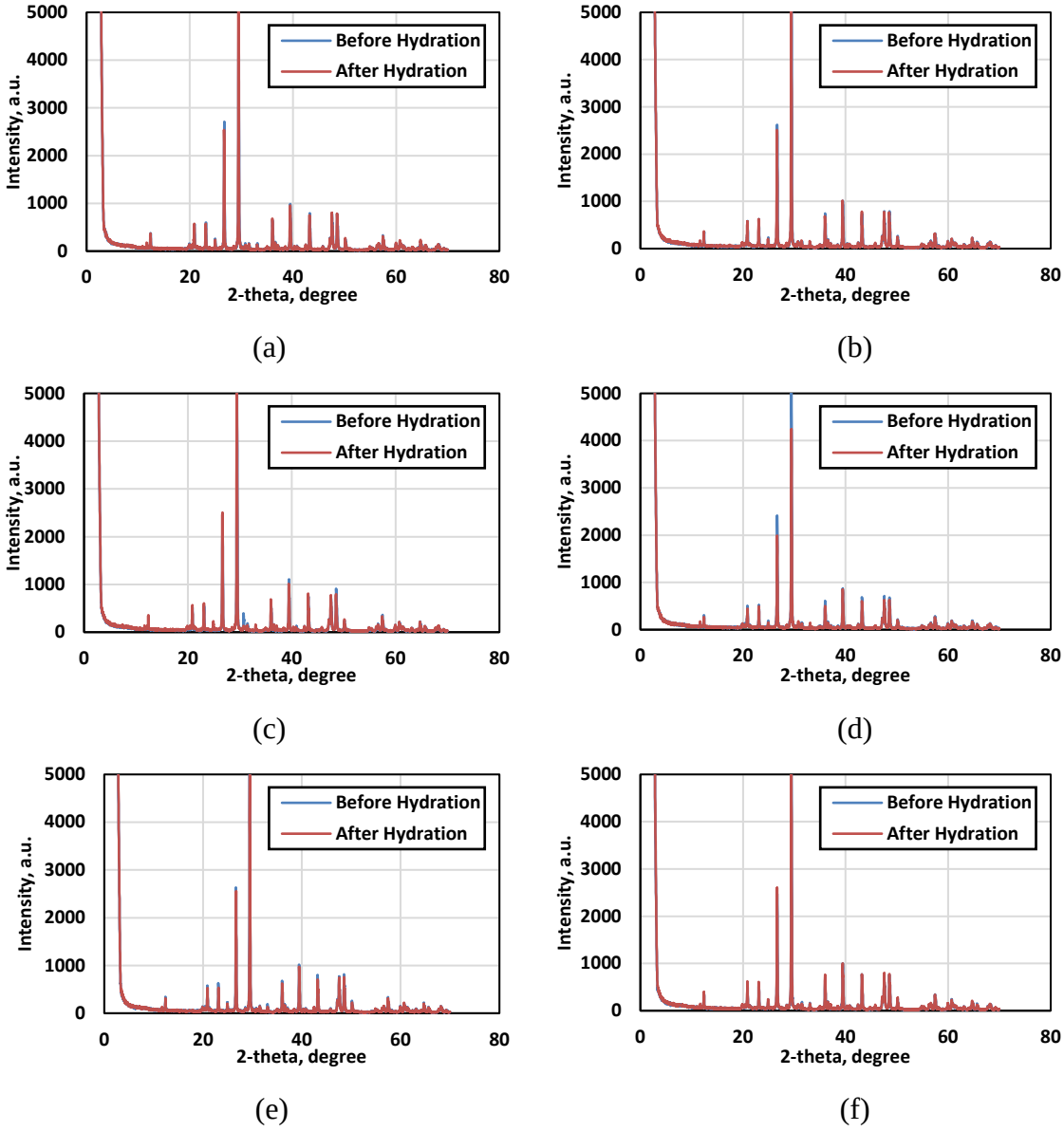

Fig. 6. 15 Organic-rich mudrock formation M1: XRD analysis on rock samples (a) M1.1, (b) M1.2, (c) M1.3, (d) M1.4, (e) M1.5, and (f) M1.6.

6.3.2.1.3 Nitrogen Adsorption-Desorption Measurements

Fig. 6.16 shows nitrogen adsorption-desorption isotherms of organic-rich mudrock samples M1.1, M1.2, M1.3, M1.4, M1.5, and M1.6. Based on the measured nitrogen adsorption-desorption isotherms, the BET surface areas of organic-rich

mudrock samples M1.1, M1.2, M1.3, M1.4, M1.5, and M1.6 were estimated to be 4.110, 4.024, 3.467, 3.867, 4.202, and 4.106 m²/g, respectively. After applying the inversion algorithm with the inputs of mineral composition from QXRD, the surface areas of quartz, feldspar, calcite, illite, kaolinite, and chlorite in the mudrock samples were estimated to be 0.409, 0.533, 3.260, 19.800, 11.653, and 10.302 m²/g, respectively.

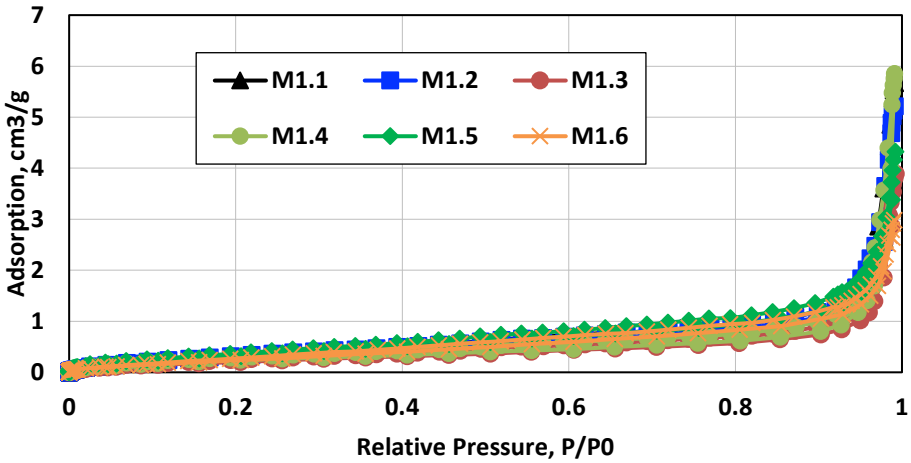

Fig. 6. 16 Nitrogen adsorption-desorption isotherms of organic-rich mudrock samples M1.1, M1.2, M1.3, M1.4, M1.5, and M1.6.

6.3.2.1.4 NMR Measurements

Figs. 6.17a–f show the NMR T_2 distributions of hydration water in samples M1.1–M1.6, respectively. The volumes of hydration water in M1.1–M1.6 were quantified to be 0.629, 0.618, 0.333, 0.5512, 0.672, and 0.658 mL/100g, respectively. Based on **Eq. 6.15** and mineral composition from QXRD, the volume of hydration water from illite, kaolinite, and chlorite were estimated to be 9.968, 2.985, and 3.047 mL/100g, respectively.

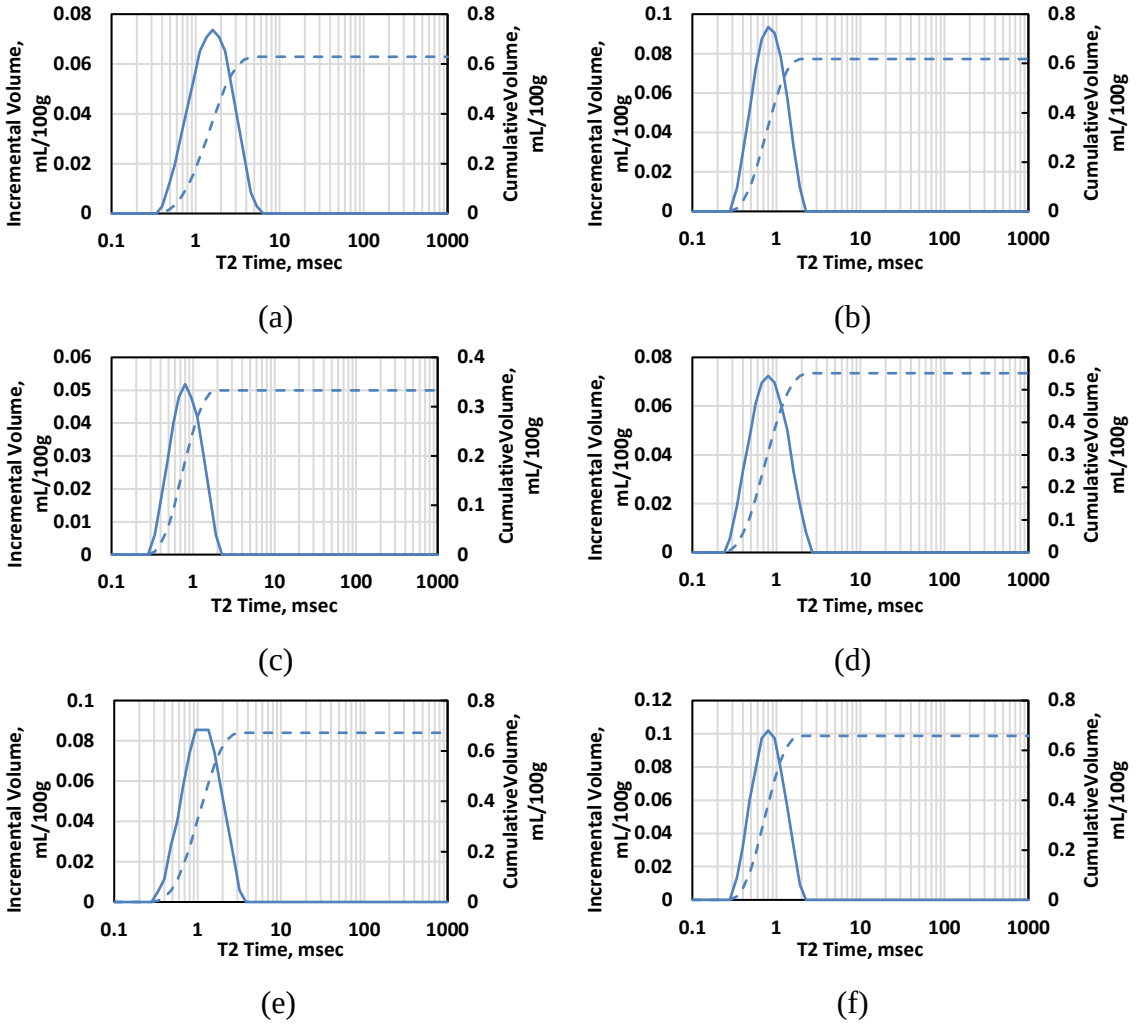

Fig. 6. 17 Hydration water quantification in organic-rich mudrock formation M1: NMR T_2 distribution in samples (a) M1.1, (b) M1.2, (c) M1.3, (d) M1.4, (e) M1.5, and (f) M1.6.

6.3.2.1.5 ICP-MS Measurements and CEC Quantification

Table 6.10 lists the results of measured CEC for four types of cations and the total CEC in six samples M1.1–M1.6 based on wet chemistry method and ICP-MS measurements. The concentrations of four types of exchangeable cations (i.e., Na^+, Mg^{2+}, K^+, and Ca^{2+}) from ICP-MS measurements were used for calculating CEC of those

cations for each mudrock samples based on **Eqs 6.1–6.4**. The total CEC of mudrock sample is calculated using **Eq. 6.5**.

CEC	M1.1	M1.2	M1.3	M1.4	M1.5	M1.6
Na^+	0.42	0.2	0	0.02	0.19	0.42
Mg^{2+}	1.55	2.32	1.88	1.59	1.52	1.55
K^+	0.9	1	1.05	1.48	1.23	0.9
Ca^{2+}	0.32	0.37	0.22	0.26	0.47	0.32
CEC, total	3.19	3.89	3.16	3.35	3.4	3.19

Table 6. 10 The CEC for Na^+, Mg^{2+}, K^+, and Ca^{2+}, and the total measured CEC in six samples M1.1–M1.6 (meq/100g) using ICP-MS measurements.

6.3.2.1.6 CEC Assessment Using Membrane Potential Method

Table 6.11 lists the results of measured CEC in six samples M1.1–M1.6 based on the membrane potential method. Porosity of the six samples M1.1–M1.6 is quantified by NMR T_2 measurements. Q_v is calculated based on **Eq 6.8**. The CEC of six samples is calculated using **Eq. 6.9**. The results of CEC estimates from the membrane potential method are used for verification of those obtained from the new method.

6.3.2.1.7 CEC Assessment Using the Introduced Method

The volume of hydration water from NMR measurements as well as the basal spacing, the number of layers, and the effective surface area were used as inputs to the CEC estimation model presented in **Eq. 6.12**. **Table 6.12** lists the volume of hydration water, the basal spacing, the average number of layers, the thickness of hydration water at clay surface, the effective surface area, the estimates of CEC using the new method for three of the clay minerals (i.e., illite, kaolinite, and chlorite) for the mudrock samples, and the range of CEC values of pure clay minerals reported in the previous

publications (Carroll, 1959; Ellis and Singer, 2007). It was observed that the estimates of CEC using the new method for all the three clay minerals fell within the upper and lower bounds of reported CEC values.

Samples	NMR Porosity, %	Voltage, mV	Q_v, meq/cc	CEC, meq/100g
M1.1	5.61 ± 0.01	82.9 ± 0.2	0.84 – 0.86	1.83 ± 0.02
M1.2	4.80 ± 0.03	82.3 ± 0.1	0.82 – 0.83	1.52 ± 0.01
M1.3	5.91 ± 0.07	71.8 ± 0.3	0.44 – 0.47	1.03 ± 0.03
M1.4	3.95 ± 0.04	87.1 ± 0.2	1.06 – 1.08	1.62 ± 0.02
M1.5	5.13 ± 0.01	84.2 ± 0.1	0.91 – 0.92	1.81 ± 0.01
M1.6	4.98 ± 0.03	84.2 ± 0.2	0.90 – 0.92	1.69 ± 0.02

Table 6. 11 Organic-rich mudrock formation M1: NMR porosity, voltage between Ag/AgCl electrodes, Q_v, and CEC in six samples M1.1–M1.6 (meq/100g) using membrane potential method.

Clay	V_{HW}	d	D_s	S	**CEC, estimated**	**Range of CEC, reported**
Illite	9.968	-	50.3	19.800	17.95	10 – 40
Kaolinite	2.985	7.15	25.6	11.653	11.17	3 – 15
Chlorite	3.047	-	29.6	10.302	9.72	1 – 40

Table 6. 12 Organic-rich mudrock formation M1: Estimates of volume of hydration water (V_{HW}, mL/100g), basal spacing (d, Å), thickness of hydration water at surface (D_s, Å), effective surface area (S, $m^2 \cdot g^{-1}$), and CEC from the new method (meq/100g) as well as the range of CEC values from publications for the three dominant clay minerals.

6.3.2.1.8 Comparison of CEC Estimates between Different Method

Since the CEC of the three clay minerals (i.e., illite, kaolinite, and chlorite) within the mudrock samples have been quantified, the CEC of mudrock samples can be estimated based on **Eq. 6.19**. The CEC values of clay minerals reported in the previous publications have upper and lower bounds, so the upper and lower bounds of CEC of mudrock samples can be estimated by use of **Eq. 6.19** with an input of mineral composition in each sample. **Table 6.13** summarizes the results of CEC estimates from

the new method, the wet chemistry method, the membrane potential method, and the upper and lower bounds calculated from the previously documented CEC data. **Fig. 6.18** compares the CEC estimates obtained from the proposed method against those from the membrane potential method. The results indicated that the estimated CEC values from the new method agreed with those from the membrane potential method. **Fig. 6.19** compares the CEC estimates based on the new method, the wet chemistry method, the membrane potential method and upper and lower bounds of CEC estimates from the previously documented CEC data. The results indicated that the calculated CEC estimates using the new method and the membrane potential method fell within the upper and lower bounds of CEC. However, the CEC measured by wet chemistry method was beyond the upper bound of CEC. The overestimation of CEC from wet chemistry method was mainly caused by the existence of salt precipitant in pore space of the mudrock. During the ammonium acetate extraction, the cations from salt precipitant were also moved to the cation solution for ICP-MS measurements. All comparisons indicated the reliability of the new method for CEC assessment.

Different Methods	**M1.1**	**M1.2**	**M1.3**	**M1.4**	**M1.5**	**M1.6**
CEC, new method	1.82	1.71	0.91	1.54	1.90	1.77
CEC, wet chemistry	3.19	3.89	3.16	3.35	3.40	3.19
CEC, membrane potential	1.83 ± 0.02	1.52 ± 0.01	1.03 ± 0.03	1.62 ± 0.02	1.81 ± 0.01	1.69 ± 0.02
CEC, reported data	0.60 – 3.12	0.59 – 2.98	0.32 – 1.63	0.53 – 2.67	0.63 – 3.37	0.63 – 3.16

Table 6. 13 Organic-rich mudrock formation M1: CEC estimates (meq/100g) based on the new method, the wet chemistry method, and membrane potential method as well as the upper and lower bounds for CEC, calculated from the previously documented CEC data for pure clay minerals.

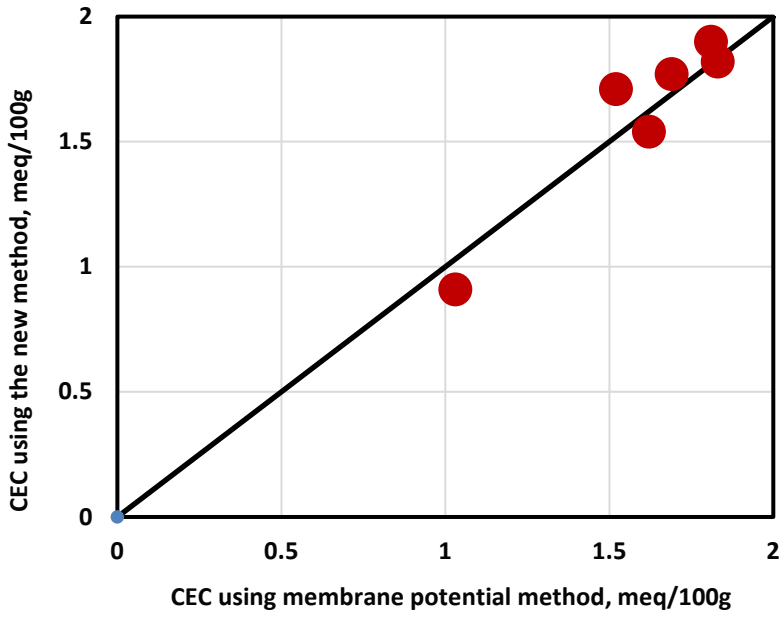

Fig. 6. 18 Organic-rich mudrock formation M1: Comparison of the estimates of CEC from the new method against those from the membrane potential method.

6.3.2.1.9 Influence on Assessment on Water Saturation

I created a synthetic example to investigate the influence of CEC estimates from different method on assessment of water saturation. The water saturation of the formation with multiple types of clay minerals can be estimate by use of Waxman-Smith equation (Waxman and Smits, 1968), given by

$$\frac{1}{R_t} = \frac{S_w^m \phi^n}{a}\left(\frac{1}{R_w} + \frac{B_e Q_v}{S_w}\right), \tag{6.20}$$

where R_t is resistivity of formation, R_w is the resistivity of brine, m, n, and a are constant, B is equivalent conductance of clay cation.

Based on actual field data, I assume that R_t is equal to 100 ohm·m at 200 °F, R_w is equal to 0.05 ohm·m at 75 °F, ϕ is determined by NMR T_2 measurements, m is equal to 2, n is equal to 2, a is equal to 1, B is equal to 3.5 $(ohm \cdot m \cdot meq)^{-1} \cdot cc$.

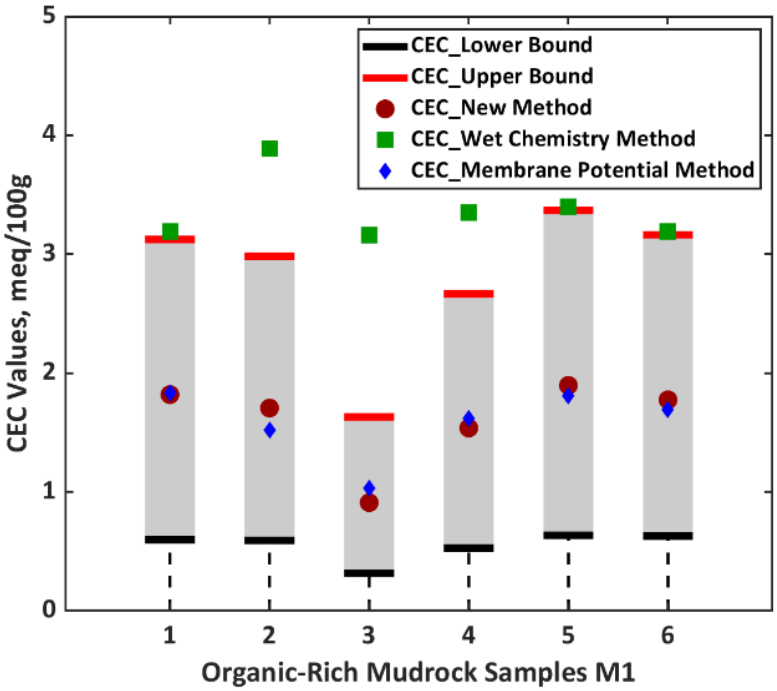

Fig. 6. 19 Organic-rich mudrock formation M1: Comparison of the CEC estimates from the new method, the wet chemistry method, and upper and lower bounds of CEC estimates calculated from the previously documented CEC data.

Table 6.14 summarizes the results of water saturation based on CEC estimates from the new method, the wet chemistry method, and the previously documented CEC data. **Fig. 6.20** compares the water saturation estimates based on different method. The results showed a significant uncertainty of water saturation using the CEC estimates from previously documented data. The estimate of water saturation from the new method fell within the range of reported data, but water saturation was underestimated when CEC estimates from the wet chemistry method was used. The comparison further

indicated that the new method for CEC quantification can be considered more reliable for assessment of water saturation.

Different Methods	M1.1	M1.2	M1.3	M1.4	M1.5	M1.6
S_w, new method	0.065	0.060	0.127	0.054	0.058	0.059
S_w , wet chemistry	0.037	0.026	0.040	0.025	0.033	0.033
S_w , membrane potential	0.064	0.066	0.11	0.051	0.060	0.062
S_w , reported data	0.037 – 0.172	0.026 – 0.154	0.040 – 0.262	0.025 – 0.144	0.033 – 0.155	0.033 – 0.151

Table 6. 14 Organic-rich mudrock formation M1: Water saturation estimates based on CEC estimates from the new method, the wet chemistry method, the membrane potential method, and previously documented data.

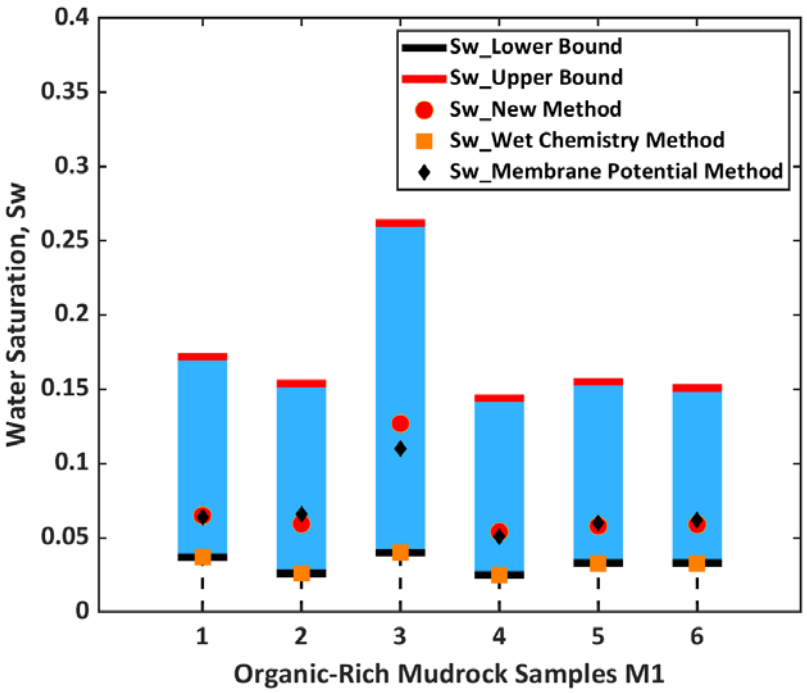

Fig. 6. 20 Organic-rich mudrock formation M1: Assessment of water saturation from the new method, the wet chemistry method, the membrane potential method, and the previously documented CEC data.

6.3.2.2 Formation M2

6.3.2.2.1 XRD Analysis

The XRD measurements in the organic-rich mudrock samples M2.1, M2.2, M2.3, M2.4, M2.5, and M2.6 before (blue line) and after (red line) hydration are show in **Figs. 6.21a–f**, respectively. The reflection index (d001), which represents the basal space of montmorillonite and illite, was observed at 2-theta of 8.851˚. The overlap of the reflection index (d001) of Mt and illite, indicates that the basal spacing of Mt and illite are equal. Based on Bragg's Law, the basal spacing of illite and Mt was calculated to be 9.99 Å. The shift of reflection for basal spacing before and after hydration was not observed, indicating the absence of swelling phenomenon. It also implied the concentration of swelling clay minerals, such as Mt, might be low in these rock samples. Reflection index of kaolinite and chlorite was not observed either, indicating low concentration of kaolinite and chlorite.

6.3.2.2.2 Mineralogy and TOC Analysis

Table 6.15 summarizes weight concentrations of dominant minerals and TOC in the six rock samples M2.1–M2.6, obtained from quantitative XRD analysis and pyrolysis. The dominant clay types were illite and chlorite. The results showed low contents of montmorillonite and kaolinite in the rock samples. Hence, the contributions of CEC from montmorillonite and kaolinite were assumed to be negligible and were not considered for estimating CEC of the rock samples. TOC of the mudrock samples M2.1–M2.6 were in range of 1.0wt% to 3.3wt%.

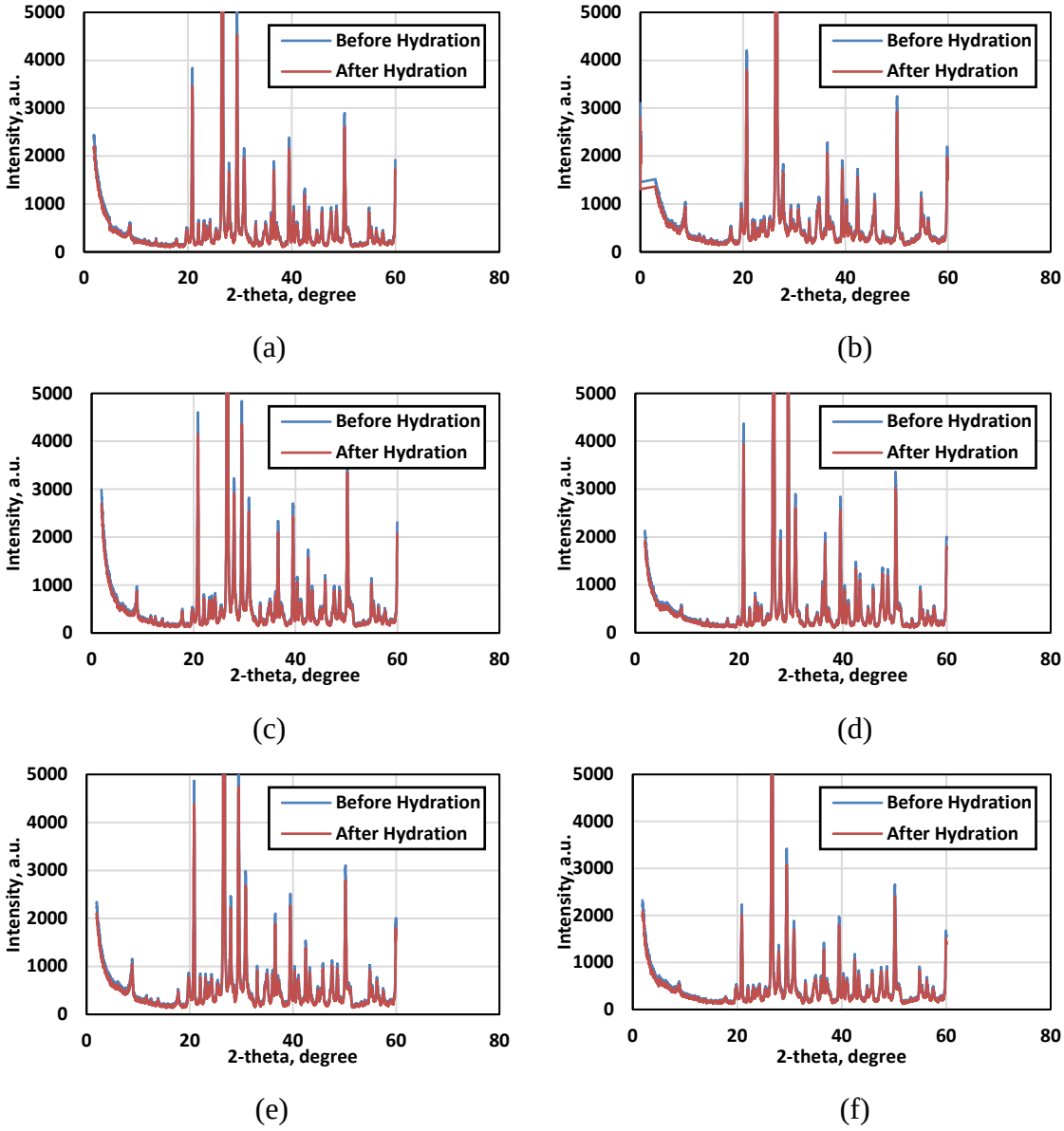

Fig. 6. 21 Organic-rich mudrock formation M2: XRD analysis on rock samples (a) M2.1, (b) M2.2, (c) M2.3, (d) M2.4, (e) M2.5, and (f) M2.6.

6.3.2.2.3 Nitrogen Adsorption-Desorption Measurements

Fig. 6.22 shows nitrogen adsorption-desorption isotherms of organic-rich mudrock samples M2.1, M2.2, M2.3, M2.4, M2.5, and M2.6. Based on the measured nitrogen adsorption-desorption isotherms, the BET surface areas of sample M2.1, M2.2,

M2.3, M2.4, M2.5, and M2.6 were estimated to be 4.774, 9.091, 4.784, 2.967, 6.510, 4.845 m^2/g, respectively. After applying the inversion algorithm with the inputs of mineral composition from QXRD, the surface areas of quartz, feldspar, plagioclase, calcite, illite, and chlorite in the mudrock samples were estimated to be 0.771, 0.850, 1.901, 0.972, 35.32, and 8.015 m^2/g, respectively.

Composition	M2.1 (wt%)	M2.2 (wt%)	M2.3 (wt%)	M2.4 (wt%)	M2.5 (wt%)	M2.6 (wt%)
Quartz	46.6	53.3	47.2	46.8	41.3	44.6
Feldspars	2.4	2.3	2.4	1.6	2.0	2.3
Plagioclase	9.8	8.1	12.4	8.5	9.6	9.8
Calcite	25.6	5.9	24.2	34.7	23.7	27.8
Mt	0.2	0.4	0.2	0.3	0.2	0.3
Illite	10.7	22.5	10.4	5.4	15.0	10.8
Kaolinite	0.1	0.1	0.2	0.0	0.1	0.2
Chlorite	1.7	4.4	2.1	1.0	4.8	1.1
TOC	2.89	3.01	1.01	1.73	3.21	3.15

Table 6. 15 The weight concentrations of dominant minerals in the mudrock samples M2.1–M2.6, obtained from QXRD analysis.

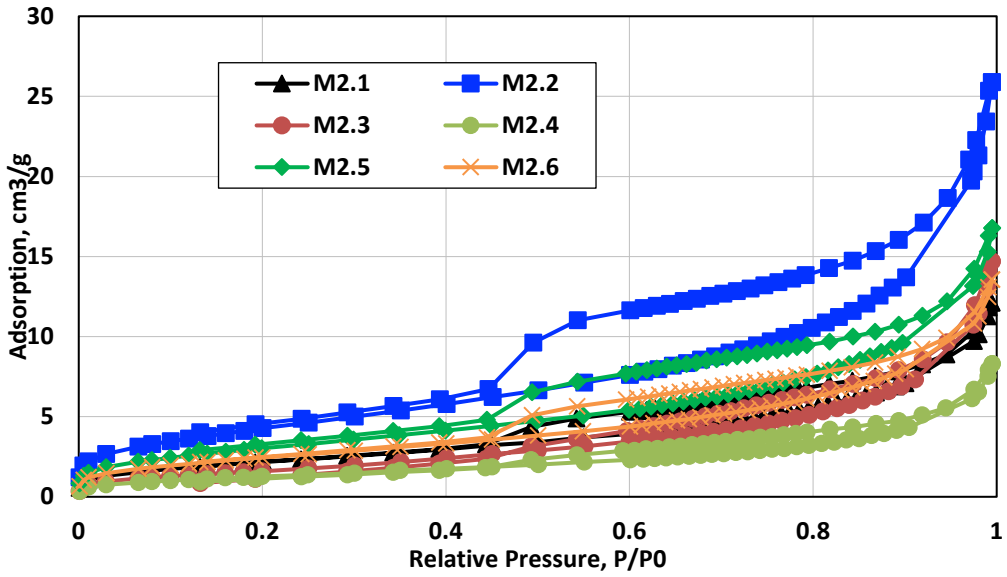

Fig. 6. 22 Nitrogen adsorption-desorption isotherms of organic-rich mudrock samples M2.1, M2.2, M2.3, M2.4, M2.5, and M2.6.

6.3.2.2.4 NMR Measurements

Figs. 6.23a–f show the NMR T_2 distributions of hydration water in samples M2.1–M2.6, respectively. The volumes of hydration water in M2.1–M2.6 were quantified to be 1.33, 2.84, 1.32, 0.70, 1.92, and 1.36 mL/100g, respectively. Based on **Eq. 6.15** (inversion algorithm) and mineral composition from QXRD, the volume of hydration water from illite and chlorite were estimated to be 12.17 and 1.61 mL/100g, respectively.

6.3.2.2.5 ICP-MS Measurements and CEC Quantification

Table 6.16 lists the results of measured CEC for four types of cations and the total CEC in six samples M2.1–M2.6 based on wet chemistry method and ICP-MS measurements. The concentrations of four types of exchangeable cations (i.e., Na^+, $Mg^{2+,}$ K^+, and Ca^{2+}) from ICP-MS measurements were used for calculating CEC of those cations for each mudrock samples based on **Eqs 6.1–6.4**. The total CEC of mudrock sample is calculated using **Eq. 6.5**.

CEC	**M2.1**	**M2.2**	**M2.3**	**M2.4**	**M2.5**	**M2.6**
Na^+	5.03	5.88	4.32	3.18	4.62	4.56
Mg^{2+}	1.30	1.69	2.11	1.09	2.31	1.74
K^+	0.66	0.87	1.26	0.63	0.96	1.00
Ca^{2+}	0.36	0.65	0.35	0.15	0.97	0.75
CEC, total	7.35	9.09	8.04	5.05	8.86	8.05

Table 6. 16 The CEC for Na^+, Mg^{2+}, K^+, and Ca^{2+}, and the total measured CEC in six samples M2.1–M2.6 (meq/100g) using ICP-MS measurements.

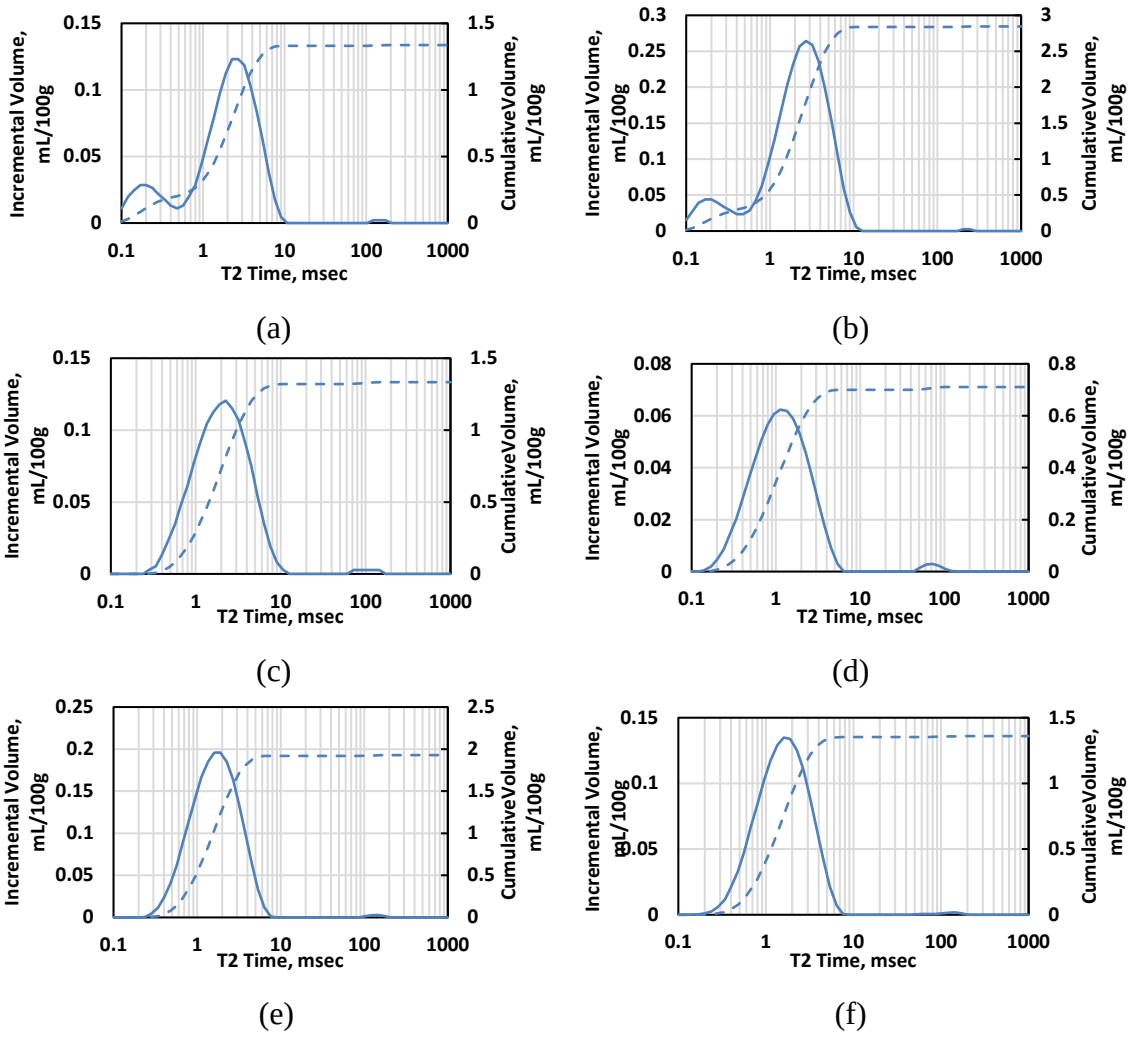

Fig. 6. 23 Hydration water quantification in organic-rich mudrock formation M2: NMR T_2 distribution in samples (a) M2.1, (b) M2.2, (c) M2.3, (d) M2.4, (e) M2.5, and (f) M2.6.

6.3.2.2.6 CEC Assessment Using the Membrane Potential Method

Table 6.17 lists the results of measured CEC in six samples M2.1–M2.6 based on membrane potential method. Porosity of the six samples M2.1–M2.6 is quantified by NMR T_2 measurements. Q_v is calculated based on **Eq 6.8**. The CEC of six samples is

calculated using **Eq. 6.9**. The results of CEC estimates from the membrane potential method are used for verification of those obtained from the new method.

Samples	NMR Porosity, %	Voltage, mV	Q_v, meq/cc	CEC, meq/100g
M2.1	7.07 ± 0.03	90.5 ± 0.2	1.28 – 1.31	3.55 ± 0.05
M2.2	7.78 ± 0.01	101.2 ± 0.2	2.39 – 2.45	7.24 ± 0.10
M2.3	6.82 ± 0.03	92.8 ± 0.2	1.45 – 1.48	3.83 ± 0.05
M2.4	6.24 ± 0.02	91.8 ± 0.1	1.39 – 1.40	2.35 ± 0.02
M2.5	7.43 ± 0.04	95.8 ± 0.1	1.73 – 1.76	5.01 ± 0.04
M2.6	6.96 ± 0.03	89.5 ± 0.3	1.20 – 1.24	3.26 ± 0.06

Table 6. 17 Organic-rich mudrock formation M1: NMR porosity, voltage between Ag/AgCl electrodes, Q_v, and CEC in six samples M2.1–M2.6 (meq/100g) using membrane potential method.

6.3.2.2.7 CEC Assessment Using the Introduced Method

The volume of hydration water from NMR measurements as well as the basal spacing, the number of layers, and the effective surface area were used as inputs to the CEC estimation model presented in **Eq. 6.12**. **Table 6.18** lists the volume of hydration water, the basal spacing, the average number of layers, the thickness of hydration water at clay surface, the effective surface area, the estimates of CEC using the new method for the mudrock samples, and the range of CEC values of pure clay minerals reported in the previous publications. It was also observed that the estimates of CEC using the new method for clay minerals fell within the upper and lower bounds of reported CEC values.

Clay	V_{HW}	d	D_s	S	**CEC, estimated**	**Range of CEC, reported**
Illite	12.17	9.99	34.5	35.32	32.87	10 – 40
Chlorite	1.61	-	20.1	8.015	7.96	1 – 40

Table 6. 18 Organic-rich mudrock formation M2: Estimates of volume of hydration water (V_{HW}, mL/100g), basal spacing (d, Å), thickness of hydration water at surface (D_s, Å), effective surface area (S, $m^2 \cdot g^{-1}$), and CEC from the new method (meq/100g) as well as the range of CEC values from publications for the three dominant clay minerals.

6.3.2.2.8 Comparison of CEC Estimates between Different Method

Table 6.19 summarizes the results of CEC estimates from the new method, the wet chemistry method, and the upper and lower bounds calculated from the previously documented CEC data. **Fig. 6.24** compares the CEC estimates obtained from the proposed method against those from the membrane potential method. The results indicated that the estimated CEC values from the new method agreed with those from the membrane potential method. **Fig. 6.25** compares the CEC estimates based on the new method, the wet chemistry method, the membrane potential method, and upper and lower bounds of CEC estimates from the previously documented CEC data. The results indicated that the calculated CEC estimates using the new method fell within the upper and lower bounds of CEC. However, the CEC measured by the wet chemistry method was beyond the upper bound of CEC. The overestimation of CEC from wet chemistry method was mainly caused by the existence of salt precipitant in pore space of the mudrock samples. During the ammonium acetate extraction, the cations from salt precipitant were also moved to the cation solution for ICP-MS measurements. All comparisons indicated the reliability of the new method for CEC assessment.

6.3.2.2.9 Influence on Assessment on Water Saturation

Similarly, water saturation can be estimated for formation M2 based on **Eq. 6.20**. **Table 6.20** summarizes the results of water saturation based on CEC estimates from the new method, the wet chemistry method, and the previously documented CEC data. **Fig.**

6.26 compares the water saturation estimates based on different method. The results showed a significant uncertainty of water saturation using the CEC estimates from previously documented data. The estimate of water saturation from the new method fell within the range of reported data.

Different Methods	M2.1	M2.2	M2.3	M2.4	M2.5	M2.6
CEC, new method	3.73	7.79	3.67	1.95	5.39	3.75
CEC, wet chemistry	7.35	9.09	8.04	5.05	8.86	8.05
CEC, membrane potential	3.55 ± 0.05	7.24 ± 0.10	3.83 ± 0.05	2.35 ± 0.02	5.01 ± 0.04	3.26 ± 0.06
CEC, reported data	1.11 – 5.08	2.31– 10.8	1.08 – 5.16	0.58 – 2.68	1.57 – 8.04	1.12 – 4.96

Table 6. 19 Organic-rich mudrock formation M2: CEC estimates (meq/100g) based on the new method, the wet chemistry method, and the membrane potential method, as well as the upper and lower bounds for CEC, calculated from the previously documented CEC data for pure clay minerals.

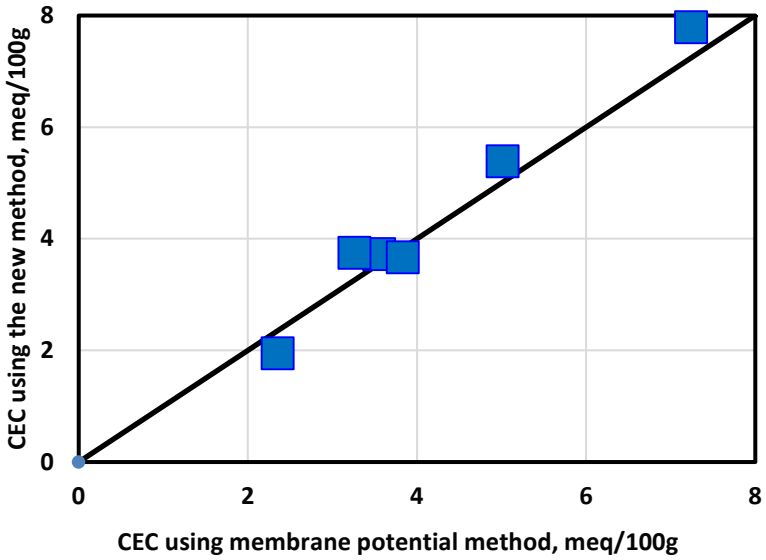

Fig. 6. 24 Organic-rich mudrock formation M2: Comparison of the estimates of CEC from the new method against those from the membrane potential method.

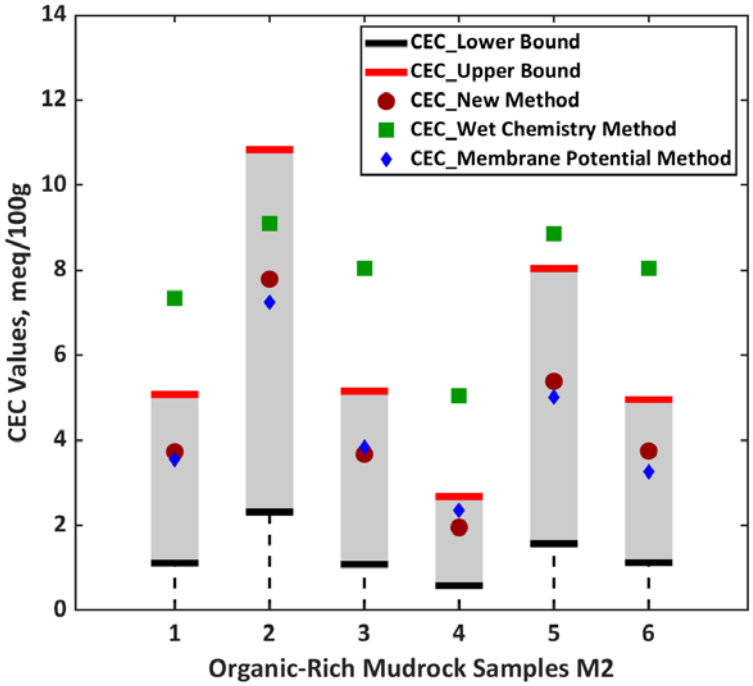

Fig. 6. 25 Organic-rich mudrock formation M2: Comparison of the CEC estimates from the new method, the wet chemistry method, the membrane potential method and upper and lower bounds of CEC estimates calculated from the previously documented CEC data.

Different Methods	**M2.1**	**M2.2**	**M2.3**	**M2.4**	**M2.5**	**M2.6**
S_w **, new method**	0.040	0.021	0.039	0.067	0.030	0.040
S_w **, wet chemistry**	0.021	0.018	0.018	0.026	0.018	0.019
S_w **, membrane potential**	0.042	0.023	0.038	0.056	0.032	0.046
S_w **, reported data**	0.030 – 0.126	0.015 – 0.071	0.028 – 0.124	0.049 – 0.189	0.020 – 0.098	0.030 – 0.124

Table 6. 20 Organic-rich mudrock formation M2: Water saturation estimates based on CEC estimates from the new method, the wet chemistry method, the membrane potential method and previously documented data.

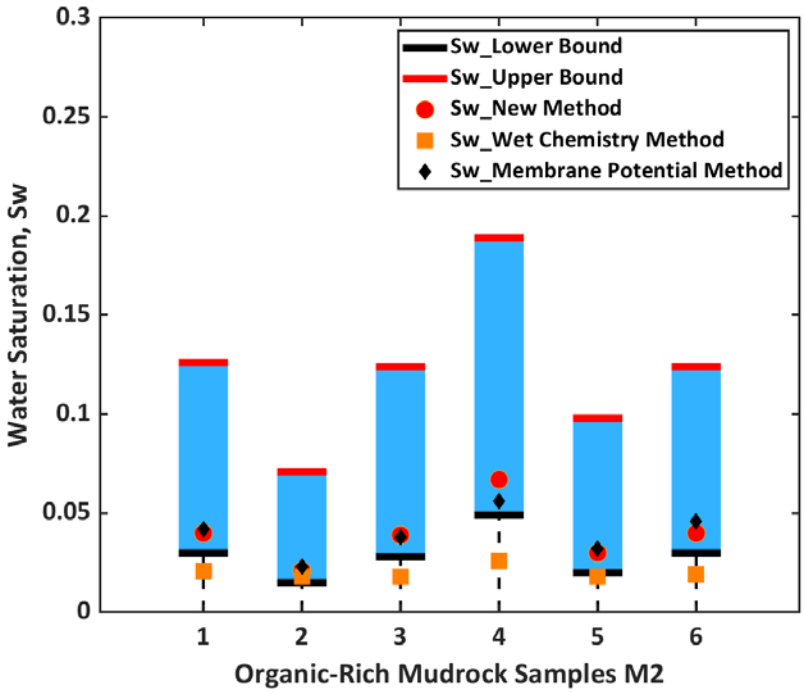

Fig. 6. 26 Organic-rich mudrock formation M2: Assessment of water saturation from the new method, the wet chemistry method, the membrane potential method, and the previously documented CEC data.

6.4 Conclusions

I introduced a new workflow for CEC assessment in rocks with complex mineralogy and presence of multiple types of clay minerals by integrating analysis of data collected from XRD, QXRD, NMR, pyrolysis, and nitrogen adsorption-desorption isotherm measurements. In the case of synthetic shaly sand samples, direct measurements of CEC based on ammonium acetate method and ICP-MS measurements were used as ground truth for cross-validation of the results obtained from the new method. In the case of actual shaly sand samples, estimates of CEC from ammonium acetate method and ICP-MS measurements were corrected for the influence of salt

precipitant in pore space and then used for cross-validation of the results obtained from the new method. In the case of organic-rich mudrock samples, CEC estimates from the new method were compared against the wet chemistry method, the membrane potential method, and previously documented CEC data were

The CEC values of synthetic shaly sand samples, estimated using the new method, agreed with direct measurements with difference of less than 3 meq/100g. The CEC values of actual shaly sand samples, containing three types of clay minerals, were also in good agreement with direct measurements (after correction for the salt precipitation effect) with difference of less than 4 meq/100g. The CEC values of organic-rich mudrock samples were in range of the previously documented data, but CEC values from the wet chemistry method were overestimated. The CEC values of organic-rich mudrock samples also agreed with those from the membrane potential method. Results confirmed that the introduced new method can be used for estimating CEC in rocks with complex minerology and various type of formations. The assessment of water saturation based on CEC estimates from different method showed that there would be 5 – 20% uncertainty when using previously documented CEC data. The new method can significantly enhance the water saturation assessment.

The introduced method can be considered more convenient for the industrial purposes compared to the wet chemistry method. The reasons include (a) wet chemistry method will cause overestimate of CEC due to the existence of salt precipitant in pore space and (b) the accuracy of wet chemistry method significantly relies on every step of the procedure, such as deionized water preparation, particle size, and pH. The new

method, however, can overcome the existence of salt precipitation. The reliability of the method can also be improved with increase in accuracy of mineral composition results. Moreover, the introduced method can be applied for any given formation, while the multiple salinity method is limited to highly-permeable formations and requires intact core plugs. The membrane potential method requires special equipment and relies on the empirical correlations, while this method is analytically established on the physics-based correlations among CEC, volume of hydration water, and structure of clay minerals. The outcomes of this research imply the feasibility of applying the new method for CEC assessment in any rock physics laboratory with as access to XRD, NMR, and nitrogen adsorption-desorption equipment. The outcomes of this research can be applied to variety of formations with complex lithology.

CHAPTER VII

CONCLUSIONS AND FUTURE RESEARCH RECOMMENDATIONS

This chapter summarizes the main contributions of the research conducted in this dissertation. Main conclusions are reiterated, and recommendations for future research are provided.

7.1 Summary, Conclusions, and Contributions

This section details the summary, conclusions, and contributions based on the results reported in the dissertation. It is divided into subsections including improved NMR-based pore-network connectivity assessment, enhanced NMR-based permeability assessment, impact of relative humidity on reliability of core measurements, and quantification of CEC using integrated interpretation of NMR, XRD, pyrolysis, and nitrogen adsorption-desorption measurements.

7.1.1 Nanoparticles as NMR Contrast Agents for Pore-Network Connectivity Assessment

In Chapter II, I proposed the use of magnetic nanoparticles as NMR contrast agents for improved characterization of pore-size distribution, interconnected porosity, and fracture network in rocks. I showed the successful application of the proposed method for distinguishing isolated from connected pore/fracture network in rocks with

complex pore structure. The following are summaries and main conclusions of my research in the aforementioned category:

1. The relaxation of proton spins was significantly accelerated with the presence of SPIONs, causing a remarkable shift in T_2 relaxation times to short relaxation times;
2. The large pores of sandstone rock samples were easily invaded by SPIONs;
3. Only the connected fractures of organic-rich mudrocks were invaded by SPIONs because the size of the SPIONs was larger than the pore-throat size of organic-rich mudrocks;
4. The results of NMR T_2 measurements before and after injection of magnetic nanoparticles were used to characterize interconnected pores.

The main contributions of the research can be summarized as follows:

1. This is the first time that nanoparticles have been utilized to improve NMR core measurements, including characterization of pore-size distribution and pore connectivity in heterogeneous rock samples;
2. It is promising for improved and real-time NMR-based permeability assessment in formations with complex pore structure through reliable characterization of pore structure;

7.1.2 Manganese-Bearing Solution as an NMR Contrast Agent for Enhanced Permeability Assessment

In Chapter III, I switched to using a manganese-bearing solution as an NMR contrast agent for assessing pore connectivity in carbonate formations due to

electrostatic attraction between the carbonate surface and SPIONs, which caused aggregation of SPIONs on the carbonate surface. This method successfully distinguished isolated pores from interconnected pores. This enhanced characterization of pore-network connectivity improved the reliability of NMR-based permeability assessment. The following are summaries and main conclusions of my research in the aforementioned category:

1. The interconnected pores of carbonate formations were invaded by the manganese-bearing solution using coreflood experiments;
2. The results of NMR T_2 measurements before and after injection of contrast agents were used to distinguish isolated pores from interconnected pores;
3. After correcting T_2 distribution for the impact of isolated pores, NMR-based permeability estimates were improved significantly. The relative error in permeability estimates (compared to permeability corrected for Klinkenberg effect) decreased from 500% to less than 10% for the SDR model and from 79.7% to 4.0% for the Coates models.

The main contributions of the introduced method can be summarized as follows:

1. This method enhances NMR-based permeability assessment in carbonate formations in the presence of isolated pores;
2. This method will not damage the formation and can be used as a supplemental technique for the existing NMR log-inject-log method;

3. This method can be used for permeability assessment in field applications, but the mercury injection capillary pressure (MICP) method is limited to the laboratory applications.

7.1.3 Impact of Relative Humidity on Hydration of Clay Minerals

In Chapter IV, I quantified the influence of relative humidity on the hydration of clay minerals using laboratory NMR and TGA measurements. The following are summaries and main conclusions of my research in the aforementioned category:

1. The volumes of interlayer water and hydration water were quantified by TGA and NMR measurements;
2. The water accumulation on the clay minerals (i.e., hydration of clay minerals) at different relative humidity levels was quantified by NMR measurements;
3. Approximately 20 mL/100 g variations in volume of hydration in montmorillonite was caused by variation of relative humidity level in the range of 0% to 95%, implying significant influence of clay hydration on assessment of water content in clay-rich formations;
4. More than 250% of fluid content in organic-rich mudrocks was observed when relative humidity changed from 0% to 95%;
5. A strong relationship was detected between volume of hydration water and CEC of clay minerals.

The main contributions of the research can be summarized as follows:

1. This study systematically investigated the influence of relative humidity on assessment of NMR-based porosity (fluid volume) and shows that NMR-based porosity evaluation is sensitive to the concentration of clay minerals and humidity level in the laboratory environment;
2. Corrections for the impact of humidity might be required, depending on the type and concentration of clay minerals in rocks, as well as the level of humidity.

7.1.4 Quantification of CEC

In Chapters V and VI, I established an analytical correction between the volume of hydration water and the CEC of clay minerals and developed a new method for quantifying CEC of pure clay minerals and rocks with multiple types of clay minerals. The following are summaries and main conclusions of my research in the aforementioned category:

The energy balance between chemical potential and electric potential energy was used to derive an analytical correlation between the volume of hydration water and the CEC of pure clay minerals;

1. The properties of clay minerals characterized from XRD, quantitative XRD, NMR, pyrolysis, and N_2 adsorption-desorption measurements were used as inputs for the new method;
2. For the case of pure clay minerals, the CEC estimates from the new method agreed well with those obtained from the wet chemistry method, with a difference of less than 7 meq/100 g;

3. For the case of shaly sand samples, the CEC estimates from the new method agreed well with those obtained from the wet chemistry method, with a difference of less than 4 meq/100 g;
4. For the case of organic-rich mudrock samples, CEC estimates were in the range of the literature-documented data, but those from the wet chemistry method were overestimated due to the existence of salt precipitants in the pore space;
5. For the case of organic-rich mudrock samples, CEC estimates from the new method agreed with those from the membrane potential method, which further verified the reliability of the new method.

The main contributions of the research can be summarized as follows:

1. The introduced method potentially can be considered more convenient and reliable for industrial purposes as compared to other methods:
    a. Compared against the wet chemistry method, the new method overcomes the uncertainty caused by salt precipitants;
    b. Compared against the multiple salinity method, the new method can be more applicable for various types of formation, including tight formations;
    c. Compared against the membrane potential method, the new method is analytically established on physics-based correlations and is more accurate;
2. The introduced method can be applicable for CEC assessment in any rock physics laboratory with access to XRD, NMR, and nitrogen adsorption-desorption equipment;

3. The outcomes of this work can be applied to a variety of formations with complex lithology and can be an onsite supplement application for mud logging.

7.2 Future Research Recommendations

Although this dissertation focused on developing new techniques to solve the challenges associated with interpretation of NMR measurements for reliable formation evaluation, there remain many unsolved problems. The following is a list of possible future research that could expand the technical contributions of this dissertation:

1. Investigate the stability of nanoparticles at different salinity, pH, and other in-situ conditions, as well as the optimal size of nanoparticles to invade interconnected pore space in different formation types;
2. Test the method using NMR contrast agents on more cases of formations with complex pore structure and in the presence of non-connected or poorly connected pore network and correct T_2 distributions for the impact of isolated pores;
3. Apply the improved NMR-based permeability model to field data, in which manganese-ion-doped mud was used previously to characterize residual saturation;
4. Examine the possibility of altering the CEC value of the rocks when the rocks are crushed into powder for the purpose of uncertainty analysis for CEC estimates as well as achieving best practices for sample preparation;

5. Study the influence of facial direction of clay particles on the change in electric potential energy during the hydration process, and modify the energy balance between electric potential energy and chemical potential to improve the new method for CEC quantification;
6. Improve the efficiency of the hydration process in the introduced NMR-based CEC assessment method, which currently takes approximately 10 days in the laboratory;
7. Develop a workflow that incorporates NMR, XRD, N_2 adsorption-desorption techniques in the field, and provide an efficient and real-time technique for monitoring CEC at the rig site.

REFERENCES

Abragam, A., 1961. The principles of nuclear magnetism, *Oxford University Press*, New York, 324-325.

Al-Bazali, T.M., 2005. Experimental study of the membrane behavior of shale during interaction with water-based and oil-based muds, Ph.D. Dissertation, University of Texas at Austin, Austin, Texas.

Al-Shehri, A. A., Ellis, E. S., Servin, J. M., Kosynkin, D. V., Kanj, M. Y., and Schmidt, H. K., 2013. Illuminating the reservoir: magnetic nanomappers, SPE 164461, Proceedings of the SPE Middle East Oil and Gas Show and Exhibition: Society of Petroleum Engineers, Manama, Bahrain, March 10–13.

Anderson, R.L., Ratcliffe, I., Williams, P.A., Cliffe, S., and Coveney, P.V., 2010. Clay swelling – a challenge in the oilfield, *Earth Science Reviews*, 98, 201-216.

Barron, A. R., Tour, J. M., Busnaina, A. A., Jung, Y. J., Somu, S., Kani, M. Y., Potter, D., Resasco, D., and Ullo, J., 2010. Big things in small packages, *Oilfield review*, 22(3), 38-49.

Berend, I., Cases, J.M., Franqois, M., Uriot, J.P., Michot, L., Masion, A., and Thomas, F., 1995. Mechanism of adsorption and desorption of water vapor by homoionic montmorillonites: 2. the Li^+, Na^+, K^+, Rb^+, and Cs^+ -exchanged forms, *Clays and Clay Minerals*, 43(3), 324-336.

Bergaya, F. and Lagaly, G., 2006. Chapter 1 general introduction: clays, clay minerals, and clay science, *Developments in Clay Science*, 1, 1-18.

Bergaya, F., Lagaly, G., and Vayer, M., 2013. Cation and anion exchange, *Handbook of Clay Science*, 5, 333-359.

Boek, E.S. and Coveney, P.V., 1995. Molecular modeling of clay hydration: a study of hysteresis loops in the swelling curves of sodium montmorillonites, *Langmuir*, 11(12), 4629-4631.

Bonnemain, B., 1998. Superparamagnetic agents in magnetic resonance imaging: physicochemical characteristics and clinical applications — a review, *Journal of Drug Targeting*, 6 (3), 167–174.

Bragg, W.L., 1933. The crystalline state, vol. I, a general survey, London: Bell.

Bush, D.C. and Jenkins, R.E., 1977. CEC determinations by correlations with adsorbed water, SPWLA-1977-H, presented at SPWLA 18th Annual Logging Symposium, Houston, Texas, USA, June 5-8.

Carr, H.Y. and Purcell, E.M., 1954. Effects of diffusion on free precession in NMR experiments, *Physical Review*, 94(3), 630-638.

Carroll, D., 1959. Ion exchange in clays and other minerals, *Bulletin of the Geological Society of America*, 70, 749-780.

Cases, J.M., Berend, I., Besson, G., Franqois, M., Uriot, J.P., Thomas, F., and Poirier, J.E., 1992. Mechanism of adsorption-desorption of water vapor by homoionic montmorillonite. 1. the sodium exchanged form, *Langmiur*, 8(11), 2730-2739.

Cases, J.M., Berend, I., Franqois, M., Uriot, J.P., Michot, L.J., and Thomas, F., 1997. Mechanism of adsorption and desorption of water vapor by homoionic montmorillonite: 3. the Mg2+, Ca2+, Sr2+ and Ba2+ exchanged forms, *Clays and Clay Minerals*, 45(1), 8-22.

Chang, D., Vinegar, H., Morriss, C., and Straley, C., 1997. Effective porosity, producible fluid and permeability in carbonates from NMR logging, *The Log Analyst*, 38(2), 60-72.

Chapman, H.D., 1965. Methods of soil analysis – part 2 chemical and microbiological properties, *American Society of Agronomy*, 891-901.

Chen, S., Jacobi, D., Kwak, H., Altunbay, M., and Kloos, J., 2008. Pore-connectivity based permeability model for complex carbonate formations, presented at the SPWLA 49th Annual Logging Symposium. SPWLA-2008-E.

Cheng, K., Aderibigbe, A., Alfi, M., Heidari, Z., and Killough, J., 2014. Quantifying the impact of petrophysical properties on spatial distribution of contrasting nanoparticle agents in the near-wellbore region, *Petrophysics*, 55(5), 447-460.

Cheng, K. and Heidari, Z., 2015. Pore connectivity and permeability assessment in carbonate formations using NMR log-inject-log method, SPE-175066-MS, The Society of Petroleum Engineers (SPE) Annual Technical Conference and Exhibition Houston, Texas, USA, September 28–30.

Cheng, K. and Heidari, Z., 2017, Combined interpretation of NMR and TGA measurements to quantify the impact of relative humidity on hydration of clay minerals, *Applied Clay Science*, 143, 362-371.

Cheng, K. and Heidari, Z., 2018. A new method for quantifying cation exchange capacity in clay minerals, *Applied Clay Science*, 161, 444-455.

Cheng, K., Zhou, Y., Sun, Z., Hu, H., Zhong, H., Kong, X., and Chen, Q., 2012. Synthesis of carbon-coated, porous and water-dispersive Fe_3O_4 nanocapsules and their excellent performance for heavy metal removal applications, *Dalton Transactions*, 41(19), 5854–5861.

Chi, L., Cheng, K., and Heidari, Z., 2016. Improved assessment of interconnected porosity in multiple-porosity rocks by use of nanoparticle contrast agents and nuclear-magnetic-resonance relaxation measurements, *SPE Reservoir Evaluation & Engineering*, 19(1), 95-107.

Chitale, D.V., Gardner, J., and Signal, R., 2000. Significance of NMR T2 distribution from hydrated montmorillonites, SPWLA-2000-X, presented at SPWLA 41st Annual Logging Symposium, Dallas, Texas, USA, June 4-7.

Coates, G. R., Galford, J., Mardon, D., and Marschall, D., 1997. A new characterization of bulk-volume irreducible using magnetic resonance, presented at the SPWLA 38th Annual Logging Symposium, SPWLA-1997-QQ, also published in 1997 in *Dialog, London Petrophysical Society*, 5(6), 9-16.

Coates, G.R., Xiao, L., and Prammar, M.G., 1999. NMR logging principles and applications. Halliburton Energy Services, Houston.

Crowe, M.B., Jasek, D.E., Van Dalen, S.C., LaTorraca, G.A., Dunn, K.J., and Donovan, M.T., 1997. Measuring Residual Oil Saturation in West Texas Using NMR, presented at the SPWLA 38th Annual Logging Symposium, Houston, Texas, USA, June 15-18.

Doyle, C.D., 1961. Kinetic analysis of thermogravimetric data, *Journal of Applied Polymer Science*, 5(15), 285-292.

Ellis, D.W. and Singer, M.J., 2007. Well Logging for Earth Scientists: 2nd Edition, *Springer*, The Netherlands, 601.

Ferrage, E., Lanson, B., Sakharvo, B.A., and Drits, V.A., 2005. Investigation of smectite hydration properties by modeling experimental X-Ray diffraction patterns: part I. montmorillonite hydration properties, *American Mineralogist*, 90, 1358-1374.

Funk, J., Al-Khan, M., Eyvazzadeh, R., Dudenas, P., Jones, D., and Wilson, B., 2004. Revitalizing the use of sponge core for the determination of remaining oil saturations in carbonate reservoirs, presented at the Society of Core Analysts International Symposium, Abu Dhabi, UAE, October 5-9. SCA 2004-31.

Grim, R.E., 1962. Applied clay mineralogy, McGraw-Hill Book Co., Inc., New York.

Handwerger, D.A., Willberg, D.M., Pagels, M., Rowland, B., and Keller, J., 2012. Reconciling retort versus dean stark measurements on tight shales, SPE 159976, presented at SPE Annual Technology Conference and Exhibition, San Antonio, Texas, USA, October 8-10.

He, F., Zhang, M., Qian, T., and Zhao, D., 2009. Transport of carboxymethyl cellulose stabilized iron nanoparticles in porous media: Column experiments and modeling, *Journal of Colloid and Interface Science*, 334 (1), 96–102.

Horkowitz, J.P., Vinegar, H.J., Hartman, D.E., Coates, G.R., and Clerke, E.A., 1995. Residual oil saturation measurements in carbonates with pulsed NMR logs, presented at the SPWLA 37th Annual Logging Symposium, Paris, France, June 26-29.

Job, G. and Herrmann, F., 2006. Chemical potential – a quantity in search of recognition, *European Journal of Physics*, 27, 353-371.

Johnson, W.L. and Linke, W.A., 1978. Some practical applications to improve formation evaluation of sandstones in the mackenzie delta, SPWLA-1978-C, presented at SPWLA 19th Annual Logging Symposium, El Paso, TX, June 13-16.

Józefczak, A., Skumiel, A., and Łabowski, M., 2005. Effects of biocompatible coating of nanoparticles on acoustics property of the magnetic fluid, *Journal of Magnetism and Magnetic Materials*, 290–291, 265–268.

Kanj, M.Y., Funk, J.J, and Al-Yousif, Z., 2009. Nanofluid coreflood experiments in the ARAB-D, presented at SPE Saudi Arabia Section Technical Symposium and Exhibition, Alkhobar, Saudi Arabia, May 9-11. SPE 126161.

Kenyon, W. E., Day, P. I., Straley, C., and Willemsen, J. F., 1988. A three part study of NMR longitudinal relaxation properties of water saturated sandstones, *SPE Formation Evaluation*, 3(3), 622 -636.

Langford, J.I. and Wilson, A.J.C., 1978. Scherrer after sixty years: a survey and some new results in the determination of crystallite size, *Journal of Applied Crystallography*, 11, 102-113.

Lecoanet, H.F., Bottero, J.Y., and Wiesner, M.R., 2004. Laboratory assessment of the mobility of nanomaterials in porous media, *Environmental Science & Technology*, 38 (19), 5164-5169.

Martin, P. and Dacy, J., 2004. Effective Qv by NMR core tests, SPWLA-2004-HH, presented at SPWLA 45st Annual Logging Symposium, Noordwijk, The Netherlands, June 6-9.

Meiboom, S. and Gill, D., 1958. Modified spin-echo method for measuring nuclear relaxation times, *Review of Scientific Instruments*, 29, 688-691.

Mian, M.A. and Hilchie, D.W., 1981. Comparison of results from three cation exchange capacity analysis techniques, SPE-10550-MS.

Mooney, R.W., Keenan, A.G., and Wood, L.A., 1952. Adsorption of water vapor by montmorillonite, part i. heart of desorption and application of bet theory, *Journal of The American Chemical Society*, 74(6), 1367-1371.

Mooney, R.W., Keenan, A.G., and Wood, L.A., 1952. Adsorption of water vapor by montmorillonite, part ii. effect of exchangeable ions and lattice swelling as measured by X-Ray diffraction, *Journal of The American Chemical Society*, 74(6), 1371-1374.

Nadeau, P.H., 1985. The physical dimension of fundamental clay particles, *Clay Minerals*, 20, 499-514.

Neuman, C.H., 1983. Logging measurements of residual oil, Rangely Field, CO. SPE 8844, *Journal of Petroleum Technology*, 35 (9), 1735-1744.

Norrish, K., 1954. The swelling of montmorillonite, *Discussion of the Faraday Society*, 18, 120-134.

Odriozola, G. and Aguilar, J.F., 2005. Stability of Ca-montmorillonite hydrates: a computer simulation study, *Journal of Chemical Physics*, 123, 174708-1-174708-7.

Pinnavaia, T.J., 1983. Intercalated Clay Catelysts, *Science*, 220, 365-371.

Plank, J. and Bassioni, G., 2007. Adsorption of carboxylate anions on a CaCO3 surface, *Zeitschrift fur Naturforschung B*, 62 (10), 1277-1284.

Rodriguez, E., Roberts, M.R., Yu, H., Huh, C., and Bryant S.L., 2009. Enhanced migration of surface-treated nanoparticles in sedimentary rocks, presented at the SPE Annual Technical Conference and Exhibition, New Orleans, Louisiana, USA, October 4-7. SPE 124418.

Rosen, B.R., Belliveau, J.W., Vevea, J.M., and Brady, T.J., 1990. Perfusion imaging with NMR contrast agents, *Magnetic Resonance in Medicine*, 14 (2), 249–265.

Ross, G.J., 1968. Structural decomposition of an orthochlorite during its acid dissolution, *The Canadian Mineralogist*, 9(4), 522-530.

Rylander, E., Singer, P.M., Jiang, T., Lewis, R., and Mclin, R., 2013. NMR T2 distributions in the eagle ford shale: reflections on pore size, presented at the Unconventional Resources Conference, the Woodlands, Texas, USA, April 10-12. SPE 164554.

Salles, F., Beurroies, I., Bildstein, O., Jullien, M., Raynal, J., Denoyel, R., and Damme, H.V., 2008. A calorimetric study of mesoscopic swelling and hydration sequence in solid Na-montmorillonite, *Applied Clay Science*, 39, 186-201.

Salles, F., Devautour-Vinot, S., Bildstein, O., Jullien, M., Maurin, G., Giuntini, J.C., Douillard, J.M., and Damme, H.V., 2008. Ionic mobility and hydration energies in montmorillonite clay, *Journal of Physical Chemistry C*, 112(36), 14001-14009.

Scherrer, P., 1918. Bestimmung der grösse und der inneren struktur von kolloidteilchen mittels röntgenstrahlen, *Nachr. Ges. Wiss. Göttingen*, 26, 98-100.

Schulz, R.A., 2011. A case study in cased-hole log-inject-log techniques to determine residual oil saturation to asp injection, presented at the SPE Enhanced Oil Recovery Conference, Kuala Lumpur, Malaysia, July 19-21. SPE-144016-MS.

Seevers, D.O., 1966. A nuclear magnetic method for determining the permeability of sandstones, presented at the SPWLA 7th Annual Logging Symposium, Tulsa, Oklahoma, USA, May 9-11. SPWLA-1966-L.

Sen, P.N., Straley, C., Kenyon, W.E., and Whittingham, M.S., 1990. Surface-to-volume ratio, charge density, nuclear magnetic relaxation, and permeability in clay-bearing sandston, *Geophysics*, 55 (1), 61-69.

Shafer, J., 2013. Recent advances in core analysis, *Petrophysics*, 54(6), 554-579.

Sing, K.S. W., Everett, D.H., Haul, R.A. W., Moscou, L., Pierotti, R.A., Jouquerol, J., and Siemieniewska, T., 1985. Reporting physisorption data for gas/solid systems - with special reference to the determination of surface area and porosity, *Pure and Applied Chemistry*, 57(4), 603-619.

Sperinck, S., Paiteri, P., Marks, N., and Wright, K., 2010. Dehydroxylation of kaolinite to metakaolin - a molecular dynamics study, *Journal of Materials Chemistry*, 21, 2118-2125.

Stokes, R.H. and Robinson, R.A., 1949. Standard solutions for humidity control at 25˚C, *Industrial & Engineering Chemistry*, 41(9), 2013-2013.

Straley, C., Rossini, D., Vinegar, H., Tutunjian, P., and Morriss, C., 1997. Core analysis by low-field NMR. *The Log Analyst*, 38 (2), 84-94.

Tetens, O., 1930. Über einige meteorologische begriffe. Z, *Geophys*, 6, 207-309.

Thomas, E.C., 1976. The determination of Qv from membrane potential measurements on shaly sands, *Journal of Petroleum Technology*, 28(9), 1087-1096.

Toumelin, E., Sun, B., Manzoor, A., Keele, D., Wasson, M., and Sagnak, A., 2012. Revisiting log-inject-log NMR for remaining oil determination: a field application of T2 -d NMR in the Permian Basin. *Petrophysics*, 53 (3), 183-196.

Toussaint, B.F., Fripiat, J.J., and Gastuche, M.C., 1962. Dehydroxylation of kaolinite. I. kinetics, *Journal of Physical Chemistry*, 67(1), 26-30.

Unalmiser, S. and Funk, J.J., 1998. Engineering core analysis, *Journal of Petroleum Technology*, 50(4), 106-114.

Vandenbroucke, M. and Largeau, C., 2007. Kerogen origin, evolution and structure, *Organic Geochemistry*, 38(5), 719-833.

Wang, Y.X., Hussain, S.M., and Krestin, G.P., 2001. Superparamagnetic iron oxide contrast agents: physicochemical characteristics and applications in MR imaging. *European Radiology*, 11 (11), 2319–2331.

Waxman, M.H. and Smits, L.J.M., 1968. Electrical conductivities in oil-bearing shaly sands, *Society of Petroleum Engineers Journal*, 8(2), 107-122.

Weinmann, H.J., Brasch, R.C., Press, W.R., and Wesbey, G.E., 1984. Characteristic of gadolinium-DTPA complex: a potential NMR contrast agent, *AJR American Journal of Roentgenology*, 142 (3), 619–624.

Weissleder, R., Bogdanov, A., Neuwelt, E.A., and Papisov, M., 1995. Long-circulating iron oxides for MR imaging, *Advanced Drug Delivery Reviews*, 16 (2-3), 321–334.

Xu W., Johnston, C.T., Parker, P., and Agnew, S.F., 2000. Infrared study of water sorption on na-, li-, ca-, and mg-exchanged (swy-1 and saz-1) montmorillonite, *Clays and Clay Minerals*, 48(1), 120-131.

Yang, F., Li, Y., Chen, Z., Zhang, Y., Wu, J., and Gu, N., 2009. Superparamagnetic iron oxide nanoparticle-embedded encapsulated microbubbles as dual contrast agents of magnetic resonance and ultrasound imaging. *Biomaterials*, 30 (23-24), 3882–3890.

Young J.F., 1967. Humidity control in the laboratory using salt solutions—a review, *Journal of Applied Chemistry*, 17(9), 241-245.

Yu, H., 2012. Transport and retention of surface-modified nanoparticles in sedimentary rocks, Ph.D. Dissertation, The University of Texas at Austin, Austin,Texas, USA.

Yu, J., An, C., Mo, D., Liu, N., and Lee, R., 2012. Study of adsorption and transportation behavior of nanoparticles in three different porous media, presented at the Eighteenth SPE Improved Oil Recovery Symposium, Tulsa, Oklahoma, USA, April 14-18. SPE 153337.

Zhang, Z.Z. and Low, P.F., 1989. Relation between the heat of immersion and the initial water-content of li-montmorillonite, na-montmorillonite, and k-montmorillonite, *Journal of Colloidal Interface Science*, 133, 461–472.

APPENDIX

LIST OF PUBLICATIONS

Journal Publications

Cheng, K. and Heidari, Z., 2018, A new method for quantifying cation exchange capacity in clay minerals, *Applied Clay Science*, 161, 444-455.

Cheng, K. and Heidari, Z., 2017, Combined interpretation of NMR and TGA measurements to quantify the impact of relative humidity on hydration of clay minerals, *Applied Clay Science*, 143, 362-371.

Cheng, K. and Heidari, Z., 2017, Pore network connectivity and permeability assessment using NMR log-inject-log method, *SPE Reservoir Evaluation & Engineering*, 20(4), 831-838.

Chi, L., Cheng, K., and Heidari, Z., 2016, Improved assessment of interconnected porosity in multiple-porosity rocks by use of nanoparticle contrast agents and nuclear-magnetic-resonance relaxation measurements, *SPE Reservoir Evaluation & Engineering*, 19(1), 95-107.

Aderibigbe, A., Cheng, K., Heidari, Z., Killough, J., and Fuss, T., 2016, Application of magnetic nanoparticles mixed with propping agents in enhancing near-wellbore fracture detection, *Journal of Petroleum Science and Engineering*, 141, 133-143.

Cheng, K., Aderibigbe, A., Heidari, Z. and Killough, J., 2014, Quantifying the impact of petrophysical properties on spatial distribution of contrasting nanoparticle agents, *Petrophysics*, 55(5), 447-460.

Conference Proceedings

Cheng, K. and Heidari, Z, 2018, An experimental multi-physics method for quantifying cation exchange capacity of clay-rich rocks, SPWLA-2018-TT, SPWLA 59th Annual Symposium in London, UK, June 2–6.

Cheng, K. and Heidari, Z, 2018, A new method for quantifying cation exchange capacity: application to organic-rich mudrock formations, URTEC-2901029-MS, Unconventional Resources Technology Conference in Houston, Texas, USA, July 23–25.

Cheng, K. and Heidari, Z., 2017, A new theoretical method for quantifying cation exchange capacity, SPWLA-2017-YY, SPWLA 58th Annual Symposium in Oklahoma City, Oklahoma, USA, June 17–21.

Cheng, K. and Heidari, Z., 2016, An experimental approach to quantify the impact of relative humidity on hydration of clay minerals using NMR- and TGA-based evaluations, SPWLA-2016-O, SPWLA 57th Annual Symposium in Reykjavik, Iceland, June 25–19.

Cheng, K. and Heidari, Z., 2015, Pore connectivity and permeability assessment in carbonate formations using NMR log-inject-log method, SPE-175066-MS, SPE Annual Technical Conference and Exhibition Houston, Texas, USA, September 28–30.

Cheng, K., Aderibigbe, A., Heidari, Z. and Killough, J., 2014, Quantifying the impact of petrophysical properties on spatial distribution of contrasting nanoparticle agents, SPWLA-2014-YY, SPWLA 55th Annual Symposium in Abu Dhabi, May.

Cheng, K., Chi, L., and Heidari, Z., 2014, Improved assessment of pore-size distribution and pore connectivity in multiple-porosity systems using superparamagnetic iron oxide nanoparticles and NMR measurement, SPE 170792, SPE Annual Technical Conference and Exhibition, Amsterdam, The Netherlands, October 27-29.

Aderibigbe, A., Cheng, K., Heidari, Z., Killough, J., and Fuss, T., 2014, Detection of propping agents in fractures using magnetic susceptibility measurements enhanced by magnetic nanoparticles, SPE 170818, SPE Annual Technical Conference and Exhibition, Amsterdam, The Netherlands, October 27-29.